Digital defocus aberration interference for automated optical microscopy: Supplementary Notes

Haowen Zhou[1,†,*], Shi Zhao[1,†], Yujie Fan[2], Zhenyu Dong[1], Oumeng Zhang[1], Viviana Gradinaru[2], and Changhuei Yang[1]

[1]Department of Electrical Engineering, California Institute of Technology, Pasadena, CA, USA

[2]Division of Biology and Biological Engineering, California Institute of Technology, Pasadena, CA, USA

[*]hzhou7@caltech.edu

[†]These authors contribute equally to this work

Contents

List of frequently used abbreviations

Abbreviation	**Definition**
2D	Two-Dimensional
3D	Three-Dimensional
APIC	Angular Ptychographic Imaging with Closed-form method
DAbI	Digital defocus Aberration Interference
DoF	Depth of Field
FFT	Fast Fourier Transform
FOV	Field of View
FPM	Fourier Ptychographic Microscopy
LED	Light-Emitting Diode
NA	Numerical Aperture
PBR	Peak-to-Background Ratio
PSNR	Peak Signal-to-Noise Ratio
RMSE	Root Mean Square Error
SNR	Signal-to-Noise Ratio
SSIM	Structural Similarity Index Measure

1 Derivation of digital defocus aberration interference (DAbI) in 2D case

We begin our analysis with two-dimensional (2D) thin samples and subsequently generalize it to the three-dimensional (3D) case in Note 2.

1.1 Image formation forward model

In the DAbI system, the two illumination wavefronts from the LEDs can be modeled as tilted plane waves:

$$u(\mathbf{r}_\perp; \mathbf{k}_{i\perp}) = e^{j\mathbf{k}_{i\perp}\cdot\mathbf{r}_\perp}, \quad i = 1, 2 \tag{S1}$$

where $\mathbf{k}_{i\perp} = (k_{ix}, k_{iy})$, $i = 1, 2$ denote the transverse illumination wavevectors and $\mathbf{r}_\perp = (x, y)$ represents the transverse spatial coordinates.

These plane waves interact with the sample $o(\mathbf{r}_\perp)$, and the resulting field then propagates through a $4f$ imaging system. The camera captures the intensity of the complex-valued optical field at the image plane. This image formation process can be modeled as:

$$I_i = \left| \mathcal{F}^{-1} \left\{ \mathcal{F}\left\{ u(\mathbf{r}_\perp; \mathbf{k}_{i\perp})\, o(\mathbf{r}_\perp) \right\} \widehat{P}(\mathbf{k}_\perp) \right\} \right|^2, \quad i = 1, 2 \tag{S2}$$

where I_i is the intensity measurement from the i-th illumination angle, $\mathcal{F}\{\cdot\}$ denotes the 2D Fourier transform, and $\widehat{P}(\mathbf{k}_\perp)$ is the coherent transfer function of the system:

$$\widehat{P}(\mathbf{k}_\perp) = \mathbb{1}(|\mathbf{k}_\perp| \le k_0 \mathrm{NA})\, e^{j\widehat{\phi}(\mathbf{k}_\perp)},$$

where $k_0 = 2\pi/\lambda$ is the free-space wavenumber corresponding to the illumination wavelength λ, and $\widehat{\phi}(\mathbf{k}_\perp)$ denotes the system aberration, including defocus.

1.2 Digital interference-like fringes

Light interacting with the sample can be modeled as the sum of two components: the unscattered and scattered parts. According to the frequency-shifting property of the Fourier transform, we have:

$$\mathcal{F}\left\{ e^{j\mathbf{k}_{i\perp}\cdot\mathbf{r}_\perp}\, o(\mathbf{r}_\perp) \right\} = C \cdot \delta(\mathbf{k}_\perp - \mathbf{k}_{i\perp}) + \widehat{O}(\mathbf{k}_\perp - \mathbf{k}_{i\perp}), \tag{S3}$$

where $\delta(\mathbf{k}_\perp - \mathbf{k}_{i\perp})$ is the Dirac delta function representing the spectrum of the unscattered light, and $\widehat{O}(\mathbf{k}_\perp - \mathbf{k}_{i\perp})$ corresponds to the scattered component. For simplicity, we ignore the constant C in the following derivation.

Applying the Fourier transform to the intensity images I_i in Eq. (S2) and substituting Eq. (S3) yield

$$\mathcal{F}\{I_i\} = \mathcal{F}\left\{ \left| \mathcal{F}^{-1}\left\{ \left(\delta(\mathbf{k}_\perp - \mathbf{k}_{i\perp}) + \widehat{O}(\mathbf{k}_\perp - \mathbf{k}_{i\perp}) \right) \widehat{P}(\mathbf{k}_\perp) \right\} \right|^2 \right\}, \quad i = 1, 2. \tag{S4}$$

To simplify Eq. (S4), we first introduce

$$\xi_i(\mathbf{k}_\perp) = \left(\delta(\mathbf{k}_\perp - \mathbf{k}_{i\perp}) + \widehat{O}(\mathbf{k}_\perp - \mathbf{k}_{i\perp}) \right) \widehat{P}(\mathbf{k}_\perp), \tag{S5}$$

so that Eq. (S4) can be written compactly as

$$\mathcal{F}\{I_i\} = \mathcal{F}\Big\{ \left| \mathcal{F}^{-1}\{\xi_i(\mathbf{k}_\perp)\} \right|^2 \Big\}. \tag{S6}$$

Using the fact that the Fourier transform of an intensity is the autocorrelation of the corresponding field, $\mathcal{F}\{|u|^2\} = U \otimes U^*$ with $U = \mathcal{F}\{u\}$, we obtain

$$\mathcal{F}\{I_i\} = \xi_i(\mathbf{k}_\perp) \otimes \xi_i^*(-\mathbf{k}_\perp). \tag{S7}$$

We next separate the unscattered and scattered contributions by defining the auxiliary function

$$\widehat{\Psi}(\mathbf{k}_\perp) = \widehat{O}(\mathbf{k}_\perp - \mathbf{k}_{i\perp})\widehat{P}(\mathbf{k}_\perp), \tag{S8}$$

so that

$$\xi_i(\mathbf{k}_\perp) = \delta(\mathbf{k}_\perp - \mathbf{k}_{i\perp})\widehat{P}(\mathbf{k}_\perp) + \widehat{\Psi}(\mathbf{k}_\perp), \qquad \xi_i^*(\mathbf{k}_\perp) = \delta(\mathbf{k}_\perp - \mathbf{k}_{i\perp})\widehat{P}^*(\mathbf{k}_\perp) + \widehat{\Psi}^*(\mathbf{k}_\perp). \tag{S9}$$

Substituting these expressions into the convolution gives

$$\begin{aligned}
\mathcal{F}\{I_i\} &= \left[\delta(\mathbf{k}_\perp - \mathbf{k}_{i\perp})\widehat{P}(\mathbf{k}_\perp) + \widehat{\Psi}(\mathbf{k}_\perp)\right] \otimes \left[\delta(\mathbf{k}_\perp + \mathbf{k}_{i\perp})\widehat{P}^*(-\mathbf{k}_\perp) + \widehat{\Psi}^*(-\mathbf{k}_\perp)\right] \\
&= \delta(\mathbf{k}_\perp - \mathbf{k}_{i\perp})\widehat{P}(\mathbf{k}_\perp) \otimes \delta(\mathbf{k}_\perp + \mathbf{k}_{i\perp})\widehat{P}^*(-\mathbf{k}_\perp) \\
&\quad + \delta(\mathbf{k}_\perp - \mathbf{k}_{i\perp})\widehat{P}(\mathbf{k}_\perp) \otimes \widehat{\Psi}^*(-\mathbf{k}_\perp) + \widehat{\Psi}(\mathbf{k}_\perp) \otimes \delta(\mathbf{k}_\perp + \mathbf{k}_{i\perp})\widehat{P}^*(-\mathbf{k}_\perp) \\
&\quad + \widehat{\Psi}(\mathbf{k}_\perp) \otimes \widehat{\Psi}^*(-\mathbf{k}_\perp).
\end{aligned} \tag{S10}$$

Using the convolution and shift properties of the Dirac delta function in spatial frequency coordinates and absorbing constant factors into the overall normalization, the four terms above can be rewritten as

$$\begin{aligned}
\mathcal{F}\{I_i\}(\mathbf{k}_\perp) &= \delta(\mathbf{k}_\perp) + \widehat{\Psi}(\mathbf{k}_\perp) \otimes \delta(\mathbf{k}_\perp + \mathbf{k}_{i\perp}) + \widehat{\Psi}^*(-\mathbf{k}_\perp) \otimes \delta(\mathbf{k}_\perp - \mathbf{k}_{i\perp}) + \widehat{\Psi}(\mathbf{k}_\perp) \otimes \widehat{\Psi}^*(-\mathbf{k}_\perp) \\
&= \delta(\mathbf{k}_\perp) + \widehat{\Psi}(\mathbf{k}_\perp + \mathbf{k}_{i\perp}) + \widehat{\Psi}^*(\mathbf{k}_{i\perp} - \mathbf{k}_\perp) + \widehat{\Psi}(\mathbf{k}_\perp) \otimes \widehat{\Psi}^*(-\mathbf{k}_\perp), \qquad i = 1, 2.
\end{aligned} \tag{S11}$$

where $\widehat{\Psi}(\mathbf{k}_\perp) = \widehat{O}(\mathbf{k}_\perp - \mathbf{k}_{i\perp})\widehat{P}(\mathbf{k}_\perp)$ is an auxiliary function defined in spatial frequency coordinates (given by Eq. (S8)), and $\otimes$ denotes convolution.

As shown in Eq. (S11), the spectrum of each intensity image contains four distinct terms (Fig. (S1)). The first term arises from the unscattered light. The second and third terms represent the convolution of the scattered field with shifted delta functions and their complex conjugates, introducing positive and negative frequency shifts. The fourth term corresponds to the autocorrelation of the scattered spectrum.

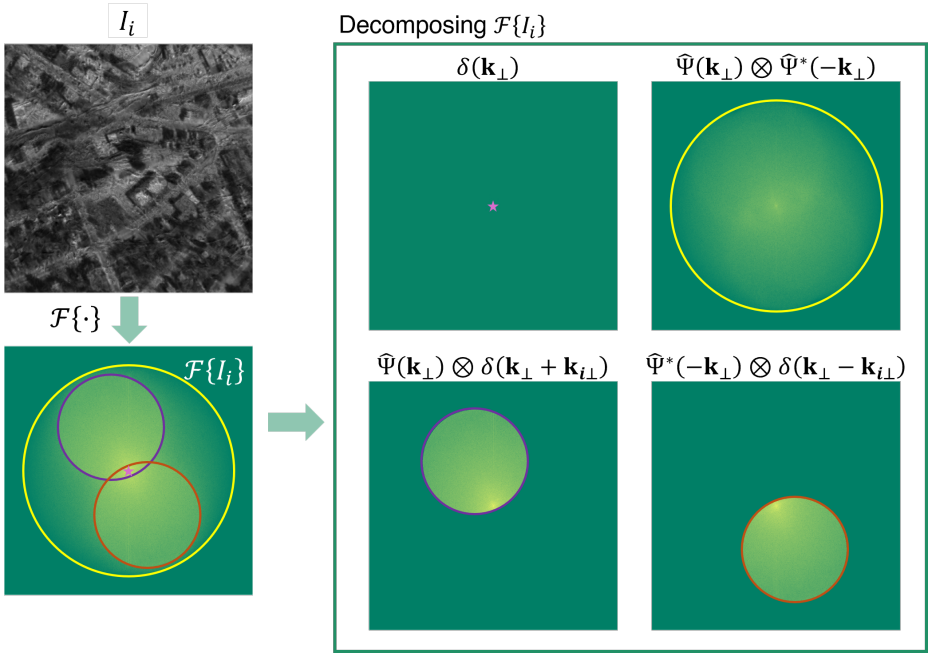

Figure S1: Fourier spectrum of an intensity image under an oblique illumination angle. I_i is an intensity measurement from the camera that can be modeled by Eq. (S2). The four components in the spectrum correspond to four terms in Eq. (S11)

DAbI captures two intensity images from two illumination angles. The spectra of these two images are summed to reveal the interference-like fringes in a numerical manner. Note that the first and fourth terms from the two spectra are located at the same spatial frequency region, while the second and third terms are

in different regions (Fig. (S1)). The sum of the first terms is still a Dirac delta function at the zero frequency. The sum of the fourth terms is a linear combination of the autocorrelation of the scattered spectra. If the sample is not highly absorptive or strongly scattering, the sum of the fourth terms is not dominant and serves as a minor background modulation for the fringes. Therefore, this sum can be neglected in later analysis. The effect of strong autocorrelation terms will be further discussed in Note 7. After neglecting the first and fourth terms, the resulting summed spectra can be approximated as:

$$\begin{aligned}\mathcal{F}\{I_1\}+\mathcal{F}\{I_2\} \approx & \widehat{O}(\mathbf{k}_\perp)\widehat{P}(\mathbf{k}_\perp+\mathbf{k}_{1\perp})+\widehat{O}(\mathbf{k}_\perp)\widehat{P}(\mathbf{k}_\perp+\mathbf{k}_{2\perp}) \\ & +\widehat{O}^*(-\mathbf{k}_\perp)\widehat{P}^*(-\mathbf{k}_\perp+\mathbf{k}_{1\perp})+\widehat{O}^*(-\mathbf{k}_\perp)\widehat{P}^*(-\mathbf{k}_\perp+\mathbf{k}_{2\perp}).\end{aligned} \tag{S12}$$

Given the finite circular support, $\widehat{P}(\pm\mathbf{k}_\perp+\mathbf{k}_{i\perp})$ is shifted by different illumination wavevectors; thus, the resulting scattered spectra occupy distinct spatial frequency regions. There exists a region that only contains

$$\widehat{O}(\mathbf{k}_\perp)\widehat{P}(\mathbf{k}_\perp+\mathbf{k}_{1\perp})+\widehat{O}(\mathbf{k}_\perp)\widehat{P}(\mathbf{k}_\perp+\mathbf{k}_{2\perp}),$$

indicated in the shaded region of Fig. (S2). This region can be mathematically defined as a set:

$$\mathcal{S} \coloneqq \left\{ \mathbf{k}_\perp \in \mathbb{R}^2 \;\middle|\; \begin{array}{l} |\mathbf{k}_\perp+\mathbf{k}_{1\perp}| \le k_0\mathrm{NA}, \\ |\mathbf{k}_\perp+\mathbf{k}_{2\perp}| \le k_0\mathrm{NA}, \\ |\mathbf{k}_\perp-\mathbf{k}_{1\perp}| > k_0\mathrm{NA}, \\ |\mathbf{k}_\perp-\mathbf{k}_{2\perp}| > k_0\mathrm{NA} \end{array} \right\}. \tag{S13}$$

Within this set $\mathcal{S}$, Eq. (S12) simplifies to:

$$\mathcal{F}\{I_1\}+\mathcal{F}\{I_2\} = \widehat{O}(\mathbf{k}_\perp)\widehat{P}(\mathbf{k}_\perp+\mathbf{k}_{1\perp})+\widehat{O}(\mathbf{k}_\perp)\widehat{P}(\mathbf{k}_\perp+\mathbf{k}_{2\perp}), \quad \mathbf{k}_\perp \in \mathcal{S}. \tag{S14}$$

The complex-valued sample spectrum $\widehat{O}(\mathbf{k}_\perp)$ can be written in terms of amplitude $\widehat{A}(\mathbf{k}_\perp)$ and phase $\widehat{\eta}(\mathbf{k}_\perp)$, and the coherent transfer function $\widehat{P}(\mathbf{k}_\perp)$ includes a phase term $\widehat{\phi}(\mathbf{k}_\perp)$ representing system aberrations. Thus:

$$\mathcal{F}\{I_1\}+\mathcal{F}\{I_2\} = \widehat{A}(\mathbf{k}_\perp)e^{j\widehat{\eta}(\mathbf{k}_\perp)}\left(e^{j\widehat{\phi}(\mathbf{k}_\perp+\mathbf{k}_{1\perp})}+e^{j\widehat{\phi}(\mathbf{k}_\perp+\mathbf{k}_{2\perp})}\right), \quad \mathbf{k}_\perp \in \mathcal{S}. \tag{S15}$$

From Eq. (S15), we see that the sample term $\widehat{A}(\mathbf{k}_\perp)e^{j\widehat{\eta}(\mathbf{k}_\perp)}$ is shared across both measurements, while the aberration terms $\widehat{\phi}(\mathbf{k}_\perp)$ are modulated by the illumination angle. Taking the magnitude of both sides gives:

$$\begin{aligned}|\mathcal{F}\{I_1\}+\mathcal{F}\{I_2\}| &= \left|\widehat{A}(\mathbf{k}_\perp)e^{j\widehat{\eta}(\mathbf{k}_\perp)}\right|\left|e^{j\widehat{\phi}(\mathbf{k}_\perp+\mathbf{k}_{1\perp})}+e^{j\widehat{\phi}(\mathbf{k}_\perp+\mathbf{k}_{2\perp})}\right| \\ &\propto \sqrt{2+2\cos\left(\widehat{\phi}(\mathbf{k}_\perp+\mathbf{k}_{1\perp})-\widehat{\phi}(\mathbf{k}_\perp+\mathbf{k}_{2\perp})\right)}, \quad \mathbf{k}_\perp \in \mathcal{S}.\end{aligned} \tag{S16}$$

Within the region $\mathcal{S}$, the resulting summed spectrum exhibits interference fringes due to the phase difference introduced by the aberrations at different illumination angles. The effect of $\left|\widehat{A}(\mathbf{k}_\perp)e^{j\widehat{\eta}(\mathbf{k}_\perp)}\right|$ in Eq. (S16) will be discussed in Note 8.1.

1.3 The choice of set $\mathcal{S}$

In Eq. (S13), we have defined a set $\mathcal{S}$, as indicated graphically in Fig. S2. This set $\mathcal{S}$ encompasses one of the two regions where fringes may appear. However, there are other overlap regions between two of the circles in Fig. S2. For example, there exists an overlap region between the pink and red circles that is perpendicular to the set $\mathcal{S}$. We define this overlap region as $\mathcal{S}^*$:

$$\mathcal{S}^* \coloneqq \left\{ \mathbf{k}_\perp \in \mathbb{R}^2 \;\middle|\; \begin{array}{l} |\mathbf{k}_\perp+\mathbf{k}_{1\perp}| \le k_0\mathrm{NA}, \\ |\mathbf{k}_\perp+\mathbf{k}_{2\perp}| > k_0\mathrm{NA}, \\ |\mathbf{k}_\perp-\mathbf{k}_{1\perp}| > k_0\mathrm{NA}, \\ |\mathbf{k}_\perp-\mathbf{k}_{2\perp}| \le k_0\mathrm{NA} \end{array} \right\}. \tag{S17}$$

Here, we would like to justify our choice between the set $\mathcal{S}$ and $\mathcal{S}^*$.

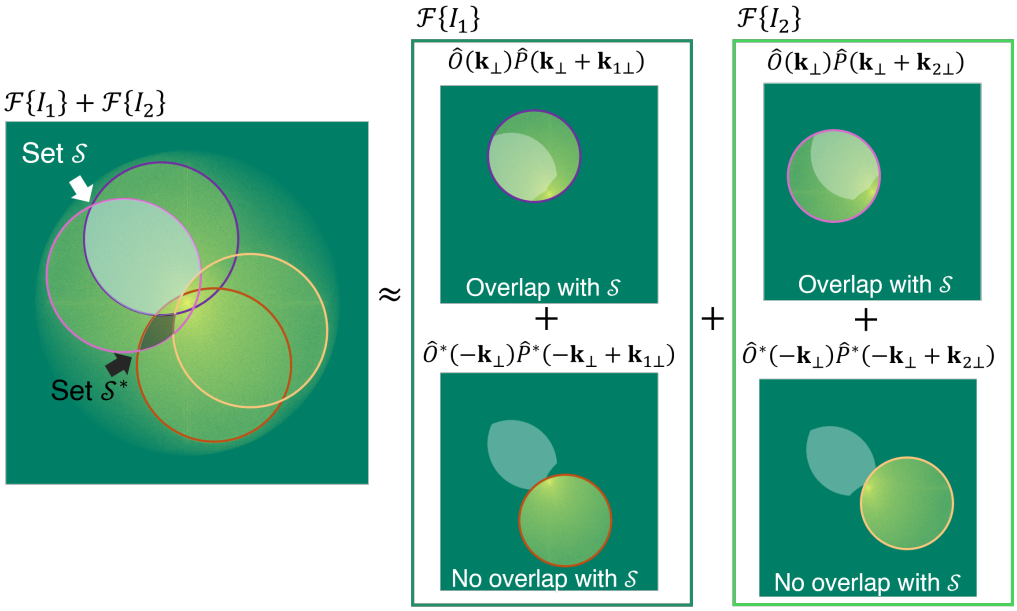

Figure S2: Fourier spectrum of two intensity images under two oblique illumination angles. The white-shaded region indicates set $\mathcal{S}$ in Eq. (S13), and the black-shaded region shows set $\mathcal{S}^*$ in Eq. (S17).

For a straightforward comparison, we list the mathematical modeling of the signals within these two sets in the following expressions:

$$\begin{aligned}
\mathbf{k}_\perp \in \mathcal{S} : & \left|\widehat{A}(\mathbf{k}_\perp)e^{j\widehat{\eta}(\mathbf{k}_\perp)}\right| \left|e^{j\widehat{\phi}(\mathbf{k}_\perp+\mathbf{k}_{1\perp})} + e^{j\widehat{\phi}(\mathbf{k}_\perp+\mathbf{k}_{2\perp})}\right|, \\
& \equiv \left|\widehat{A}(\mathbf{k}_\perp)\right| \, 2\left|\cos\left(\frac{\widehat{\phi}(\mathbf{k}_\perp+\mathbf{k}_{1\perp}) - \widehat{\phi}(\mathbf{k}_\perp+\mathbf{k}_{2\perp})}{2}\right)\right| \\
\mathbf{k}_\perp \in \mathcal{S}^* : & \left|\widehat{A}(\mathbf{k}_\perp)\right| \left|e^{j[\widehat{\phi}(\mathbf{k}_\perp+\mathbf{k}_{1\perp})+\widehat{\eta}(\mathbf{k}_\perp)]} + e^{-j[\widehat{\phi}(-\mathbf{k}_\perp+\mathbf{k}_{2\perp})+\widehat{\eta}(\mathbf{k}_\perp)]}\right| \\
& \equiv \left|\widehat{A}(\mathbf{k}_\perp)\right| \, 2\left|\cos\left(\frac{\widehat{\phi}(\mathbf{k}_\perp+\mathbf{k}_{1\perp}) + \widehat{\phi}(-\mathbf{k}_\perp+\mathbf{k}_{2\perp})}{2} + \widehat{\eta}(\mathbf{k}_\perp)\right)\right|.
\end{aligned} \tag{S18}$$

From the above two expressions, we observe that the cosine modulation in set $\mathcal{S}$ is only determined by the defocus aberration $\widehat{\phi}$. However, in the set $\mathcal{S}^*$, the cosine term is "contaminated" by the sample spectrum phase $\widehat{\eta}(\mathbf{k}_\perp)$. Additionally, the sum of $\widehat{\phi}(\mathbf{k}_\perp + \mathbf{k}_{1\perp})$ and $\widehat{\phi}(\mathbf{k}_\perp + \mathbf{k}_{2\perp})$ instead of subtraction leads to complicated patterns, which can be hard in the detection process. Therefore, the set $\mathcal{S}$ is chosen for defocus detection in DAbI.

1.4 Relation between defocus aberration and interference-like fringes

$\widehat{\phi}(\mathbf{k}_\perp)$ represents the system aberration. In the application of autofocusing and digital refocusing, $\widehat{\phi}(\mathbf{k}_\perp)$ is mostly defocus aberration; thus, it can be expressed as:

$$\widehat{\phi}(\mathbf{k}_\perp) = \sqrt{k_0^2 - |\mathbf{k}_\perp|^2}\,\Delta z \tag{S19}$$

where Δz denotes the defocus distance. Substituting Eq. (S19) into the cosine term in Eq. (S16) gives:

$$\cos\left(\widehat{\phi}(\mathbf{k}_\perp + \mathbf{k}_{1\perp}) - \widehat{\phi}(\mathbf{k}_\perp + \mathbf{k}_{2\perp})\right) = \cos\left(\sqrt{k_0^2 - |\mathbf{k}_\perp + \mathbf{k}_{1\perp}|^2}\,\Delta z - \sqrt{k_0^2 - |\mathbf{k}_\perp + \mathbf{k}_{2\perp}|^2}\,\Delta z\right). \tag{S20}$$

When $\cos(\cdot) = -1$, the function exhibits valleys (local minima), satisfying:

$$\sqrt{k_0^2 - |\mathbf{k}_{v\perp} + \mathbf{k}_{1\perp}|^2}\,\Delta z - \sqrt{k_0^2 - |\mathbf{k}_{v\perp} + \mathbf{k}_{2\perp}|^2}\,\Delta z = n\pi, \quad n = 2m - 1,\ m \in \mathbb{Z},\ \mathbf{k}_{v\perp} \in \mathcal{S}. \tag{S21}$$

The solutions to Eq. (S21) specify the n-th order fringe valley positions $\mathbf{k}_{v\perp}$. By tracking these valley positions, we can solve for the defocus Δz (Eq. (3) in the main paper):

$$|\Delta z| = \left| \frac{n\pi}{\sqrt{k_0^2 - |\mathbf{k}_{v\perp} + \mathbf{k}_{1\perp}|^2} - \sqrt{k_0^2 - |\mathbf{k}_{v\perp} + \mathbf{k}_{2\perp}|^2}} \right|. \tag{S22}$$

The validity of Eq. (S22) relies on defocus being the dominant aberration. When other aberrations are minor, the solution in Eq. (S22) remains valid. In the case where other aberrations—such as spherical or astigmatic aberrations—are significant, a one-time system aberration precalibration is required (Note 6.4).

1.5 Linearity and nonlinearity in DAbI fringes

Equation (S21) reveals the positions of the DAbI fringe valleys under defocus aberration. In this section, we show that DAbI exhibits straight, parallel, and evenly spaced fringes in low-NA systems (e.g., NA ≤ 0.30), while curved fringes emerge in high-NA systems.

Without loss of generality, we define the transverse illumination wavevectors as

$$\mathbf{k}_{1\perp} = \big(k_0 \sin\beta_1 \cos\theta_1,\ k_0 \sin\beta_1 \sin\theta_1\big), \quad \mathbf{k}_{2\perp} = \big(k_0 \sin\beta_2 \cos\theta_2,\ k_0 \sin\beta_2 \sin\theta_2\big), \tag{S23}$$

where β_1 and β_2 denote the polar illumination angles of the two LEDs, and θ_1 and θ_2 denote their azimuthal illumination angles (formally defined in Note. 3). For convenience, we graphically show the definition of these angles in Fig. S3.

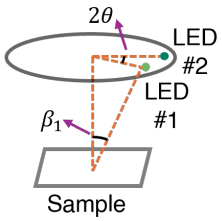

Figure S3: Graphical definition of polar illumination angle β and azimuthal illumination angle θ.

The right-hand side of Eq. (S21) can be expanded using a Taylor series:

$$\begin{aligned}
&\left(\sqrt{k_0^2 - |\mathbf{k}_{v\perp} + \mathbf{k}_{1\perp}|^2} - \sqrt{k_0^2 - |\mathbf{k}_{v\perp} + \mathbf{k}_{2\perp}|^2}\right)\Delta z \\
&= \left(\frac{|\mathbf{k}_{v\perp} + \mathbf{k}_{2\perp}|^2}{2k_0} - \frac{|\mathbf{k}_{v\perp} + \mathbf{k}_{1\perp}|^2}{2k_0}\right)\Delta z \\
&\quad + \left(\frac{|\mathbf{k}_{v\perp} + \mathbf{k}_{2\perp}|^4}{8k_0^3} - \frac{|\mathbf{k}_{v\perp} + \mathbf{k}_{1\perp}|^4}{8k_0^3}\right)\Delta z \\
&\quad + \mathcal{O}\left(\frac{|\mathbf{k}_{v\perp} + \mathbf{k}_{1\perp}|^6}{k_0^5}\right)\Delta z + \mathcal{O}\left(\frac{|\mathbf{k}_{v\perp} + \mathbf{k}_{2\perp}|^6}{k_0^5}\right)\Delta z.
\end{aligned} \tag{S24}$$

The fringe valley wavevector $\mathbf{k}_{v\perp}$ is constrained within DAbI's working region $\mathcal{S}$ (defined in Eq. (S13) and Fig. S2), such that

$$|\mathbf{k}_{v\perp} + \mathbf{k}_{1\perp}| \leq k_0\mathrm{NA}, \quad |\mathbf{k}_{v\perp} + \mathbf{k}_{2\perp}| \leq k_0\mathrm{NA}. \tag{S25}$$

For low-NA systems, NA is small,

$$\frac{|\mathbf{k}_{v\perp} + \mathbf{k}_{i\perp}|^4/(8k_0^3)}{|\mathbf{k}_{v\perp} + \mathbf{k}_{i\perp}|^2/(2k_0)} = \frac{|\mathbf{k}_{v\perp} + \mathbf{k}_{i\perp}|^2}{4k_0^2} < \frac{1}{4}\mathrm{NA}^2 \ll 1, \tag{S26}$$

and thus the fourth-order and higher-order terms in Eq. (S24) can be neglected. Equation (S24) can therefore be approximated as

$$\left(\sqrt{k_0^2-|\mathbf{k}_{v\perp}+\mathbf{k}_{1\perp}|^2}-\sqrt{k_0^2-|\mathbf{k}_{v\perp}+\mathbf{k}_{2\perp}|^2}\right)\Delta z\approx\left(\frac{|\mathbf{k}_{v\perp}+\mathbf{k}_{2\perp}|^2}{2k_0}-\frac{|\mathbf{k}_{v\perp}+\mathbf{k}_{1\perp}|^2}{2k_0}\right)\Delta z. \tag{S27}$$

Substituting Eq. (S23) and letting $\mathbf{k}_{v\perp}=(k_{vx},k_{vy})$, Eq. (S27) can be simplified to

$$\begin{aligned}&\left(\sqrt{k_0^2-|\mathbf{k}_{v\perp}+\mathbf{k}_{1\perp}|^2}-\sqrt{k_0^2-|\mathbf{k}_{v\perp}+\mathbf{k}_{2\perp}|^2}\right)\Delta z\\&\approx\frac{k_0}{2}\left(\sin^2\beta_2-\sin^2\beta_1\right)\Delta z+\left(\sin\beta_2\cos\theta_2-\sin\beta_1\cos\theta_1\right)k_{vx}\Delta z\\&\quad+\left(\sin\beta_2\sin\theta_2-\sin\beta_1\sin\theta_1\right)k_{vy}\Delta z\\&=n\pi,\quad n=2m-1,\ m\in\mathbb{Z},\ \mathbf{k}_{v\perp}\in\mathcal{S}.\end{aligned} \tag{S28}$$

Equation (S28) represents a family of straight lines in the (k_{vx},k_{vy}) plane, corresponding to straight, parallel, and evenly spaced fringes, as shown in the left panel of Fig. S4. The spacing between adjacent fringes is given by

$$d=\frac{2\pi}{\Delta z\sqrt{\left(\sin\beta_2\cos\theta_2-\sin\beta_1\cos\theta_1\right)^2+\left(\sin\beta_2\sin\theta_2-\sin\beta_1\sin\theta_1\right)^2}}. \tag{S29}$$

For high-NA systems, NA^2 is no longer negligible compared with unity, and the higher-order terms in Eq. (S24) must be retained. The resulting quadratic and higher-order terms (e.g., k_{vx}^2, k_{vy}^2, and $k_{vx}k_{vy}$) introduce curvature into the fringes, as illustrated in the right panel of Fig. S4. A detailed description of how to recover the correct defocus distance from curved fringes is provided in Note 4.

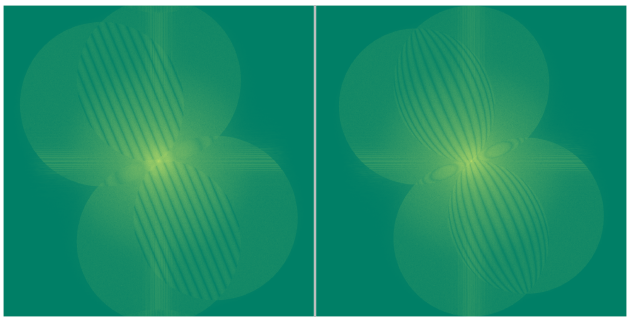

Figure S4: Simulated DAbI fringes with 10x 0.25NA (left) and 40x 0.95NA (right), and a camera pixel pitch of 6.5 µm

1.6 Virtual defocus aberration strategy

From Eq. (S22), we note that the sign of defocus is missing. Also, when the defocus is small, the term

$$\left|\sqrt{k_0^2-|\mathbf{k}_{v\perp}+\mathbf{k}_{1\perp}|^2}-\sqrt{k_0^2-|\mathbf{k}_{v\perp}+\mathbf{k}_{2\perp}|^2}\right|\in[0,\pi)$$

may result in the absence of observable fringe valleys.

To handle such situations, we design and employ a virtual defocus aberration strategy, as shown in Fig. S5. In this strategy, within the set $\mathcal{S}$, instead of directly summing the contributions from the two measurements as in Eq. (S14) and Eq. (S15), we first manually add a known, adaptive defocus aberration to each measurement separately. This yields:

$$\mathcal{F}\{I_i\}_{\mathrm{Vir}}=\widehat{A}(\mathbf{k}_\perp)e^{j\widehat{\eta}(\mathbf{k}_\perp)}e^{j\sqrt{k_0^2-|\mathbf{k}_\perp+\mathbf{k}_{i\perp}|^2}\,\Delta z}e^{j\sqrt{k_0^2-|\mathbf{k}_\perp+\mathbf{k}_{i\perp}|^2}\,z_v},\quad i=1,2,\quad \mathbf{k}_\perp\in\mathcal{S}, \tag{S30}$$

where $\mathcal{F}\{I_i\}_{\text{Vir}}$ is the virtual intensity spectrum with additional defocus aberration, and z_v is the added defocus distance.

We then sum the two virtual terms and take the magnitude:

$$|\mathcal{F}\{I_1\}_{\text{Vir}} + \mathcal{F}\{I_2\}_{\text{Vir}}| = \left|\widehat{A}(\mathbf{k}_\perp)e^{j\widehat{\eta}(\mathbf{k}_\perp)}\right| \left|e^{j\sqrt{k_0^2-|\mathbf{k}_\perp+\mathbf{k}_{1\perp}|^2}(\Delta z+z_v)} + e^{j\sqrt{k_0^2-|\mathbf{k}_\perp+\mathbf{k}_{2\perp}|^2}(\Delta z+z_v)}\right|. \tag{S31}$$

For the small defocus aberration case, by adding a relatively large z_v, we virtually increase the total defocus distance, and the valleys of the interference fringes become visible. We can then locate the valley positions and solve for $\Delta z + z_v$:

$$\Delta z + z_v = \frac{\text{sgn}(z_v)\,|n\pi|}{\left|\sqrt{k_0^2 - |\mathbf{k}_{\text{vir}\perp} + \mathbf{k}_{1\perp}|^2} - \sqrt{k_0^2 - |\mathbf{k}_{\text{vir}\perp} + \mathbf{k}_{2\perp}|^2}\right|}. \tag{S32}$$

In this case, since $|z_v| > |\Delta z|$, the sign of $\Delta z + z_v$ is determined by the sign function $\text{sgn}(z_v)$, and Δz can be calculated simply by subtracting z_v.

In other cases, the sign of Δz can also be determined using a small defocus offset z_v, $0 < |z_v| < |\Delta z|$,

$$|\Delta z \pm z_v| = \frac{|n\pi|}{\left|\sqrt{k_0^2 - |\mathbf{k}^{\pm}_{\text{vir}\perp} + \mathbf{k}_{1\perp}|^2} - \sqrt{k_0^2 - |\mathbf{k}^{\pm}_{\text{vir}\perp} + \mathbf{k}_{2\perp}|^2}\right|}. \tag{S33}$$

From Eq. (S33), we obtain $|\Delta z \pm z_v|$. Then the sign of Δz can be determined by:

$$\text{sgn}(\Delta z) = \text{sgn}\left(|\Delta z + z_v| - |\Delta z - z_v|\right) \cdot \text{sgn}(z_v). \tag{S34}$$

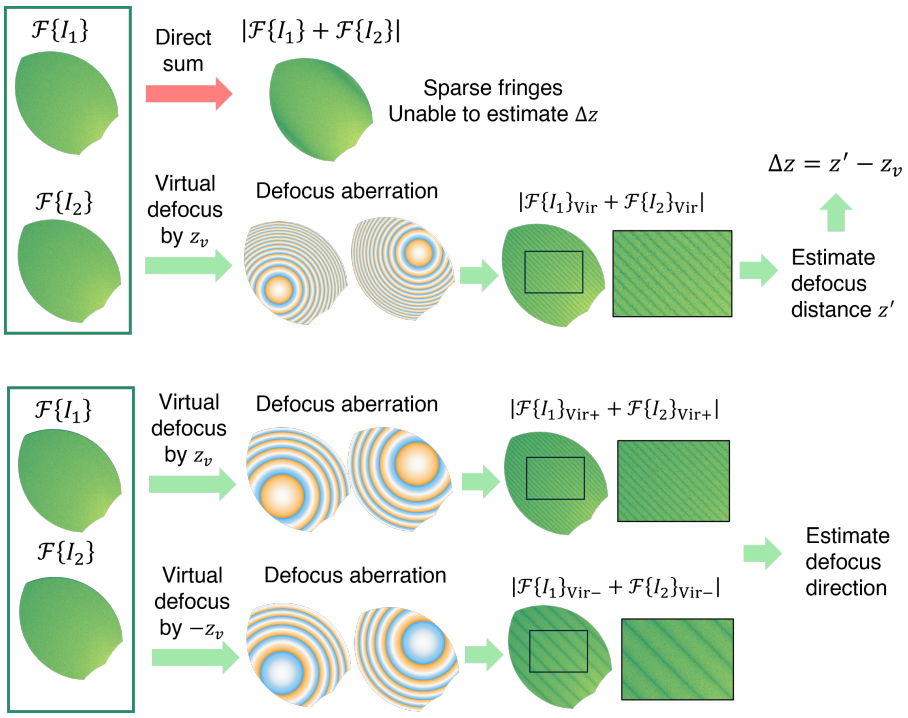

Figure S5: Virtual defocus aberration strategy in finding small defocus distance (top panel) and determining defocus direction (bottom panel).

1.7 Theory extension to temporally partially coherent light

The above analyses were based on the coherent light model. In practice, DAbI can also be achieved by partially coherent light sources. In this section and the next, we will discuss the theoretical modeling of DAbI under partially coherent light. To facilitate understanding of the derivations below and in Note 1.8, we present Fig. S6 to align the physics picture and mathematical notations.

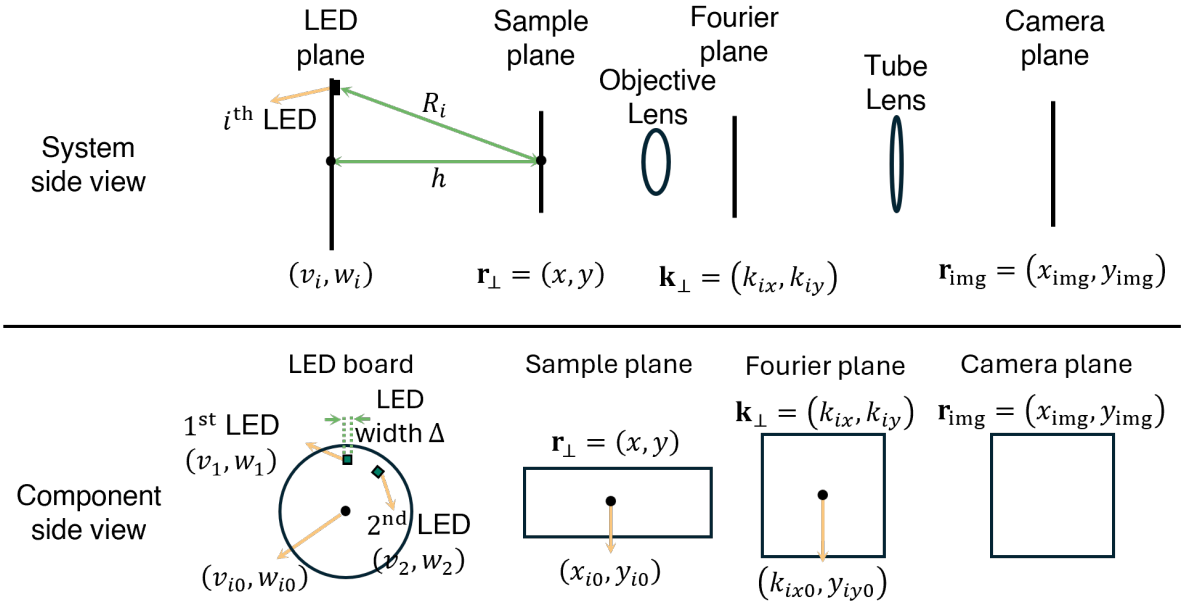

Figure S6: Notations for partially coherent light theory. Top panel: system side view and notations for coordinates and some definitions; Bottom panel: components side view and related notations.

First, assuming that only *temporal* partial coherence is present, each LED is treated as an ideal point source in space. Spectrally, the LED is modeled as a narrowband Gaussian source, which limits its temporal coherence and may consequently influence the measured DAbI fringes. In this section, we analyze the effect of temporal coherence on the DAbI phenomenon.

Without loss of generality, we assume the LED spectral power density follows a Gaussian distribution. The corresponding normalized spectral density is

$$T(\lambda) = \frac{1}{\sqrt{2\pi}\,\sigma_\lambda} \exp\left[-\frac{(\lambda - \lambda_0)^2}{2\sigma_\lambda^2}\right], \tag{S35}$$

where λ_0 is the central wavelength and σ_λ is the standard deviation (spectral bandwidth parameter).

For a fixed wavelength λ_m, the monochromatic model derived in Note 1.2 still holds. Therefore, within the overlap region $\mathcal{S}(\lambda_m)$,

$$\mathcal{S}(\lambda_m) = \left\{ \mathbf{k}_\perp \in \mathbb{R}^2 \;\middle|\; \begin{array}{l} |\mathbf{k}_\perp + \mathbf{k}_{1\perp}(\lambda_m)| \le \dfrac{2\pi}{\lambda_m}\,\mathrm{NA}, \\ |\mathbf{k}_\perp + \mathbf{k}_{2\perp}(\lambda_m)| \le \dfrac{2\pi}{\lambda_m}\,\mathrm{NA}, \\ |\mathbf{k}_\perp - \mathbf{k}_{1\perp}(\lambda_m)| > \dfrac{2\pi}{\lambda_m}\,\mathrm{NA}, \\ |\mathbf{k}_\perp - \mathbf{k}_{2\perp}(\lambda_m)| > \dfrac{2\pi}{\lambda_m}\,\mathrm{NA}, \end{array} \right\}, \tag{S36}$$

the summation of the intensity spectra is analogous to Eq. (S14):

$$\begin{aligned} \mathcal{F}\{I_1(\lambda_m)\} + \mathcal{F}\{I_2(\lambda_m)\} \approx\; & \widehat{O}(\mathbf{k}_\perp; \lambda_m)\, \widehat{P}(\mathbf{k}_\perp + \mathbf{k}_{1\perp}(\lambda_m); \lambda_m)\, \widehat{P}^*(\mathbf{k}_{1\perp}(\lambda_m); \lambda_m) \\ & + \widehat{O}(\mathbf{k}_\perp; \lambda_m)\, \widehat{P}(\mathbf{k}_\perp + \mathbf{k}_{2\perp}(\lambda_m); \lambda_m)\, \widehat{P}^*(\mathbf{k}_{2\perp}(\lambda_m); \lambda_m), \end{aligned} \tag{S37}$$

where $\mathbf{k}_{i\perp} = (k_{ix}, k_{iy}) = \left(-k_0 \frac{v_i}{R_i}, -k_0 \frac{w_i}{R_i}\right)$ are the transverse wavevector components, (v_i, w_i) is the i-th LED position in the LED plane, h is the distance from the LED plane to the sample plane, and $R_i = \sqrt{v_i^2 + w_i^2 + h^2}$. Here $k_0 = 2\pi/\lambda_m$. Unlike the derivation from Eq. (S11) to Eq. (S14), we do *not* absorb the constant phase factors $\widehat{P}^*(\mathbf{k}_{1\perp}(\lambda_m); \lambda_m)$ and $\widehat{P}^*(\mathbf{k}_{2\perp}(\lambda_m); \lambda_m)$ into the overall normalization, because these factors also depend on λ_m and vary across wavelength.

In practical settings, the exposure time is typically much longer than the coherence time of LED sources. Hence, the time-averaged mutual-coherence terms between different wavelengths vanish. The detected intensity is an incoherent superposition of the source spectrum:

$$\tilde{I}_i = \int T(\lambda)\, I_i(\lambda)\, \mathrm{d}\lambda. \tag{S38}$$

Accordingly, Eq. (S37) can be written as

$$\begin{aligned} \mathcal{F}\{\tilde{I}_1\} + \mathcal{F}\{\tilde{I}_2\} \approx & \int T(\lambda)\, \widehat{O}(\mathbf{k}_\perp; \lambda)\, \widehat{P}(\mathbf{k}_\perp + \mathbf{k}_{1\perp}(\lambda); \lambda)\, \widehat{P}^*(\mathbf{k}_{1\perp}(\lambda); \lambda)\, \mathrm{d}\lambda \\ & + \int T(\lambda)\, \widehat{O}(\mathbf{k}_\perp; \lambda)\, \widehat{P}(\mathbf{k}_\perp + \mathbf{k}_{2\perp}(\lambda); \lambda)\, \widehat{P}^*(\mathbf{k}_{2\perp}(\lambda); \lambda)\, \mathrm{d}\lambda, \end{aligned} \tag{S39}$$

whose validity region is

$$\tilde{\mathcal{S}} = \bigcap_{\lambda \in \Lambda} \mathcal{S}(\lambda) = \left\{ \mathbf{k}_\perp \in \mathbb{R}^2 \;\middle|\; \begin{array}{l} \|\mathbf{k}_\perp + \mathbf{k}_{1\perp}(\lambda)\| \le \dfrac{2\pi}{\lambda}\,\mathrm{NA}, \\ \|\mathbf{k}_\perp + \mathbf{k}_{2\perp}(\lambda)\| \le \dfrac{2\pi}{\lambda}\,\mathrm{NA}, \\ \|\mathbf{k}_\perp - \mathbf{k}_{1\perp}(\lambda)\| > \dfrac{2\pi}{\lambda}\,\mathrm{NA}, \\ \|\mathbf{k}_\perp - \mathbf{k}_{2\perp}(\lambda)\| > \dfrac{2\pi}{\lambda}\,\mathrm{NA} \end{array} \forall\, \lambda \in \Lambda \right\}. \tag{S40}$$

where $\Lambda = [\lambda_0 - 3\sigma_\lambda,\ \lambda_0 + 3\sigma_\lambda]$ is the main-energy interval of the Gaussian spectrum. Because the LED bandwidth is narrow ($\sigma_\lambda \ll \lambda_0$), $\tilde{\mathcal{S}}$ does not shrink significantly compared with $\mathcal{S}(\lambda)$, so the fringes remain visible over a wide region.

Similarly, since σ_λ is small, the sample scattering spectrum can be treated as slowly varying over Λ:

$$\widehat{O}(\mathbf{k}_\perp; \lambda) \approx \widehat{O}(\mathbf{k}_\perp; \lambda_0) \equiv \widehat{O}(\mathbf{k}_\perp), \qquad \lambda \in \Lambda. \tag{S41}$$

Then Eq. (S39) can be rearranged into

$$\mathcal{F}\{\tilde{I}_1\} + \mathcal{F}\{\tilde{I}_2\} \approx \widehat{O}(\mathbf{k}_\perp) \left[\int T(\lambda)\, \mathrm{e}^{j\Psi(\lambda, \mathbf{k}_\perp, \mathbf{k}_{1\perp})}\, \mathrm{d}\lambda + \int T(\lambda)\, \mathrm{e}^{j\Psi(\lambda, \mathbf{k}_\perp, \mathbf{k}_{2\perp})}\, \mathrm{d}\lambda \right], \tag{S42}$$

where the phase term is

$$\begin{aligned} \Psi(\lambda, \mathbf{k}_\perp, \mathbf{k}_{i\perp}) &= \widehat{\phi}(\lambda, \mathbf{k}_\perp + \mathbf{k}_{i\perp}) - \widehat{\phi}(\lambda, \mathbf{k}_{i\perp}) \\ &= \left(\sqrt{\left(\frac{2\pi}{\lambda}\right)^2 - \|\mathbf{k}_\perp + \mathbf{k}_{i\perp}\|^2} - \sqrt{\left(\frac{2\pi}{\lambda}\right)^2 - \|\mathbf{k}_{i\perp}\|^2} \right) \Delta z. \end{aligned} \tag{S43}$$

Next, we handle each integral term in Eq. (S42). Note that $\Psi(\lambda, \mathbf{k}_\perp, \mathbf{k}_{i\perp})$ is a function of both $\mathbf{k}_\perp$ and λ:

$$\Psi(\lambda; v_i, w_i, \mathbf{k}_\perp) = \left(\sqrt{\left(\frac{2\pi}{\lambda}\right)^2 - \left(k_x - \frac{2\pi v_i}{\lambda R_i}\right)^2 - \left(k_y - \frac{2\pi w_i}{\lambda R_i}\right)^2} - \frac{2\pi h}{\lambda R_i} \right) \Delta z. \tag{S44}$$

Because the LED is narrowband, we perform a Taylor expansion of Ψ around λ_0:

$$\Psi(\lambda; v_i, w_i, \mathbf{k}_\perp) = q_{0,i} + q_{1,i}\, \delta\lambda + \frac{1}{2} q_{2,i}\, (\delta\lambda)^2 + \cdots, \qquad \delta\lambda = \lambda - \lambda_0, \tag{S45}$$

where

$$q_{0,i} = \Psi(\lambda_0; v_i, w_i, \mathbf{k}_\perp), \qquad q_{1,i} = \left.\frac{\partial \Psi}{\partial \lambda}\right|_{\lambda_0}, \qquad q_{2,i} = \left.\frac{\partial^2 \Psi}{\partial \lambda^2}\right|_{\lambda_0}. \tag{S46}$$

For typical narrowband LED experiments (e.g., $\lambda_0 = 5.2 \times 10^{-7}$ m and $\sigma_\lambda \approx 2 \times 10^{-8}$ m) with representative geometric scales ($h \sim 10^{-1}$ m, $\Delta z \sim 10^{-4}$ m, $v_i, w_i \sim 3 \times 10^{-2}$ m for NA-matching illumination of a NA = 0.4 objective, and $\mathbf{k}_\perp$ near DC), numerical evaluation indicates that the second-order contribution satisfies $\frac{1}{2} q_{2,i} (3\delta\lambda)^2 \sim 10^{-3} \ll 1$, so terms of order ≥ 2 can be safely neglected. Therefore, the integral term in Eq. (S42) can be approximated by retaining only the linear term:

$$\int \frac{1}{\sqrt{2\pi}\,\sigma_\lambda} \exp\left[-\frac{(\lambda - \lambda_0)^2}{2\sigma_\lambda^2}\right] \mathrm{e}^{j\Psi(\lambda, \mathbf{k}_\perp, \mathbf{k}_{i\perp})}\, \mathrm{d}\lambda \approx \mathrm{e}^{j q_{0,i}} \frac{1}{\sqrt{2\pi}\,\sigma_\lambda} \int \exp\left[-\frac{(\delta\lambda)^2}{2\sigma_\lambda^2}\right] \mathrm{e}^{j q_{1,i} \delta\lambda}\, \mathrm{d}(\delta\lambda). \tag{S47}$$

This Gaussian integral yields

$$\int T(\lambda)\, \mathrm{e}^{j\Psi(\lambda, \mathbf{k}_\perp, \mathbf{k}_{i\perp})}\, \mathrm{d}\lambda \approx \mathrm{e}^{j q_{0,i}} \exp\left(-\frac{1}{2}\sigma_\lambda^2 q_{1,i}^2\right). \tag{S48}$$

Consequently,

$$\left|\mathcal{F}\{\tilde{I}_1\} + \mathcal{F}\{\tilde{I}_2\}\right| \approx \left|\widehat{O}(\mathbf{k}_\perp)\right| \left|\mathrm{e}^{j q_{0,1}} \exp\left(-\frac{1}{2}\sigma_\lambda^2 q_{1,1}^2\right) + \mathrm{e}^{j q_{0,2}} \exp\left(-\frac{1}{2}\sigma_\lambda^2 q_{1,2}^2\right)\right|. \tag{S49}$$

Define

$$A_1 = \exp\left(-\frac{1}{2}\sigma_\lambda^2 q_{1,1}^2\right), \qquad A_2 = \exp\left(-\frac{1}{2}\sigma_\lambda^2 q_{1,2}^2\right). \tag{S50}$$

Then the two phasors still produce fringes similarly to the coherent case, and one may write

$$\left|\mathcal{F}\{\tilde{I}_1\} + \mathcal{F}\{\tilde{I}_2\}\right| \approx \left|\widehat{O}(\mathbf{k}_\perp)\right| \left(A_1^2 + A_2^2 + 2A_1 A_2 \cos(q_{0,1} - q_{0,2})\right). \tag{S51}$$

The phase difference remains

$$q_{0,1} - q_{0,2} = \left(\sqrt{\left(\frac{2\pi}{\lambda_0}\right)^2 - \|\mathbf{k}_\perp + \mathbf{k}_{1\perp}\|^2} - \sqrt{\left(\frac{2\pi}{\lambda_0}\right)^2 - \|\mathbf{k}_\perp + \mathbf{k}_{2\perp}\|^2}\right) \Delta z + \text{Constant}, \tag{S52}$$

while the first-order (spectral) term mainly acts as a slow background modulation through the fringe contrast

$$\gamma_t = \frac{2\exp\left[-\frac{1}{2}\sigma_\lambda^2 \left(q_{1,1}^2 + q_{1,2}^2\right)\right]}{\exp\left(-\sigma_\lambda^2 q_{1,1}^2\right) + \exp\left(-\sigma_\lambda^2 q_{1,2}^2\right)}. \tag{S53}$$

Since γ_t varies slowly and only slightly reduces the fringe visibility (especially within the DAbI detection region), the fringe pattern is still governed primarily by the phase difference (S52), which is effectively equivalent to the ideal monochromatic case. Therefore, the DAbI method remains applicable to sources with finite spectral bandwidth, such as narrow-band LEDs.

To give a straightforward comparison, we performed simulations with parameters of $\lambda_0 = 5.2 \times 10^{-7}$ m, $\sigma_\lambda \approx 2 \times 10^{-8}$ m, NA=0.4, and a magnification of 20 (as shown in Fig. S7). From Fig. S7, we observe that the temporal partial coherence results in a subtle degradation of the fringe contrasts, but it has no effect on the fringe detections.

1.8 Theory extension to spatially partially coherent light

In the spatially partially coherent regime, each LED should be modeled as an extended emitter rather than an ideal point source. Without loss of generality, we place the origin at the intersection of the optical axis and the sample plane. The emitting area of the i-th LED is modeled as a square region of side length Δ centered at $(v_{i0}, w_{i0}, -h)$, where h denotes the distance between the LED plane and the sample plane, and i is the LED index. Following common fabrication conventions, the square emitting area is radially oriented

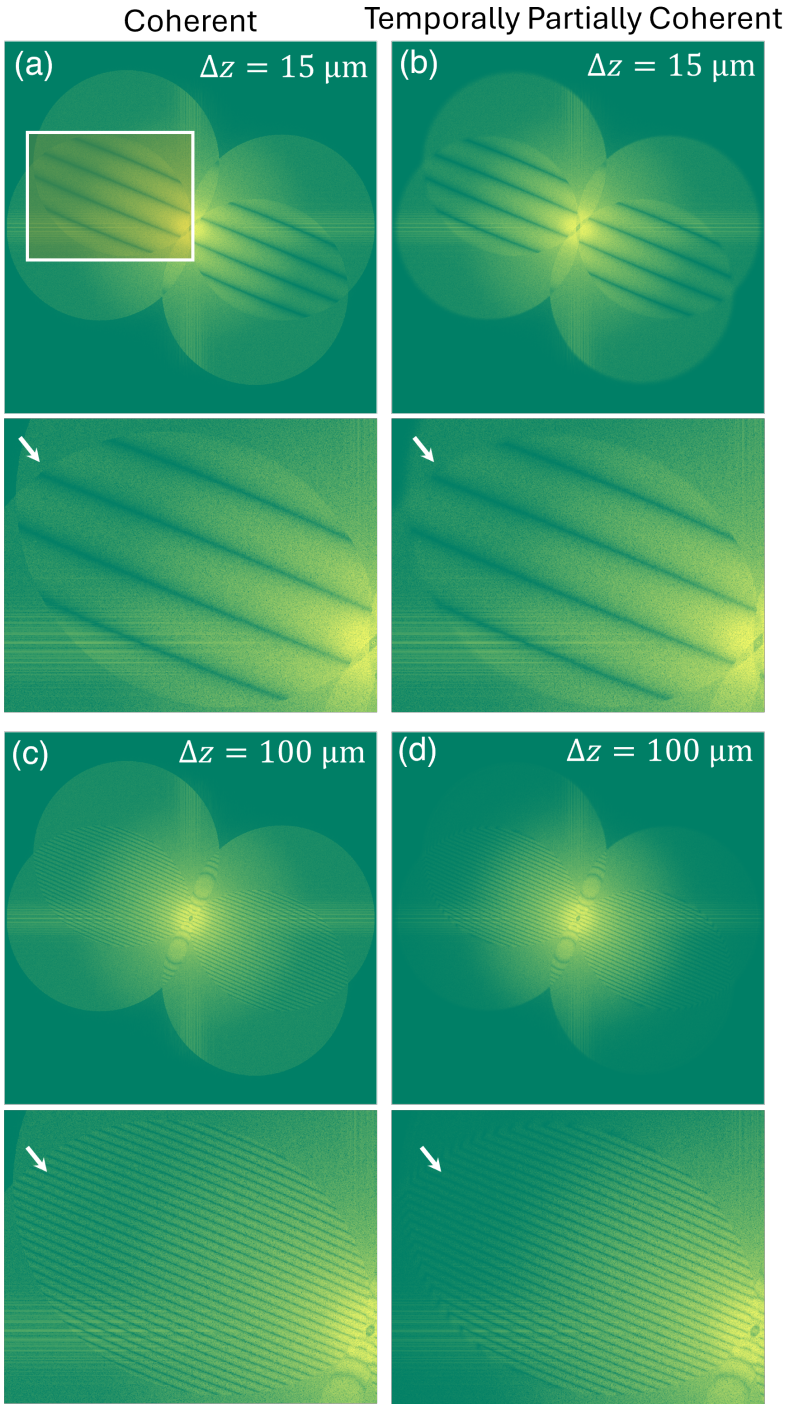

Figure S7: Simulations of coherent and temporally partially coherent light to show the effect of temporal partial coherence on DAbI fringes. **a**, Coherence and **b**, temporal partial coherent cases at defocus of 15 µm. **c**, Coherence and **d**, temporal partial coherent cases at defocus of 100 µm. The white arrows indicate the slight fringe contrast degradation in the zoomed-in regions.

with respect to the center of the LED array; i.e., its sides are aligned with the local radial and tangential directions in the LED plane.

Each differential element on the LED active area is treated as an independent point emitter that radiates a spherical wave with a random complex field amplitude $a(v_i, w_i)$. The illumination field at the sample plane is then

$$E(\mathbf{r}_\perp) = \iint_{\text{LED active area}} a(\mathbf{x}_i)\, \frac{\mathrm{e}^{jk_0\sqrt{(v_i-x)^2+(w_i-y)^2+h^2}}}{\sqrt{(v_i-x)^2+(w_i-y)^2+h^2}}\, \mathrm{d}v_i\, \mathrm{d}w_i, \tag{S54}$$

where $\mathbf{r}_\perp = (x, y)$ denotes the transverse coordinates on the sample plane, and $\mathbf{x}_i = (v_i, w_i)$ denotes the transverse coordinates on the LED plane. We assume distinct source points are mutually uncorrelated, i.e.,

$$\left\langle a(\mathbf{x}_i)\, a^*(\mathbf{x}_i')\right\rangle = I(\mathbf{x}_i)\, \delta(v_i - v_i')\, \delta(w_i - w_i'), \tag{S55}$$

where $I(v_i, w_i)$ is the source-plane intensity. We assume the intensity is uniform over the active area:

$$I(\mathbf{x}_i) = \begin{cases} I_0, & \mathbf{x}_i \in \mathcal{A}_i, \\ 0, & \text{otherwise.} \end{cases} \tag{S56}$$

The i-th LED active region $\mathcal{A}_i$ is parameterized as

$$\mathcal{A}_i := \left\{ \mathbf{x}_i \in \mathbb{R}^2 \;\middle|\; \mathbf{x}_i = \mathbf{x}_{i0} + v\, \widehat{\mathbf{e}}_{r,i} + w\, \widehat{\mathbf{e}}_{t,i},\ |v| < \frac{\Delta}{2},\ |w| < \frac{\Delta}{2} \right\}, \tag{S57}$$

where $\mathbf{x}_{i0} = (v_{i0}, w_{i0})$, and

$$\widehat{\mathbf{e}}_{r,i} = \left(\frac{v_{i0}}{\sqrt{v_{i0}^2 + w_{i0}^2}},\ \frac{w_{i0}}{\sqrt{v_{i0}^2 + w_{i0}^2}} \right), \tag{S58}$$

$$\widehat{\mathbf{e}}_{t,i} = \left(-\frac{w_{i0}}{\sqrt{v_{i0}^2 + w_{i0}^2}},\ \frac{v_{i0}}{\sqrt{v_{i0}^2 + w_{i0}^2}} \right) \tag{S59}$$

are the local radial (subscription $_r$) and tangential (subscription $_t$) unit vectors in the LED plane.

Because the sample field of view (FOV) is small and h is typically large, the paraxial and far-field approximations hold. Define

$$R_i = \sqrt{v_i^2 + w_i^2 + h^2}. \tag{S60}$$

Then the spherical-wave Green's function can be approximated as

$$\frac{\mathrm{e}^{jk_0\sqrt{(v_i-x)^2+(w_i-y)^2+h^2}}}{\sqrt{(v_i-x)^2+(w_i-y)^2+h^2}} \approx \frac{\mathrm{e}^{jk_0 R_i}}{R_i}\, \mathrm{e}^{-j\left(\frac{k_0 v_i}{R_i}x + \frac{k_0 w_i}{R_i}y\right)}. \tag{S61}$$

Substituting Eq. (S61) into Eq. (S54) yields

$$E(\mathbf{r}_\perp) = \iint_{\text{LED active area}} b(\mathbf{x}_i)\, \mathrm{e}^{-j\left(\frac{k_0 v_i}{R_i}x + \frac{k_0 w_i}{R_i}y\right)}\, \mathrm{d}v_i\, \mathrm{d}w_i, \tag{S62}$$

where

$$b(\mathbf{x}_i) = a(\mathbf{x}_i)\, \frac{\mathrm{e}^{jk_0 R_i}}{R_i} = a(\mathbf{x}_i)\, \frac{\mathrm{e}^{jk_0\sqrt{v_i^2+w_i^2+h^2}}}{\sqrt{v_i^2+w_i^2+h^2}}. \tag{S63}$$

Equation (S62) admits an interpretation as a superposition of plane-wave components. Define the transverse wavevector components

$$\mathbf{k}_{i\perp} = (k_{ix}, k_{iy}) = \left(-\frac{k_0 v_i}{R_i},\ -\frac{k_0 w_i}{R_i} \right), \tag{S64}$$

and rewrite the field as an integral over $\mathbf{k}_{i\perp}$:

$$E(\mathbf{r}_\perp) = \iint_{\mathbf{k}_{i\perp} \text{ corresponding to LED region}} W(\mathbf{k}_{i\perp})\, \mathrm{e}^{j\mathbf{k}_{i\perp}\cdot\mathbf{r}_\perp}\, \mathrm{d}\mathbf{k}_{i\perp}, \tag{S65}$$

where

$$W(\mathbf{k}_{i\perp}) = b(\mathbf{x}_i(\mathbf{k}_{i\perp}))\left|\det\left(\frac{\partial(v_i, w_i)}{\partial(k_{ix}, k_{iy})}\right)\right|. \tag{S66}$$

det denotes the determinant of a matrix and $\frac{\partial(v_i,w_i)}{\partial(k_{ix},k_{iy})}$ is the Jacobian matrix.

The mutual intensity of the illumination wavefront is defined by

$$J_{0,i}(\mathbf{r}_\perp, \mathbf{r}'_\perp) = \left\langle E(\mathbf{r}_\perp)E^*(\mathbf{r}'_\perp)\right\rangle = \iint\iint \left\langle W(\mathbf{k}_{i\perp})W^*(\mathbf{k}'_{i\perp})\right\rangle \mathrm{e}^{j\mathbf{k}_{i\perp}\cdot\mathbf{r}_\perp}\mathrm{e}^{-j\mathbf{k}'_{i\perp}\cdot\mathbf{r}'_\perp}\,\mathrm{d}\mathbf{k}_{i\perp}\,\mathrm{d}\mathbf{k}'_{i\perp}. \tag{S67}$$

Using Eqs. (S55), (S63), and (S66), one obtains

$$\left\langle W(\mathbf{k}_{i\perp})W^*(\mathbf{k}'_{i\perp})\right\rangle = I(\mathbf{x}_i)\,\frac{R_i^2}{k_0^2h^2}\,\delta(\mathbf{k}_{i\perp} - \mathbf{k}'_{i\perp}) = I(\mathbf{x}_i)\,\frac{v_i^2 + w_i^2 + h^2}{k_0^2h^2}\,\delta(\mathbf{k}_{i\perp} - \mathbf{k}'_{i\perp})\,. \tag{S68}$$

Recall that $I(\mathbf{x}_i) = I_0$ if and only if $\mathbf{x}_i \in \mathcal{A}_i$. The active region $\mathcal{A}_i$ maps to a slightly distorted rectangular region in $\mathbf{k}$-space. To characterize this mapping, consider a point in the active region

$$\mathbf{x}_i = \mathbf{x}_{i0} + v\,\widehat{\mathbf{e}}_{r,i} + w\,\widehat{\mathbf{e}}_{t,i}, \qquad |v| < \frac{\Delta}{2},\ |w| < \frac{\Delta}{2}. \tag{S69}$$

Its corresponding transverse wavevector is

$$\mathbf{k}_{i\perp} = \left(-\frac{k_0v_i}{R_i}, -\frac{k_0w_i}{R_i}\right) = -\frac{k_0\,(\mathbf{x}_{i0} + v\,\widehat{\mathbf{e}}_{r,i} + w\,\widehat{\mathbf{e}}_{t,i})}{\sqrt{\|\mathbf{x}_{i0} + v\,\widehat{\mathbf{e}}_{r,i} + w\,\widehat{\mathbf{e}}_{t,i}\|^2 + h^2}}. \tag{S70}$$

In typical experiments, the LED side length Δ is on the order of a few hundred micrometers and is much smaller than v_{i0}, w_{i0}, and h. Therefore, we expand to first order in (v, w). Let

$$R_{i0} = \sqrt{v_{i0}^2 + w_{i0}^2 + h^2}. \tag{S71}$$

Using $\|\mathbf{x}_{i0} + v\widehat{\mathbf{e}}_{r,i} + w\widehat{\mathbf{e}}_{t,i}\|^2 = \|\mathbf{x}_{i0}\|^2 + 2\|\mathbf{x}_{i0}\|v + \mathcal{O}(v^2 + w^2)$, we have

$$R_i = \sqrt{\|\mathbf{x}_{i0} + v\,\widehat{\mathbf{e}}_{r,i} + w\,\widehat{\mathbf{e}}_{t,i}\|^2 + h^2} \approx \sqrt{\|\mathbf{x}_{i0}\|^2 + 2\|\mathbf{x}_{i0}\|v + h^2} \approx R_{i0} + \frac{\|\mathbf{x}_{i0}\|}{R_{i0}}\,v. \tag{S72}$$

Substituting Eq. (S72) into Eq. (S70) and retaining only first-order terms yields

$$\mathbf{k}_{i\perp} \approx -\frac{k_0\,(\mathbf{x}_{i0} + v\,\widehat{\mathbf{e}}_{r,i} + w\,\widehat{\mathbf{e}}_{t,i})}{R_{i0}}\left(1 - \frac{\|\mathbf{x}_{i0}\|}{R_{i0}}v\right) \approx -\frac{k_0\mathbf{x}_{i0}}{R_{i0}} - \frac{k_0h^2}{R_{i0}^3}\,v\,\widehat{\mathbf{e}}_{r,i} - \frac{k_0}{R_{i0}}\,w\,\widehat{\mathbf{e}}_{t,i}. \tag{S73}$$

Define the central transverse wavevector

$$\mathbf{k}_{i\perp0} = (k_{ix0}, k_{iy0}) = -\frac{k_0\mathbf{x}_{i0}}{R_{i0}}. \tag{S74}$$

Then the LED square maps approximately to a rectangle in $\mathbf{k}$-space, as illustrated in Fig. S8:

$$\mathcal{Q}_i := \left\{\mathbf{k}_{i\perp} \in \mathbb{R}^2 \;\middle|\; \mathbf{k}_{i\perp} = \mathbf{k}_{i\perp0} + m\,\widehat{\mathbf{e}}_{r,i} + n\,\widehat{\mathbf{e}}_{t,i},\ |m| < \frac{k_0h^2}{R_{i0}^3}\frac{\Delta}{2},\ |n| < \frac{k_0}{R_{i0}}\frac{\Delta}{2}\right\}. \tag{S75}$$

Here the radial/tangential unit vectors in $\mathbf{k}$-space are

$$\widehat{\mathbf{e}}_{r,i} = \left(\frac{k_{ix0}}{\sqrt{k_{ix0}^2 + k_{iy0}^2}},\ \frac{k_{iy0}}{\sqrt{k_{ix0}^2 + k_{iy0}^2}}\right), \qquad \widehat{\mathbf{e}}_{t,i} = \left(-\frac{k_{iy0}}{\sqrt{k_{ix0}^2 + k_{iy0}^2}},\ \frac{k_{ix0}}{\sqrt{k_{ix0}^2 + k_{iy0}^2}}\right). \tag{S76}$$

With this approximation, Eq. (S68) reduces to

$$\left\langle W(\mathbf{k}_{i\perp})W^*(\mathbf{k}'_{i\perp})\right\rangle = \begin{cases} \dfrac{I_0}{k_0^2 - \|\mathbf{k}_{i\perp}\|^2}\,\delta(\mathbf{k}_{i\perp} - \mathbf{k}'_{i\perp})\,, & \mathbf{k}_{i\perp} \in \mathcal{Q}_i, \\ 0, & \text{otherwise.} \end{cases} \tag{S77}$$

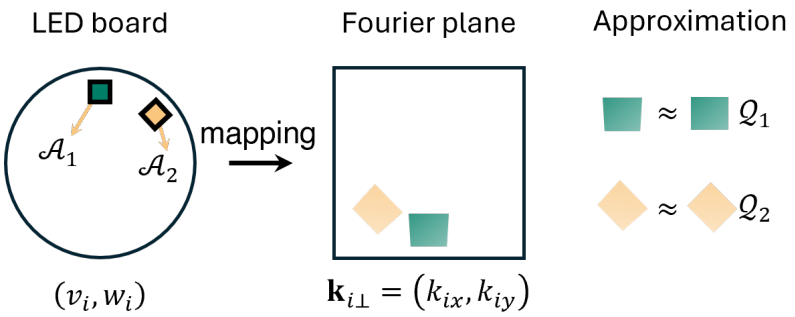

Figure S8: LED active area maps to an approximated rectangular area in **k**-space. The left panel shows the LEDs' positions in the spatial domain. The middle panel shows the LED active areas at the Fourier plane of the imaging system. The mapped regions are distorted rectangles. These regions can be approximated as rectangles for convenience in derivation (Eq. (S75)).

Defining

$$S(\mathbf{k}_{i\perp}) = \frac{I_0}{k_0^2 - \|\mathbf{k}_{i\perp}\|^2}, \tag{S78}$$

the mutual intensity of the illumination becomes

$$J_{0,i}(\mathbf{r}_\perp, \mathbf{r}'_\perp) = \iint_{\mathcal{Q}_i} S(\mathbf{k}_{i\perp})\, \mathrm{e}^{j\mathbf{k}_{i\perp}\cdot(\mathbf{r}_\perp - \mathbf{r}'_\perp)}\, \mathrm{d}\mathbf{k}_{i\perp}. \tag{S79}$$

Let the thin sample have transmittance $o(\mathbf{r}_\perp)$. Since the sample is deterministic, the mutual intensity immediately after the sample is

$$J_{s,i}(\mathbf{r}_\perp, \mathbf{r}'_\perp) = \left\langle o(\mathbf{r}_\perp) E(\mathbf{r}_\perp)\, E^*(\mathbf{r}'_\perp) o^*(\mathbf{r}'_\perp) \right\rangle = o(\mathbf{r}_\perp) o^*(\mathbf{r}'_\perp)\, J_{0,i}(\mathbf{r}_\perp, \mathbf{r}'_\perp). \tag{S80}$$

Let $h(\mathbf{r}_{\text{img}} - \mathbf{r}_\perp)$ denote the coherent point spread function (PSF) of the imaging system, where the subscription $_{\text{img}}$ indicates the coordinates at the image plane, and $_\perp$ is at the sample plane. The mutual intensity at the camera plane is

$$J_{\text{img},i}(\mathbf{r}_{\text{img}}, \mathbf{r}'_{\text{img}}) = \iint h(\mathbf{r}_{\text{img}} - \mathbf{r}_\perp)\, h^*(\mathbf{r}'_{\text{img}} - \mathbf{r}'_\perp)\, J_{s,i}(\mathbf{r}_\perp, \mathbf{r}'_\perp)\, \mathrm{d}\mathbf{r}_\perp\, \mathrm{d}\mathbf{r}'_\perp. \tag{S81}$$

The measured intensity is equivalent to the mutual intensity function ($J_{\text{img},i}$) at the coincident points:

$$I_i(\mathbf{r}_{\text{img}}) = J_{\text{img},i}(\mathbf{r}_{\text{img}}, \mathbf{r}_{\text{img}}). \tag{S82}$$

Substituting Eqs. (S79)–(S82) yields

$$I_i(\mathbf{r}_{\text{img}}) = \iint_{\mathcal{Q}_i} S(\mathbf{k}_{i\perp}) \left[\iint h(\mathbf{r}_{\text{img}} - \mathbf{r}_\perp)\, h^*(\mathbf{r}_{\text{img}} - \mathbf{r}'_\perp)\, \mathrm{e}^{j\mathbf{k}_{i\perp}\cdot(\mathbf{r}_\perp - \mathbf{r}'_\perp)}\, o(\mathbf{r}_\perp)\, o^*(\mathbf{r}'_\perp)\, \mathrm{d}\mathbf{r}_\perp\, \mathrm{d}\mathbf{r}'_\perp \right] \mathrm{d}\mathbf{k}_{i\perp}. \tag{S83}$$

The term in brackets can be factorized as

$$\iint h(\mathbf{r}_{\text{img}} - \mathbf{r}_\perp)\, h^*(\mathbf{r}_{\text{img}} - \mathbf{r}'_\perp)\, \mathrm{e}^{j\mathbf{k}_{i\perp}\cdot(\mathbf{r}_\perp - \mathbf{r}'_\perp)}\, o(\mathbf{r}_\perp)\, o^*(\mathbf{r}'_\perp)\, \mathrm{d}\mathbf{r}_\perp\, \mathrm{d}\mathbf{r}'_\perp = \left| \int h(\mathbf{r}_{\text{img}} - \mathbf{r}_\perp)\, \mathrm{e}^{j\mathbf{k}_{i\perp}\cdot\mathbf{r}_\perp}\, o(\mathbf{r}_\perp)\, \mathrm{d}\mathbf{r}_\perp \right|^2. \tag{S84}$$

Given the Fourier transform frequency shifting property and the convolution theorem, we have

$$\int h(\mathbf{r}_{\text{img}} - \mathbf{r}_\perp)\, \mathrm{e}^{j\mathbf{k}_{i\perp}\cdot\mathbf{r}_\perp}\, o(\mathbf{r}_\perp)\, \mathrm{d}\mathbf{r}_\perp = \mathcal{F}^{-1}\left\{ \widehat{O}(\mathbf{k}_\perp - \mathbf{k}_{i\perp})\, \widehat{P}(\mathbf{k}_\perp) \right\}, \tag{S85}$$

where $\widehat{O}$ and $\widehat{P}$ are the Fourier transforms of the object and pupil function, respectively. Substituting Eqs. (S84) and (S85) into Eq. (S83) gives

$$I_i(\mathbf{r}_{\text{img}}) = \iint_{\mathcal{Q}_i} S(\mathbf{k}_{i\perp}) \left| \mathcal{F}^{-1}\left\{ \widehat{O}(\mathbf{k}_\perp - \mathbf{k}_{i\perp})\, \widehat{P}(\mathbf{k}_\perp) \right\} \right|^2 \mathrm{d}\mathbf{k}_{i\perp}. \tag{S86}$$

Equation (S86) shows that, under spatially partial coherence, an extended LED can be decomposed into many small coherent components, each following the coherent forward model. The measured intensity is the incoherent superposition of these components. For each component, the coherent model from Note 1.1 and 1.2 is still valid. The results from Eq. (S12) can still be used to present the summation of intensity spectra from two LED illuminations,

$$\begin{aligned}\mathcal{F}\{I_1\}+\mathcal{F}\{I_2\} = &\iint_{\mathcal{Q}_1} S(\mathbf{k}_{1\perp})\,\widehat{O}(\mathbf{k}_\perp)\,\widehat{P}(\mathbf{k}_\perp+\mathbf{k}_{1\perp})\,\widehat{P}^*(\mathbf{k}_{1\perp})\,\mathrm{d}\mathbf{k}_{1\perp}\\ &+\iint_{\mathcal{Q}_2} S(\mathbf{k}_{2\perp})\,\widehat{O}(\mathbf{k}_\perp)\,\widehat{P}(\mathbf{k}_\perp+\mathbf{k}_{2\perp})\,\widehat{P}^*(\mathbf{k}_{2\perp})\,\mathrm{d}\mathbf{k}_{2\perp}\\ &+\iint_{\mathcal{Q}_1} S(\mathbf{k}_{1\perp})\,\widehat{O}^*(-\mathbf{k}_\perp)\,\widehat{P}^*(-\mathbf{k}_\perp+\mathbf{k}_{1\perp})\,\widehat{P}(\mathbf{k}_{1\perp})\,\mathrm{d}\mathbf{k}_{1\perp}\\ &+\iint_{\mathcal{Q}_2} S(\mathbf{k}_{2\perp})\,\widehat{O}^*(-\mathbf{k}_\perp)\,\widehat{P}^*(-\mathbf{k}_\perp+\mathbf{k}_{2\perp})\,\widehat{P}(\mathbf{k}_{2\perp})\,\mathrm{d}\mathbf{k}_{2\perp}. \end{aligned} \tag{S87}$$

Here, unlike the derivation from Eq. (S11) to Eq. (S14), we do *not* absorb the constant phase factors $\widehat{P}^*(\mathbf{k}_{1\perp})$ and $\widehat{P}^*(\mathbf{k}_{2\perp})$ into the overall normalization, because these factors also depend on the LED area.

In the coherent case, with appropriate illumination design, there exists a spectral region where only the first two terms survive. In the partially coherent case, different $\mathbf{k}_{i\perp}$ within the same LED region lead to slightly different pupil shifts. However, when the LED active area is sufficiently small, the deviation from the central wavevector $\mathbf{k}_{i\perp 0}$ is small (e.g., $< 0.4\%$ in our setting). Therefore, there exists a region $\mathcal{S}'$ such that for all $\mathbf{k}_{1\perp}\in\mathcal{Q}_1$ and $\mathbf{k}_{2\perp}\in\mathcal{Q}_2$, the coherent-case separation conditions still hold, which is defined as,

$$\mathcal{S}' = \left\{ \mathbf{k}_\perp\in\mathbb{R}^2 \;\middle|\; \begin{array}{l} \|\mathbf{k}_\perp+\mathbf{k}_{1\perp}\|\le k_0\,\mathrm{NA},\\ \|\mathbf{k}_\perp+\mathbf{k}_{2\perp}\|\le k_0\,\mathrm{NA},\\ \|\mathbf{k}_\perp-\mathbf{k}_{1\perp}\|> k_0\,\mathrm{NA},\\ \|\mathbf{k}_\perp-\mathbf{k}_{2\perp}\|> k_0\,\mathrm{NA} \end{array} \forall\,\mathbf{k}_{1\perp}\in\mathcal{Q}_1,\ \forall\,\mathbf{k}_{2\perp}\in\mathcal{Q}_2 \right\}. \tag{S88}$$

In this region,

$$\begin{aligned}\mathcal{F}\{I_1\}+\mathcal{F}\{I_2\} \approx &\iint_{\mathcal{Q}_1} S(\mathbf{k}_{1\perp})\,\widehat{O}(\mathbf{k}_\perp)\,\widehat{P}(\mathbf{k}_\perp+\mathbf{k}_{1\perp})\,\widehat{P}^*(\mathbf{k}_{1\perp})\,\mathrm{d}\mathbf{k}_{1\perp}\\ &+\iint_{\mathcal{Q}_2} S(\mathbf{k}_{2\perp})\,\widehat{O}(\mathbf{k}_\perp)\,\widehat{P}(\mathbf{k}_\perp+\mathbf{k}_{2\perp})\,\widehat{P}^*(\mathbf{k}_{2\perp})\,\mathrm{d}\mathbf{k}_{2\perp}, \qquad \mathbf{k}_\perp\in\mathcal{S}'. \end{aligned} \tag{S89}$$

Given $S(\mathbf{k}_\perp)$ in Eq. (S78), $\widehat{O}(\mathbf{k}_\perp)=\widehat{A}(\mathbf{k}_\perp)\mathrm{e}^{j\widehat{\eta}(\mathbf{k}_\perp)}$, and $\widehat{P}(\mathbf{k}_\perp)=\mathbb{1}(|\mathbf{k}_\perp|\le k_0\mathrm{NA})\,e^{j\widehat{\phi}(\mathbf{k}_\perp)}$, we obtain

$$\mathcal{F}\{I_1\}+\mathcal{F}\{I_2\} \approx I_0\,\widehat{A}(\mathbf{k}_\perp)\,\mathrm{e}^{j\widehat{\eta}(\mathbf{k}_\perp)}\left[\iint_{\mathcal{Q}_1}\frac{\mathrm{e}^{j\left[\widehat{\phi}(\mathbf{k}_\perp+\mathbf{k}_{1\perp})-\widehat{\phi}(\mathbf{k}_{1\perp})\right]}}{k_0^2-\|\mathbf{k}_{1\perp}\|^2}\,\mathrm{d}\mathbf{k}_{1\perp}+\iint_{\mathcal{Q}_2}\frac{\mathrm{e}^{j\left[\widehat{\phi}(\mathbf{k}_\perp+\mathbf{k}_{2\perp})-\widehat{\phi}(\mathbf{k}_{2\perp})\right]}}{k_0^2-\|\mathbf{k}_{2\perp}\|^2}\mathrm{d}\mathbf{k}_{2\perp}\right], \tag{S90}$$

where the defocus phase is $\widehat{\phi}(\mathbf{k}_\perp)=\sqrt{k_0^2-|\mathbf{k}_\perp|^2}\,\Delta z$ (Eq. (S19)).

Consider one of the integrals in Eq. (S90). Given that $\mathbf{k}_{i\perp}$ lies within $\mathcal{Q}_i$, it can be parameterized as $\mathbf{k}_{i\perp}=\mathbf{k}_{i\perp 0}+m\widehat{\mathbf{e}}_{r,i}+n\widehat{\mathbf{e}}_{t,i}$. We write

$$\iint_{\mathcal{Q}_i}\frac{\mathrm{e}^{j\left[\widehat{\phi}(\mathbf{k}_\perp+\mathbf{k}_{i\perp})-\widehat{\phi}(\mathbf{k}_{i\perp})\right]}}{k_0^2-\|\mathbf{k}_{i\perp}\|^2}\,\mathrm{d}\mathbf{k}_{i\perp}=\int_{-k_{r,i}}^{k_{r,i}}\int_{-k_{t,i}}^{k_{t,i}}\frac{\mathrm{e}^{j\left[\widehat{\phi}(\mathbf{k}_\perp+\mathbf{k}_{i\perp 0}+m\widehat{\mathbf{e}}_{r,i}+n\widehat{\mathbf{e}}_{t,i})-\widehat{\phi}(\mathbf{k}_{i\perp 0}+m\widehat{\mathbf{e}}_{r,i}+n\widehat{\mathbf{e}}_{t,i})\right]}}{k_0^2-\|\mathbf{k}_{i\perp 0}+m\widehat{\mathbf{e}}_{r,i}+n\widehat{\mathbf{e}}_{t,i}\|^2}\,\mathrm{d}n\,\mathrm{d}m, \tag{S91}$$

where $k_{r,i}$ and $k_{t,i}$ are bounds for the LED active region mapped area in the $\mathbf{k}$-space Eq. (S75):

$$k_{r,i}=\frac{k_0h^2}{R_{i0}^3}\frac{\Delta}{2}, \qquad k_{t,i}=\frac{k_0}{R_{i0}}\frac{\Delta}{2}. \tag{S92}$$

Define the deviation from the central wavevector as $\boldsymbol{\epsilon}=\mathbf{k}_{i\perp}-\mathbf{k}_{i\perp 0}=m\widehat{\mathbf{e}}_{r,i}+n\widehat{\mathbf{e}}_{t,i}$. Then

$$\frac{1}{k_0^2-\|\mathbf{k}_{i\perp}\|^2}=\frac{1}{k_0^2-\|\mathbf{k}_{i\perp 0}+\boldsymbol{\epsilon}\|^2}=\frac{1}{k_0^2-\|\mathbf{k}_{i\perp 0}\|^2-2\mathbf{k}_{i\perp 0}\cdot\boldsymbol{\epsilon}-\|\boldsymbol{\epsilon}\|^2}. \tag{S93}$$

With representative experimental scales (e.g., $h, R_{i0} \sim 10^{-1}\,\mathrm{m}$, $k_0 = 2\pi/\lambda \sim 10^{7}\,\mathrm{m}^{-1}$, $\Delta \sim 10^{-4}\,\mathrm{m}$, and $\|\mathbf{k}_{i\perp 0}\| \sim 0.4\,k_0$), the term $2\mathbf{k}_{i\perp 0}\cdot\boldsymbol{\epsilon}$ is first-order small and $\|\boldsymbol{\epsilon}\|^2$ is second-order small. Moreover, one can bound

$$\frac{|2\mathbf{k}_{i\perp 0}\cdot\boldsymbol{\epsilon}|}{k_0^2 - \|\mathbf{k}_{i\perp 0}\|^2} \le \frac{2\|\mathbf{k}_{i\perp 0}\|\,\|\boldsymbol{\epsilon}\|}{k_0^2 - \|\mathbf{k}_{i\perp 0}\|^2} \ll 1, \tag{S94}$$

hence the amplitude factor is slowly varying over $\mathcal{Q}_i$ and can be approximated by its value at the center:

$$\frac{1}{k_0^2 - \|\mathbf{k}_{i\perp}\|^2} \approx \frac{1}{k_0^2 - \|\mathbf{k}_{i\perp 0}\|^2}. \tag{S95}$$

For the phase term, we can also expand the phase difference

$$\begin{aligned}
\widehat{\phi}(\mathbf{k}_\perp + \mathbf{k}_{i\perp}) - \widehat{\phi}(\mathbf{k}_{i\perp}) = &\left(\sqrt{k_0^2 - \|\mathbf{k}_\perp + \mathbf{k}_{i\perp 0}\|^2} - \sqrt{k_0^2 - \|\mathbf{k}_{i\perp 0}\|^2}\right)\Delta z \\
&- \left(\frac{(\mathbf{k}_\perp + \mathbf{k}_{i\perp 0})\cdot\boldsymbol{\epsilon}}{\sqrt{k_0^2 - \|\mathbf{k}_\perp + \mathbf{k}_{i\perp 0}\|^2}} - \frac{\mathbf{k}_{i\perp 0}\cdot\boldsymbol{\epsilon}}{\sqrt{k_0^2 - \|\mathbf{k}_{i\perp 0}\|^2}}\right)\Delta z \\
&- \frac{\Delta z}{2}\left[\frac{\|\boldsymbol{\epsilon}\|^2}{\sqrt{k_0^2 - \|\mathbf{k}_\perp + \mathbf{k}_{i\perp 0}\|^2}} - \frac{\|\boldsymbol{\epsilon}\|^2}{\sqrt{k_0^2 - \|\mathbf{k}_{i\perp 0}\|^2}}\right. \\
&\left. + \frac{\left[(\mathbf{k}_\perp + \mathbf{k}_{i\perp 0})\cdot\boldsymbol{\epsilon}\right]^2}{\left(k_0^2 - \|\mathbf{k}_\perp + \mathbf{k}_{i\perp 0}\|^2\right)^{3/2}} - \frac{(\mathbf{k}_{i\perp 0}\cdot\boldsymbol{\epsilon})^2}{\left(k_0^2 - \|\mathbf{k}_{i\perp 0}\|^2\right)^{3/2}}\right] + \mathcal{O}(\|\boldsymbol{\epsilon}\|^3).
\end{aligned} \tag{S96}$$

In our setting (with a maximum defocus on the order of $\sim 600\,\mu$m), the quadratic contribution in Eqs. (S96) is typically below 10^{-2} radians and can be neglected, whereas the linear term can be non-negligible, especially at larger defocus. Therefore, using Eq. (S95) (S96) and retaining the linear phase term, Eq. (S91) becomes

$$\begin{aligned}
\iint_{\mathcal{Q}_i} \frac{\mathrm{e}^{j\left[\widehat{\phi}(\mathbf{k}_\perp + \mathbf{k}_{i\perp}) - \widehat{\phi}(\mathbf{k}_{i\perp})\right]}}{k_0^2 - \|\mathbf{k}_{i\perp}\|^2}\,\mathrm{d}\mathbf{k}_{i\perp} \;\approx\; &\frac{\mathrm{e}^{j\left(\sqrt{k_0^2 - \|\mathbf{k}_\perp + \mathbf{k}_{i\perp 0}\|^2} - \sqrt{k_0^2 - \|\mathbf{k}_{i\perp 0}\|^2}\right)\Delta z}}{k_0^2 - \|\mathbf{k}_{i\perp 0}\|^2} \\
&\times \int_{-k_{r,i}}^{k_{r,i}} \int_{-k_{t,i}}^{k_{t,i}} \mathrm{e}^{-j\,\mathbf{g}_i\cdot\boldsymbol{\epsilon}\,\Delta z}\,\mathrm{d}n\,\mathrm{d}m.
\end{aligned} \tag{S97}$$

where

$$\mathbf{g}_i = \frac{\mathbf{k}_\perp + \mathbf{k}_{i\perp 0}}{\sqrt{k_0^2 - \|\mathbf{k}_\perp + \mathbf{k}_{i\perp 0}\|^2}} - \frac{\mathbf{k}_{i\perp 0}}{\sqrt{k_0^2 - \|\mathbf{k}_{i\perp 0}\|^2}}. \tag{S98}$$

Given that $\boldsymbol{\epsilon} = m\widehat{\mathbf{e}}_{r,i} + n\widehat{\mathbf{e}}_{t,i}$, we can define

$$g_{r,i} = -(\mathbf{g}_i\cdot\widehat{\mathbf{e}}_{r,i})\,\Delta z, \qquad g_{t,i} = -(\mathbf{g}_i\cdot\widehat{\mathbf{e}}_{t,i})\,\Delta z. \tag{S99}$$

Thus, in Eq. (S97),

$$\mathbf{g}_i\cdot\boldsymbol{\epsilon}\,\Delta z = m\,g_{r,i} + n\,g_{t,i}.$$

Then the integral separates along the orthogonal axes $\widehat{\mathbf{e}}_{r,i}$ and $\widehat{\mathbf{e}}_{t,i}$, yielding

$$\begin{aligned}
\iint_{\mathcal{Q}_i} \frac{\mathrm{e}^{j\left[\widehat{\phi}(\mathbf{k}_\perp + \mathbf{k}_{i\perp}) - \widehat{\phi}(\mathbf{k}_{i\perp})\right]}}{k_0^2 - \|\mathbf{k}_{i\perp}\|^2}\,\mathrm{d}\mathbf{k}_{i\perp} \;&\approx\; \frac{4k_{r,i}k_{t,i}}{k_0^2 - \|\mathbf{k}_{i\perp 0}\|^2}\,\mathrm{sinc}(g_{r,i}k_{r,i})\,\mathrm{sinc}(g_{t,i}k_{t,i}) \\
&\quad\times \mathrm{e}^{j\left(\sqrt{k_0^2 - \|\mathbf{k}_\perp + \mathbf{k}_{i\perp 0}\|^2} - \sqrt{k_0^2 - \|\mathbf{k}_{i\perp 0}\|^2}\right)\Delta z} \\
&=\; C_i(\mathbf{k}_\perp)\,\mathrm{e}^{j\left(\sqrt{k_0^2 - \|\mathbf{k}_\perp + \mathbf{k}_{i\perp 0}\|^2} - \sqrt{k_0^2 - \|\mathbf{k}_{i\perp 0}\|^2}\right)\Delta z}.
\end{aligned} \tag{S100}$$

where (with $\mathrm{sinc}(x) = \sin(x)/x$)

$$C_i(\mathbf{k}_\perp) = \frac{4k_{r,i}k_{t,i}}{k_0^2 - \|\mathbf{k}_{i\perp 0}\|^2}\,\mathrm{sinc}(g_{r,i}k_{r,i})\,\mathrm{sinc}(g_{t,i}k_{t,i}). \tag{S101}$$

Using $R_{i0} = k_0 h / \sqrt{k_0^2 - \|\mathbf{k}_{i\perp 0}\|^2}$, from Eq. (S92) one may rewrite

$$
\begin{aligned}
g_{r,i} k_{r,i} &= - \left[\frac{(\mathbf{k}_\perp + \mathbf{k}_{i\perp 0}) \cdot \widehat{\mathbf{e}}_{r,i}}{\sqrt{k_0^2 - \|\mathbf{k}_\perp + \mathbf{k}_{i\perp 0}\|^2}} - \frac{\|\mathbf{k}_{i\perp 0}\|}{\sqrt{k_0^2 - \|\mathbf{k}_{i\perp 0}\|^2}} \right] \frac{\Delta z \, (k_0^2 - \|\mathbf{k}_{i\perp 0}\|^2)^{3/2}}{2 k_0^2 h} \, \Delta, \\
g_{t,i} k_{t,i} &= - \frac{(\mathbf{k}_\perp + \mathbf{k}_{i\perp 0}) \cdot \widehat{\mathbf{e}}_{t,i}}{\sqrt{k_0^2 - \|\mathbf{k}_\perp + \mathbf{k}_{i\perp 0}\|^2}} \frac{\Delta z \, (k_0^2 - \|\mathbf{k}_{i\perp 0}\|^2)^{1/2}}{2h} \, \Delta.
\end{aligned} \tag{S102}
$$

Consequently, the magnitude of the left-hand side of Eq. (S90) can be expressed as

$$
\begin{aligned}
|\mathcal{F}\{I_1\} + \mathcal{F}\{I_2\}| = I_0 \, |\widehat{A}(\mathbf{k}_\perp)| \Big| & C_1(\mathbf{k}_\perp) \, \mathrm{e}^{j\left(\sqrt{k_0^2 - \|\mathbf{k}_\perp + \mathbf{k}_{1\perp 0}\|^2} - \sqrt{k_0^2 - \|\mathbf{k}_{1\perp 0}\|^2}\right) \Delta z} \\
& + C_2(\mathbf{k}_\perp) \, \mathrm{e}^{j\left(\sqrt{k_0^2 - \|\mathbf{k}_\perp + \mathbf{k}_{2\perp 0}\|^2} - \sqrt{k_0^2 - \|\mathbf{k}_{2\perp 0}\|^2}\right) \Delta z} \Big|
\end{aligned} \tag{S103}
$$

The two phasors still generate fringes similarly to the coherent case; under partial coherence, the fringe contrast is modulated by $C_i(\mathbf{k}_\perp)$:

$$
\gamma_s = \frac{2 |C_1(\mathbf{k}_\perp)| \, |C_2(\mathbf{k}_\perp)|}{|C_1(\mathbf{k}_\perp)|^2 + |C_2(\mathbf{k}_\perp)|^2}, \qquad C_i(\mathbf{k}_\perp) = \frac{k_0^2 - \|\mathbf{k}_{i\perp 0}\|^2}{2 k_0^2 h^2} \, \mathrm{sinc}(g_{r,i} k_{r,i}) \, \mathrm{sinc}(g_{t,i} k_{t,i}). \tag{S104}
$$

The contrast is maximized when $|C_1(\mathbf{k}_\perp)| = |C_2(\mathbf{k}_\perp)|$. At small defocus distances (e.g., within ~ 20 depth of field, DoF, $g_{r,i} k_{r,i}$ and $g_{t,i} k_{t,i}$ (Eq. (S102)) are sufficiently small so that both sinc factors are close to 1. Moreover, when the two LEDs are chosen to have similar polar illumination angles β_1, β_2 (Fig. S3, and Note 3 e.g., near NA-matching), one typically has $\|\mathbf{k}_{1\perp 0}\|^2 \approx \|\mathbf{k}_{2\perp 0}\|^2$, implying $C_1(\mathbf{k}_\perp) \approx C_2(\mathbf{k}_\perp)$ and thus high fringe contrast across $\mathcal{S}'$. At large defocus distances, the difference between the sinc factors of C_1 and C_2 may become non-negligible, and the fringes over $\mathcal{S}'$ are modulated by γ_s. In practice, for large defocus the system transfer function at high spatial frequencies is weak and measurement noise dominates; thus the useful spectrum is concentrated on near zeroth-frequency, i.e., $\|\mathbf{k}_\perp\| \ll k_0$, which is also the typical operating region of DAbI (Algorithm 1 line 6). In this regime,

$$
g_{r,i} k_{r,i} \ll 1, \qquad g_{t,i} k_{t,i} \ll 1, \tag{S105}
$$

$C_1(\mathbf{k}_\perp)$ and $C_2(\mathbf{k}_\perp)$ remain close, yielding high contrast that enables reliable defocus extraction.

Our simulation results also align with the same conclusion above (Fig. S9). From Fig. S9, we observe that the spatial partial coherence has little effect at small defocus distances, while at large defocus distances, the fringes contrast at the high spatial frequency is degraded. As discussed in the previous paragraph, at large defocus distances, the useful spectrum is concentrated on near zeroth-frequency; thus, the fringe degradation has little effect on defocus detection (Algorithm 1).

In summary, the temporally and spatially partially coherent light may influence the contrast of the DAbI fringes, but has little impact on the fringe detection.

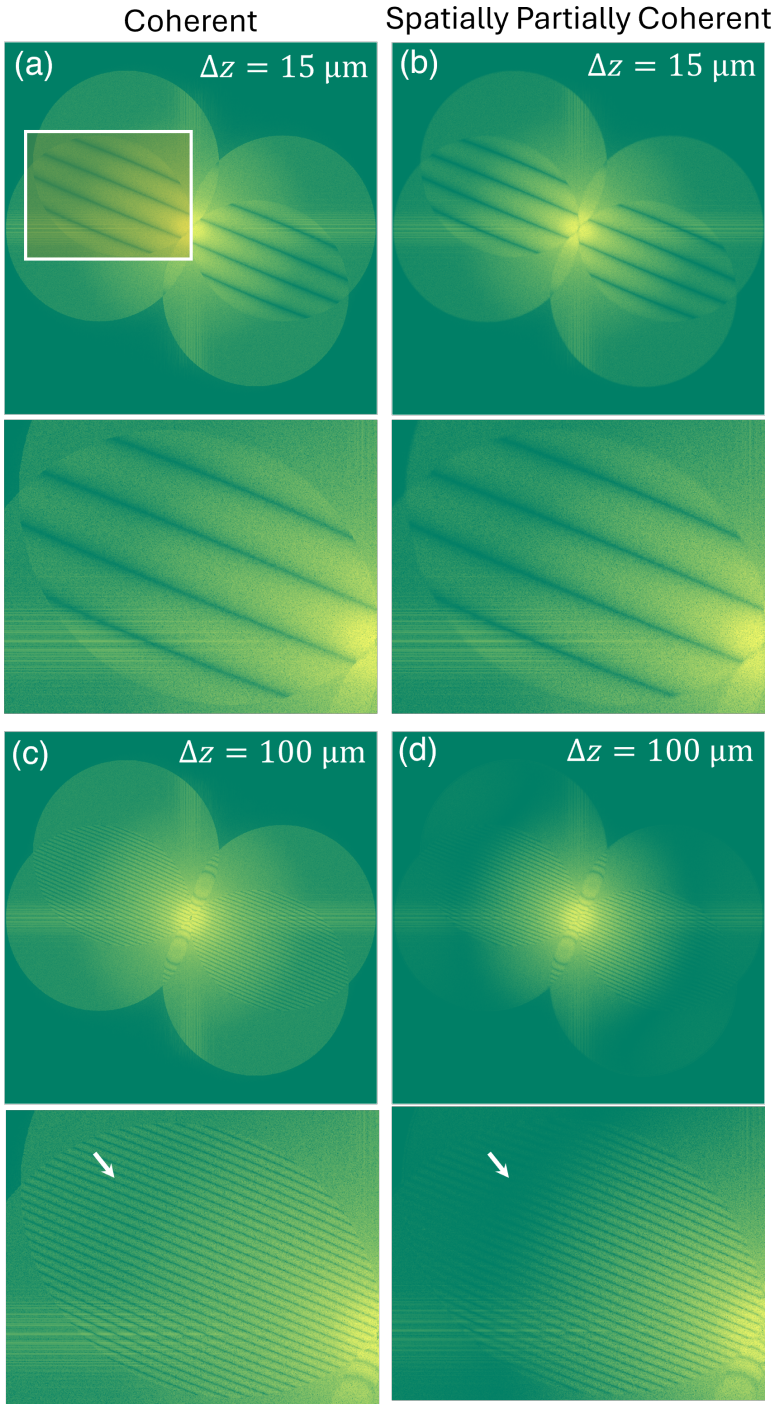

Figure S9: Simulations of coherent and spatially partially coherent light to show the effect of spatial partial coherence on DAbI fringes. **a**, Coherence and **b**, spatial partial coherent cases at defocus of 15 µm. **c**, Coherence and **d**, spatial partial coherent cases at defocus of 100 µm. The white arrows indicate the slight fringe contrast degradation in the zoomed-in regions.

2 Derivation of DAbI in 3D case

2.1 Image formation forward model for thick samples

Here, we aim to generalize 2D cases to thick samples for the above derivations. According to the Fourier diffraction theorem [1], for thick samples, the support of the coherent transfer function will extend from a 2D circular region to a 3D spherical cap on the Ewald sphere (Fig. S10). As a result, the intensity measurements contain the 2D projection of sample spectra on shifted 3D spherical caps. Later, we will demonstrate that, if we set the two illumination angles to be the same relative to the optical axis and incorporate finite sample thickness prior [2], the established DAbI method can be effectively generalized to handle thick samples with small modifications.

We start by introducing the imaging forward model for 3D thick samples. Let $n(\mathbf{r})$ be the refractive index distribution of the sample, $\mathbf{r} = (\mathbf{r}_\perp, z)$ be the spatial coordinate in 3D space, n_m be the refractive index of the background media, the 3D sample scattering potential is defined as

$$o(\mathbf{r}) \coloneqq k_0^2 \left(n(\mathbf{r})^2 - n_m^2\right). \tag{S106}$$

When this 3D sample is illuminated by plane waves $u_{in}(\mathbf{r}; \mathbf{k}_i)$ with the 3D wavevectors $\mathbf{k}_i = (\mathbf{k}_{i\perp}, k_{iz})$, the total field $u(\mathbf{r})$ obeys the inhomogeneous Helmholtz equation:

$$(\nabla^2 + k_m^2)u(\mathbf{r}) = -o(\mathbf{r})u(\mathbf{r}), \tag{S107}$$

where ∇^2 denotes the Laplace operator, $k_m \coloneqq k_0 n_m$ is the wavenumber in media. The total field can be decomposed into the incident field (unscattered field) and the scattered field,

$$u(\mathbf{r}) = u_{in}(\mathbf{r}; \mathbf{k}_i) + u_s(\mathbf{r}),$$

and solved under the first-order Born approximation as

$$u(\mathbf{r}) = u_{in}(\mathbf{r}; \mathbf{k}_i) + \int g(\mathbf{r} - \mathbf{r}')o(\mathbf{r}')u_{in}(\mathbf{r}'; \mathbf{k}_i)\, d\mathbf{r}', \tag{S108}$$

$g(\mathbf{r})$ is the 3D Green's function:

$$g(\mathbf{r}) = \frac{e^{jk_m|\mathbf{r}|}}{4\pi|\mathbf{r}|}. \tag{S109}$$

Taking the Fourier transform on both sides of Eq. (S108) and only considering forward scattered lights:

$$\widehat{U}(\mathbf{k}) = (2\pi)^3\delta(\mathbf{k} - \mathbf{k}_i) + \widehat{O}(\mathbf{k} - \mathbf{k}_i)\widehat{G}(\mathbf{k}). \tag{S110}$$

Here, $\widehat{O}(\mathbf{k}) = \mathcal{F}_{3D}\{o(\mathbf{r})\}$ is the 3D sample scattering potential spectrum, $\mathbf{k} = (\mathbf{k}_\perp, k_z)$ is the 3D spatial frequency coordinate, and

$$\widehat{G}(\mathbf{k}) = \frac{1}{k_m^2 - |\mathbf{k}|^2 + i0^+}. \tag{S111}$$

Using the Sokhotski–Plemelj identity[3], $\widehat{G}(\mathbf{k})$ can be decomposed into a near-field part and a radiative part. In our case, the Fourier transform property of the objective lens transmits the optical field in a radiative manner. Thus, we do not account for the near-field contribution. Therefore,

$$\widehat{G}(\mathbf{k}) \approx -j\pi\delta(k_m^2 - |\mathbf{k}|^2), \tag{S112}$$

$$\widehat{U}(\mathbf{k}) = (2\pi)^3\delta(\mathbf{k} - \mathbf{k}_i) - j\pi\delta(k_m^2 - |\mathbf{k}|^2)\widehat{O}(\mathbf{k} - \mathbf{k}_i), \tag{S113}$$

$\widehat{U}(\mathbf{k})$ is the 3D Fourier transform of the 3D total optical field. Given that the lens and the camera are 2D components, the imaging system only captures information from the wavefront of one plane. Additionally, we only consider forward scattering in this modeling. Therefore, for the forward model we care more about

the optical field at the focal plane of the objective $z = z_f$, namely $u(\mathbf{r}_\perp, z_f)$ and its 2D spectrum $\widehat{U}_\perp(\mathbf{k}_\perp; z_f)$. Performing 1D Fourier transform for Eq. (S113) and set $z = z_f$ gives,

$$\begin{aligned}\widehat{U}_\perp(\mathbf{k}_\perp; z_f) &= \frac{1}{2\pi}\int_{-\infty}^{+\infty} \widehat{U}(\mathbf{k}) e^{jk_z z_f}\, dk_z \\ &= (2\pi)^2 \delta(\mathbf{k}_\perp - \mathbf{k}_{i\perp}) e^{jk_{iz} z_f} \\ &\quad - \frac{j}{4\sqrt{k_m^2 - |\mathbf{k}_\perp|^2}} \widehat{O}(\mathbf{k}_\perp - \mathbf{k}_{i\perp}, \sqrt{k_m^2 - |\mathbf{k}_\perp|^2} - k_{iz}) e^{j\sqrt{k_m^2 - |\mathbf{k}_\perp|^2} z_f}. \end{aligned} \tag{S114}$$

This is the direct result from the Fourier diffraction theorem [1, 4].

Similar to the 2D case, this 2D wavefront $\widehat{U}_\perp(\mathbf{k}_\perp; z_f)$ propagates through a conventional $4f$ system and is captured by the 2D camera. Similar to Eq. (S2), we have

$$I_i = \left| \mathcal{F}_{2D}^{-1} \left\{ \widehat{U}_\perp(\mathbf{k}_\perp; z_f)\, \widehat{P}(\mathbf{k}_\perp) \right\} \right|^2, \quad i = 1, 2 \tag{S115}$$

where I_i is the ith intensity measurement, $\mathcal{F}_{2D}^{-1}\{\cdot\}$ denotes the 2D inverse Fourier transform, and $\widehat{P}(\mathbf{k}_\perp)$ is the imaging system's coherent transfer function:

$$\widehat{P}(\mathbf{k}_\perp) = \mathbf{1}_{|\mathbf{k}_\perp| \le k_0 \mathrm{NA}} \cdot e^{j\widehat{\phi}(\mathbf{k}_\perp)}$$

where $k_0 = 2\pi/\lambda$ is the free-space wavenumber and $\widehat{\phi}(\mathbf{k}_\perp)$ denotes the system aberration. When the sample is defocused by Δz, the optical path in the free space between the sample and the objective lens changes, resulting in defocus aberration. This aberration can be expressed as

$$\widehat{\phi}(\mathbf{k}_\perp) = e^{j\sqrt{k_0^2 - |\mathbf{k}_\perp|^2}\, \Delta z} \tag{S116}$$

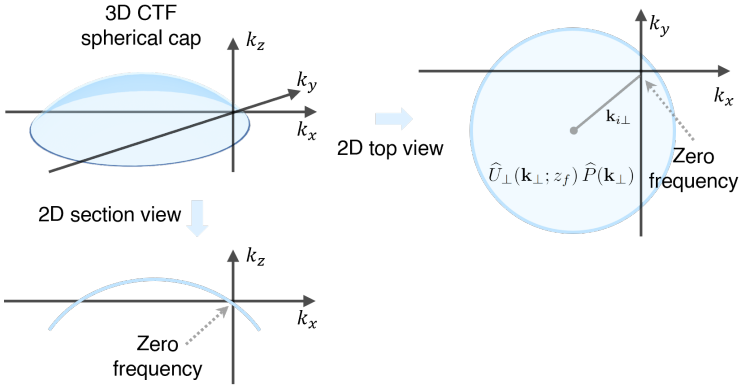

Figure S10: 3D coherent transfer function from an oblique illumination angle is a 3D spherical cap on the Ewald sphere.

2.2 Nominal in-focus plane of thick samples

In 2D thin samples, the sample plane can be considered as a 2D plane. The autofocusing task is to align this 2D plane with the focal plane of the imaging system. However, in thick samples, the sample content expands over a range of axial extension. Determining which sample plane to align with the system focal plane is of significant importance. There exists a 2D sample plane that DAbI fringes will be perfectly compensated when this 2D plane is aligned with the system's focal plane. We termed this plane as **"nominal in-focus plane"** (Fig. S11). Fortunately, in most of the biological samples, the nominal in-focus plane is approximately aligned with the geometric center of the sample along the axial direction. We composed the following part of this Note to prove this statement.

For a 3D sample, an axial shift (z') will introduce a wave propagation term $e^{jk_z z'}$ to its 3D spectrum. Here, we introduce the following Lemma (proved in Note 2.5):

Lemma 2.2.1. *Let $o(\mathbf{r}_\perp, z)$ be a 3D scattering potential and $\widehat{O}(\mathbf{k}_\perp, k_z)$ its 3D Fourier transform. Define a spatially shifted potential $o'(\mathbf{r}_\perp, z) = o(\mathbf{r}_\perp, z + z')$, with corresponding spectrum*

$$\widehat{O}'(\mathbf{k}_\perp, k_z; z') = \widehat{O}(\mathbf{k}_\perp, k_z) e^{jk_z z'}. \tag{S117}$$

Then the following equivalence holds:

$$\frac{\partial}{\partial k_z} \arg\left(\widehat{O}'(\mathbf{k}_\perp, k_z; z')\right)\Big|_{\mathbf{k}=0} = 0 \quad \Longleftrightarrow \quad z' = z_0 := \frac{\iiint z\, o(\mathbf{r}_\perp, z)\, d\mathbf{r}_\perp dz}{\iiint o(\mathbf{r}_\perp, z)\, d\mathbf{r}_\perp dz}.$$

Lemma 2.2.1 implies that $\arg\left(\widehat{O}'(\mathbf{k}_\perp, k_z; z' = z_0)\right)$ does not contain any linear term in k_z. In other words, $\widehat{O}'(\mathbf{k}_\perp, k_z; z_0)$ does not contain any wave-propagation term of the form $e^{jk_z C_0}$, where C_0 is a constant. By setting $z' = z_0$, we substitute the relation from Eq. (S117) into the object term in Eq. (S114),

$$\begin{aligned}\widehat{O}(\mathbf{k}_\perp - \mathbf{k}_{i\perp}, \sqrt{k_m^2 - |\mathbf{k}_\perp|^2} - k_{iz}) = \widehat{O}'(\mathbf{k}_\perp - \mathbf{k}_{i\perp}, \sqrt{k_m^2 - |\mathbf{k}_\perp|^2} - k_{iz}; z_0) \\ \times e^{-j\sqrt{k_m^2 - |\mathbf{k}_\perp|^2} z_0} \cdot e^{jk_{iz} z_0}.\end{aligned} \tag{S118}$$

Plugging Eq. (S118) into Eq. (S114), we have

$$\begin{aligned}\widehat{U}_\perp(\mathbf{k}_\perp; z_f) = (2\pi)^2 \delta(\mathbf{k}_\perp - \mathbf{k}_{i\perp}) e^{jk_{iz} z_f} \\ - \frac{j e^{jk_{iz} z_0}}{4\sqrt{k_m^2 - |\mathbf{k}_\perp|^2}} \widehat{O}'(\mathbf{k}_\perp - \mathbf{k}_{i\perp}, \sqrt{k_m^2 - |\mathbf{k}_\perp|^2} - k_{iz}; z_0) \\ \times e^{j\sqrt{k_m^2 - |\mathbf{k}_\perp|^2}(z_f - z_0)}.\end{aligned} \tag{S119}$$

If we align z_0 with the detection plane by setting $z_f = z_0$, we obtain:

$$\widehat{U}_\perp(\mathbf{k}_\perp; z_f = z_0) = C_1\, \delta(\mathbf{k}_\perp - \mathbf{k}_{i\perp}) + \frac{C_2}{\sqrt{k_m^2 - |\mathbf{k}_\perp|^2}} \widehat{O}'(\mathbf{k}_\perp - \mathbf{k}_{i\perp}, \sqrt{k_m^2 - |\mathbf{k}_\perp|^2} - k_{iz}). \tag{S120}$$

Here, C_1 and C_2 are constants. The scattered optical field (the second term in Eq. (S120)) no longer contains a wave-propagation term like $e^{j\sqrt{k_m^2 - |\mathbf{k}_\perp|^2} C_0}$. Therefore, at $z_f = z_0$ plane, the DAbI fringes have been perfectly compensated, that is to say, the focal plane is aligned with the nominal in-focus plane. This alignment indicates that the plane $z = z_0$ is the nominal in-focus plane, analogous to the in-focus plane in the 2D case. From Eq. (S118), z_0 is defined as the z-centroid of the scattering potential distribution. For most of the biological samples, this z-centroid is approximately aligned with the geometric central plane.

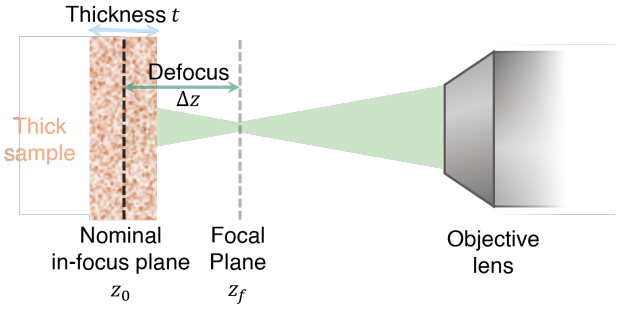

Figure S11: Graphical illustration of nominal in-focus plane z_0, focal plane z_f, defocus distance Δz, and sample thickness t.

2.3 Digital interference-like fringes for thick samples

Following a similar derivation from Eq. (S3) to Eq. (S15), the 3D counterpart of Eq. (S15) can be derived from Eq. (S120) with $z_f = z_0$:

$$\mathcal{F}\{I_1\} + \mathcal{F}\{I_2\} = C \cdot \frac{\widehat{O}'(\mathbf{k}_\perp, \sqrt{k_m^2 - |\mathbf{k}_\perp + \mathbf{k}_{1\perp}|^2} - k_{1z})}{\sqrt{k_m^2 - |\mathbf{k}_\perp + \mathbf{k}_{1\perp}|^2}} \cdot e^{j\widehat{\phi}(\mathbf{k}_\perp + \mathbf{k}_{1\perp})} + C \cdot \frac{\widehat{O}'(\mathbf{k}_\perp, \sqrt{k_m^2 - |\mathbf{k}_\perp + \mathbf{k}_{2\perp}|^2} - k_{1z})}{\sqrt{k_m^2 - |\mathbf{k}_\perp + \mathbf{k}_{2\perp}|^2}} \cdot e^{j\widehat{\phi}(\mathbf{k}_\perp + \mathbf{k}_{2\perp})}, \quad \mathbf{k}_\perp \in \mathcal{S}. \tag{S121}$$

Here, we have assumed $k_{1z} = k_{2z}$, since the two illumination angles are the same with respect to the optical axis. C is a constant, and $\mathcal{S}$ is defined in Eq. (S13).

For clarity, we define the terms

$$\text{Object term: } \frac{\widehat{O}'(\mathbf{k}_\perp, \sqrt{k_m^2 - |\mathbf{k}_\perp + \mathbf{k}_{i\perp}|^2} - k_{1z})}{\sqrt{k_m^2 - |\mathbf{k}_\perp + \mathbf{k}_{i\perp}|^2}}, \quad \text{Phase term: } e^{j\widehat{\phi}(\mathbf{k}_\perp + \mathbf{k}_{i\perp})}$$

Comparing Eq. (S15) and Eq. (S121), we observe that the 3D case differs significantly from the 2D case. In the 2D case, the object terms remain the same for both measurements within the region $\mathcal{S}$, while the aberrations at pupil phase are translated, producing clear interference fringes. In contrast, in 3D, the object terms differ in the two intensity spectra, except at:

$$\mathcal{S}_b \coloneqq \left\{ \mathbf{k}_\perp \in \mathcal{S} \,\middle|\, |\mathbf{k}_\perp + \mathbf{k}_{1\perp}|^2 = |\mathbf{k}_\perp + \mathbf{k}_{2\perp}|^2 \right\}. \tag{S122}$$

This defines a line in $\mathcal{S}$ along the angular bisection of $\mathbf{k}_{1\perp}$ and $\mathbf{k}_{2\perp}$—the 2D projection of the intersection curve between the two Ewald caps (Fig. S12). We define

$$\Delta k_z = \sqrt{k_m^2 - |\mathbf{k}_\perp + \mathbf{k}_{2\perp}|^2} - \sqrt{k_m^2 - |\mathbf{k}_\perp + \mathbf{k}_{1\perp}|^2}.$$

Then, Eq. (S121) can be rewritten as:

$$\mathcal{F}\{I_1\} + \mathcal{F}\{I_2\} = \frac{\widehat{O}'(\mathbf{k}_\perp, \sqrt{k_m^2 - |\mathbf{k}_\perp + \mathbf{k}_{1\perp}|^2} - k_{1z})}{\sqrt{k_m^2 - |\mathbf{k}_\perp + \mathbf{k}_{1\perp}|^2}} e^{j\widehat{\phi}(\mathbf{k}_\perp + \mathbf{k}_{1\perp})} + \frac{\widehat{O}'(\mathbf{k}_\perp, \sqrt{k_m^2 - |\mathbf{k}_\perp + \mathbf{k}_{1\perp}|^2} + \Delta k_z - k_{1z})}{\sqrt{k_m^2 - |\mathbf{k}_\perp + \mathbf{k}_{1\perp}|^2} + \Delta k_z} e^{j\widehat{\phi}(\mathbf{k}_\perp + \mathbf{k}_{2\perp})}, \quad \mathbf{k}_\perp \in \mathcal{S}. \tag{S123}$$

For $\mathbf{k}_\perp$ slightly deviating from $\mathcal{S}_b$, the resulting Δk_z is also relatively small. It can be shown that under the prior of a finite sample thickness (Note 2.4), the two terms,

$$\widehat{O}'(\mathbf{k}_\perp, \sqrt{k_m^2 - |\mathbf{k}_\perp + \mathbf{k}_{1\perp}|^2} - k_{1,z}) \text{ and } \widehat{O}'(\mathbf{k}_\perp, \sqrt{k_m^2 - |\mathbf{k}_\perp + \mathbf{k}_{1\perp}|^2} + \Delta k_z - k_{1,z}),$$

share the same $\mathbf{k}_\perp$ and a slightly different k_z in the sample spectrum, resulting in a slight difference between themselves. Although they are not strictly identical, these two spectra terms remain highly correlated. This correlation allows the two object terms to interfere in the presence of defocus aberrations and produces observable fringe patterns atop the background contributed by uncorrelated components.

As the distance between $\mathbf{k}_\perp$ and the line defined by $\mathcal{S}_b$ increases, the corresponding Δk_z increases due to the Ewald sphere geometry, which in turn degrades the correlation between $\widehat{O}'(\mathbf{k}_\perp, \sqrt{k_m^2 - |\mathbf{k}_\perp + \mathbf{k}_{1\perp}|^2} - k_{1,z})$ and $\widehat{O}'(\mathbf{k}_\perp, \sqrt{k_m^2 - |\mathbf{k}_\perp + \mathbf{k}_{1\perp}|^2} + \Delta k_z - k_{1,z})$. In the meantime, the difference between the two terms,

$$\frac{1}{\sqrt{k_m^2 - |\mathbf{k}_\perp + \mathbf{k}_{1\perp}|^2}} \text{ and } \frac{1}{\sqrt{k_m^2 - |\mathbf{k}_\perp + \mathbf{k}_{1\perp}|^2} + \Delta k_z},$$

also increases. As a result, the fringe contrast diminishes progressively and eventually becomes undetectable.

This phenomenon is similar to the concept of the partial coherence (Fig. S13). The interference of the partially coherent lights has a slow-varying fringe contrast modulation atop the cosine interference pattern. Then, Eq. (S16) in 2D case can be rewritten as,

$$|\mathcal{F}\{I_1\} + \mathcal{F}\{I_2\}| \propto \sqrt{2 + 2\cos\left(\widehat{\phi}(\mathbf{k}_\perp + \mathbf{k}_{1\perp}) - \widehat{\phi}(\mathbf{k}_\perp + \mathbf{k}_{2\perp})\right)\gamma(k_\perp)}, \quad \mathbf{k}_\perp \in \mathcal{S}. \tag{S124}$$

where $\gamma(k_\perp)$ is the envelope of the correlation factor, indicating the fringe contrast and degree of coherence.

To conclude, for a 3D thick sample, there exists an interference region surrounding the line $\mathcal{S}_b$ within $\mathcal{S}_\perp$, where interference fringes induced by defocus aberration are present. The fringe contrast gradually decreases away from the center of this region. Within the visible fringe regions, the fringe characteristics closely resemble those in the 2D case, enabling the application of existing 2D methods with only minor modifications, primarily guided by the reduction in fringe contrast and spatial coverage. The extent of the visible fringe region is influenced by the sample's thickness and refractive index distribution, and can thus serve as a qualitative indicator for estimating the sample thickness (Note 7).

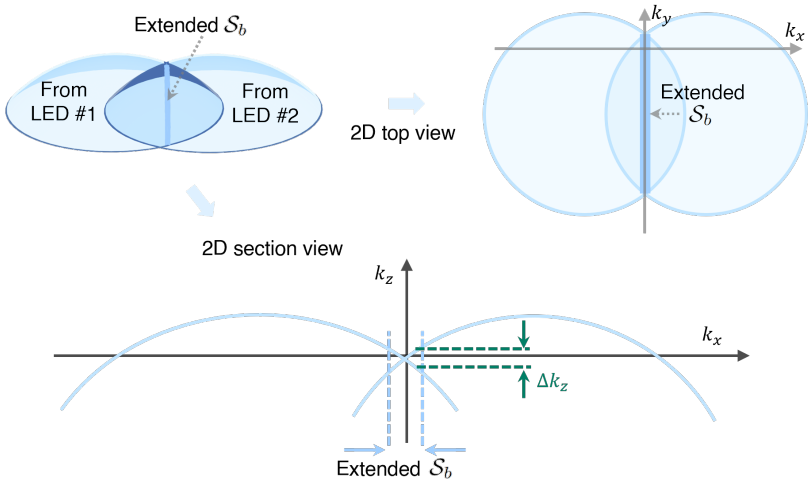

Figure S12: 3D coherent transfer function under two oblique angles. The overlap line of two spherical caps is defined in Eq. (S122) as $\mathcal{S}_b$. With the finite sample thickness prior. this region set $\mathcal{S}_b$ can be extended. Δkz in Eq. (S123) is also indicated in this figure.

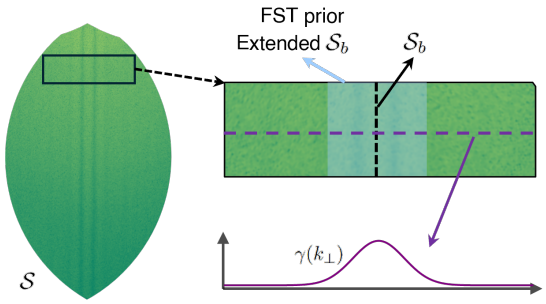

Figure S13: DAbI interference-like fringes for thick samples. The visibility of the fringes decreased, as it is far from the center line. The concept mimics the partial coherence in light behavior. $\gamma(k_\perp)$ in Eq. (S124) shows the fringe contrast, sharing a similar concept to the degree of coherence.

2.4 Mathematical note 1: finite sample thickness prior

The finite sample thickness (FST) prior, which was first proposed by [2], assumes that most sample content is confined within a finite axial range in the spatial domain. Based on our above analysis, we give an intuitive and descriptive explanation for this prior.

Here, we focus on the axial direction and show that

$$\widehat{O}'\left(\mathbf{k}_\perp, \sqrt{k_m^2 - |\mathbf{k}_\perp + \mathbf{k}_{1\perp}|^2} - k_{1,z}\right) \quad \text{and} \quad \widehat{O}'\left(\mathbf{k}_\perp, \sqrt{k_m^2 - |\mathbf{k}_\perp + \mathbf{k}_{1\perp}|^2} + \Delta k_z - k_{1,z}\right)$$

in Eq. (S123) are correlated when Δk_z is small, as a direct consequence of the FST prior.

Consider the axial object function $o^{\mathrm{Inf}}(z)$ of an ideal, infinitely thick sample, and its Fourier transform $\widehat{O}^{\mathrm{Inf}}(k_z)$. Because $o^{\mathrm{Inf}}(z)$ has unbounded support, $\widehat{O}^{\mathrm{Inf}}(k_z)$ is essentially unconstrained, meaning $\widehat{O}^{\mathrm{Inf}}(k_z + \Delta k_z)$ can differ significantly from $\widehat{O}^{\mathrm{Inf}}(k_z)$ even if Δk_z is small. In this case, $\widehat{O}^{\mathrm{Inf}}(k_z)$ and $\widehat{O}^{\mathrm{Inf}}(k_z + \Delta k_z)$ are uncorrelated and therefore cannot produce interference fringes under defocus aberration.

In physically realistic scenarios, the sample always has a finite axial extent t. Therefore, the finite thickness sample function $o^{\mathrm{Inf}}(z)$ can be modeled by the truncation of a rectangular window function $\mathrm{Rect}(z/t)$:

$$o(z) = o^{\mathrm{Inf}}(z) \cdot \mathrm{Rect}(z/t) \tag{S125}$$

Then, its Fourier transform becomes:

$$\widehat{O}(k_z) = \widehat{O}^{\mathrm{Inf}}(k_z) * [t \cdot \mathrm{sinc}(k_z t)] = t \int \widehat{O}^{\mathrm{Inf}}(k'_z)\, \mathrm{sinc}\left((k_z - k'_z)t\right)\, dk'_z \tag{S126}$$

Every point in $\widehat{O}^{\mathrm{Inf}}(k'_z)$ is convolved with the sinc function in Eq. (S126), and $\widehat{O}(k_z)$ is the resulting superposition of these expanded points. This convolution enforces spectral smoothness in the axial frequency domain.

When $|\Delta k_z| \leq \frac{2}{t}$, i.e., within the main lobe of the sinc function, both $\widehat{O}(k_z)$ and $\widehat{O}(k_z + \Delta k_z)$ share contributions from overlapping regions of $\widehat{O}^{\mathrm{Inf}}(k'_z)$, weighted by the sinc kernel. Therefore, they are correlated.

Consequently, for small Δk_z in Eq. (S123),

$$\widehat{O}'\left(\mathbf{k}_\perp, \sqrt{k_m^2 - |\mathbf{k}_\perp + \mathbf{k}_{1\perp}|^2} - k_{1z}\right) \quad \text{and} \quad \widehat{O}'\left(\mathbf{k}_\perp, \sqrt{k_m^2 - |\mathbf{k}_\perp + \mathbf{k}_{1\perp}|^2} + \Delta k_z - k_{1z}\right)$$

are correlated, providing the physical foundation for fringe formation in thick samples.

2.5 Mathematical note 2: proof of lemma 2.2.1

Lemma. *Let $o(\mathbf{r}_\perp, z)$ be a 3D scattering potential and $\widehat{O}(\mathbf{k}_\perp, k_z)$ its 3D Fourier transform. Define a spatially shifted potential $o'(\mathbf{r}_\perp, z) = o(\mathbf{r}_\perp, z + z')$, with corresponding spectrum*

$$\widehat{O}'(\mathbf{k}_\perp, k_z; z') = \widehat{O}(\mathbf{k}_\perp, k_z) e^{j k_z z'}. \tag{S127}$$

Then the following equivalence holds:

$$\frac{\partial}{\partial k_z} \arg\left(\widehat{O}'(\mathbf{k}_\perp, k_z; z')\right)\Big|_{\mathbf{k}=0} = 0 \quad \Longleftrightarrow \quad z' = z_0 := \frac{\iiint z\, o(\mathbf{r}_\perp, z)\, d\mathbf{r}_\perp dz}{\iiint o(\mathbf{r}_\perp, z)\, d\mathbf{r}_\perp dz}.$$

Proof

Assume that the spectrum can be expressed in polar form as

$$\widehat{O}(\mathbf{k}_\perp, k_z) = \left|\widehat{O}(\mathbf{k}_\perp, k_z)\right| e^{j\Omega(\mathbf{k}_\perp, k_z)},$$

where $\Omega(\mathbf{k}_\perp, k_z) := \arg\left(\widehat{O}(\mathbf{k}_\perp, k_z)\right)$. Then the derivative with respect to k_z becomes

$$\frac{\partial \widehat{O}(\mathbf{k}_\perp, k_z)}{\partial k_z} = \frac{\partial |\widehat{O}(\mathbf{k}_\perp, k_z)|}{\partial k_z} \cdot e^{j\Omega(\mathbf{k}_\perp, k_z)} + j\widehat{O}(\mathbf{k}_\perp, k_z) \cdot \frac{\partial \Omega(\mathbf{k}_\perp, k_z)}{\partial k_z}. \tag{S128}$$

Dividing both sides of Eq. (S128) by $\widehat{O}(\mathbf{k}_\perp, k_z)$, we obtain

$$\frac{1}{\widehat{O}(\mathbf{k}_\perp, k_z)} \cdot \frac{\partial \widehat{O}(\mathbf{k}_\perp, k_z)}{\partial k_z} = \frac{1}{|\widehat{O}(\mathbf{k}_\perp, k_z)|} \cdot \frac{\partial |\widehat{O}(\mathbf{k}_\perp, k_z)|}{\partial k_z} + j\frac{\partial \Omega(\mathbf{k}_\perp, k_z)}{\partial k_z}. \tag{S129}$$

Taking the imaginary part of both sides yields

$$\mathrm{Im}\left[\frac{1}{\widehat{O}(\mathbf{k}_\perp, k_z)} \cdot \frac{\partial \widehat{O}(\mathbf{k}_\perp, k_z)}{\partial k_z}\right] = \frac{\partial \Omega(\mathbf{k}_\perp, k_z)}{\partial k_z}. \tag{S130}$$

From the property of the Fourier transform, we have

$$\frac{\partial \widehat{O}(\mathbf{k}_\perp, k_z)}{\partial k_z} = -j\mathcal{F}_{3D}\left\{z\, o(\mathbf{r}_\perp, z)\right\}(\mathbf{k}), \tag{S131}$$

which at $\mathbf{k} = 0$ gives

$$\left.\frac{\partial \widehat{O}(\mathbf{k}_\perp, k_z)}{\partial k_z}\right|_{\mathbf{k}=0} = -j \iiint z\, o(\mathbf{r}_\perp, z)\, d\mathbf{r}_\perp dz, \tag{S132}$$

and

$$\left.\widehat{O}(\mathbf{k}_\perp, k_z)\right|_{\mathbf{k}=0} = \iiint o(\mathbf{r}_\perp, z)\, d\mathbf{r}_\perp dz. \tag{S133}$$

For weakly-absorbed samples, substituting Eqs. (S132) and (S133) into Eq. (S130), we obtain

$$\left.\frac{\partial \Omega(\mathbf{k}_\perp, k_z)}{\partial k_z}\right|_{\mathbf{k}=0} = \mathrm{Im}\left[\frac{-j\iiint z\, o(\mathbf{r}_\perp, z)\, d\mathbf{r}_\perp dz}{\iiint o(\mathbf{r}_\perp, z)\, d\mathbf{r}_\perp dz}\right] = -\frac{\iiint z\, o(\mathbf{r}_\perp, z)\, d\mathbf{r}_\perp dz}{\iiint o(\mathbf{r}_\perp, z)\, d\mathbf{r}_\perp dz} = -z_0. \tag{S134}$$

Now considering the shifted spectrum defined in Eq. (S127), its phase is given by,

$$\arg\left(\widehat{O}'(\mathbf{k}_\perp, k_z; z')\right) = \arg\left(\widehat{O}(\mathbf{k}_\perp, k_z)\right) + k_z z'; \tag{S135}$$

thus, its derivative at $\mathbf{k} = 0$ is

$$\left.\frac{\partial}{\partial k_z}\arg\left(\widehat{O}'(\mathbf{k}_\perp, k_z; z')\right)\right|_{\mathbf{k}=0} = \left.\frac{\partial \Omega(\mathbf{k}_\perp, k_z)}{\partial k_z}\right|_{\mathbf{k}=0} + z'. \tag{S136}$$

Substituting Eq. (S134) into Eq. (S136), we conclude:

$$\left.\frac{\partial}{\partial k_z}\arg\left(\widehat{O}'(\mathbf{k}_\perp, k_z; z')\right)\right|_{\mathbf{k}=0} = -z_0 + z'.$$

Therefore, the condition

$$\left.\frac{\partial}{\partial k_z}\arg\left(\widehat{O}'(\mathbf{k}_\perp, k_z; z')\right)\right|_{\mathbf{k}=0} = 0 \tag{S137}$$

holds if and only if

$$z' = z_0. \tag{S138}$$

This completes the proof.

3 Two-LED optical configuration design

The core idea of DAbI for estimating the defocus distance is to track the valley positions $\mathbf{k}_{v\perp}$ in the combined Fourier magnitude spectrum $|\mathcal{F}\{I_1\} + \mathcal{F}\{I_2\}|$, and compute Δz using Eq. (S22). The valley tracking must be confined to a "clear" region (Fig. S2), where the spectral content arises solely from $\widehat{O}(\mathbf{k}_\perp)\widehat{P}(\mathbf{k}_\perp + \mathbf{k}_{1\perp}) + \widehat{O}(\mathbf{k}_\perp)\widehat{P}(\mathbf{k}_\perp + \mathbf{k}_{2\perp})$. This region has been formally defined as $\mathcal{S}$ in Eq. (S13). For 3D case, this region is further reduced due to the partial mismatch in the object spectrum. As indicated by Eq. (S13), the choice of illumination wavenumbers $\mathbf{k}_{1\perp}$ and $\mathbf{k}_{2\perp}$ will influence the shape and size of the "clear" region, thereby affecting the accuracy of defocus estimation. Therefore, a careful design of the illumination angles is helpful.

3.1 Polar illumination angle design

The polar illumination angle is defined as the angle between the illumination wavevector and the optical axis of the system (Fig. S14**b**), $\beta_i = \arcsin(|\mathbf{k}_{i\perp}|/k_0)$. This angle should not exceed the maximum acceptance angle of the imaging system, which is determined by its numerical aperture (NA). Below, we provide practical guidelines for selecting an appropriate pair of polar illumination angles to ensure optimal performance.

Suppose the two LEDs have significantly different polar illumination angles. In that case, the resulting region $\mathcal{S}$ takes on an irregular shape (Fig. S14**d**), reducing its usable area and compromising the accuracy of defocus distance estimation. In the 3D case, it is crucial to set the polar illumination angles of the two LEDs equal, as any mismatch would severely distort the interference fringes. Therefore, to improve accuracy and maintain consistency across both 2D and 3D scenarios, we used and strongly recommend using two LEDs with the same polar illumination angle.

Even when the two LEDs share the same polar illumination angle relative to the optical axis, a small angle leads to substantial overlap between the regions $|\mathbf{k}_\perp + \mathbf{k}_{i\perp}| \leq k_0\text{NA}$ and $|\mathbf{k}_\perp - \mathbf{k}_{i\perp}| \leq k_0\text{NA}$, resulting in a limited region $\mathcal{S}$ (Fig. S14**f**) and reduced estimation accuracy. Increasing the polar illumination angle expands this valid region. Theoretically, when the polar illumination angle approaches the maximum acceptance angle of the imaging system, the entire region satisfying $|\mathbf{k}_\perp + \mathbf{k}_{i\perp}| \leq k_0\text{NA}$ becomes accessible, thereby allowing optimal utilization of the spectrum.

In practice, DAbI does not require a precise match of the polar illumination angle to the system NA, relaxing the strict optical alignment and calibration. The rule of thumb is to set the polar illumination angle in the range of $0.8 \times \text{NA} < \sin\beta_i < \text{NA}$ to achieve near-optimal performance.

3.2 Azimuthal illumination angle separation design

The two plane-wave illumination angles can be described by two wavevectors $\mathbf{k}_1, \mathbf{k}_2$, including both polar (tilt from the optical axis) and azimuthal (projection on the sample plane) illumination angles. In Note 3.1, we have discussed that the polar illumination angles β_i are desired to be identical ($\beta_1 = \beta_2 = \beta$), within certain range ($0.8 \times \text{NA} < \sin\beta_i < \text{NA}$). To fully determine the design of two illumination angles, we still need to identify the relation between $\mathbf{k}_{1\perp}$ and $\mathbf{k}_{2\perp}$.

Here, we define the azimuthal illumination angle separation between $\mathbf{k}_{1\perp}$ and $\mathbf{k}_{2\perp}$ is 2θ, which satisfies

$$\mathbf{k}_{1\perp} \cdot \mathbf{k}_{2\perp} = (\mathbf{k}_1 \sin\beta) \cdot (\mathbf{k}_2 \sin\beta) = |\mathbf{k}_1||\mathbf{k}_2| \sin^2\beta \cos 2\theta = k_0^2 \sin^2\beta \cos 2\theta, \quad \theta \in [0, \pi/2].$$

For a better visual understanding, we also demonstrate the azimuthal illumination angle θ in Fig. S14**b**.

Theoretically, as long as $0 < \theta < \pi/2$, the existence of the set $\mathcal{S}$ can be guaranteed. However, this existence cannot guarantee a high-performance defocus detection in DAbI. For example, the maximum defocus distance that can be detected is determined by the sampling rate at the camera plane, which is associated with system magnification, camera pixel pitch, illumination wavelength, FOV size, the system NA, and the size of set $\mathcal{S}$ (Details in Note 6). Most of the factors are system-dependent. Once the optical imaging system is set, we don't have much freedom to adjust. Only the size of the set $\mathcal{S}$ factor can be tuned by the azimuthal illumination angle separation θ.

Given a fixed set of system parameters, a smaller θ will result in a larger size of set $\mathcal{S}$ (Fig. S14**c,f**). However, if θ is too small ($\mathbf{k}_{1\perp}$ is very close to $\mathbf{k}_{2\perp}$), given a fixed defocus distance Δz and fixed system parameters, the valley positions $\mathbf{k}_{v\perp}$ will be very far from the central line of set $\mathcal{S}$ (Eq. (S22), further analysis in Note 6). This large value of $\mathbf{k}_{v\perp}$ will result in the disappearance of the fringes, which may pose difficulty in finding defocus directions and values. Therefore, the selection of θ should not be too small.

In this work, we generally used $2\theta \in [\pi/10, \pi/3]$. This is not a strict criterion and may be adjusted based on the application.

In summary, we recommend setting the angles within the following range; however, this is a guideline rather than a strict requirement.

- $2\theta \in [\pi/10, \pi/3]$
- $0.8 \times \mathrm{NA} < \sin\beta_i < \mathrm{NA}$

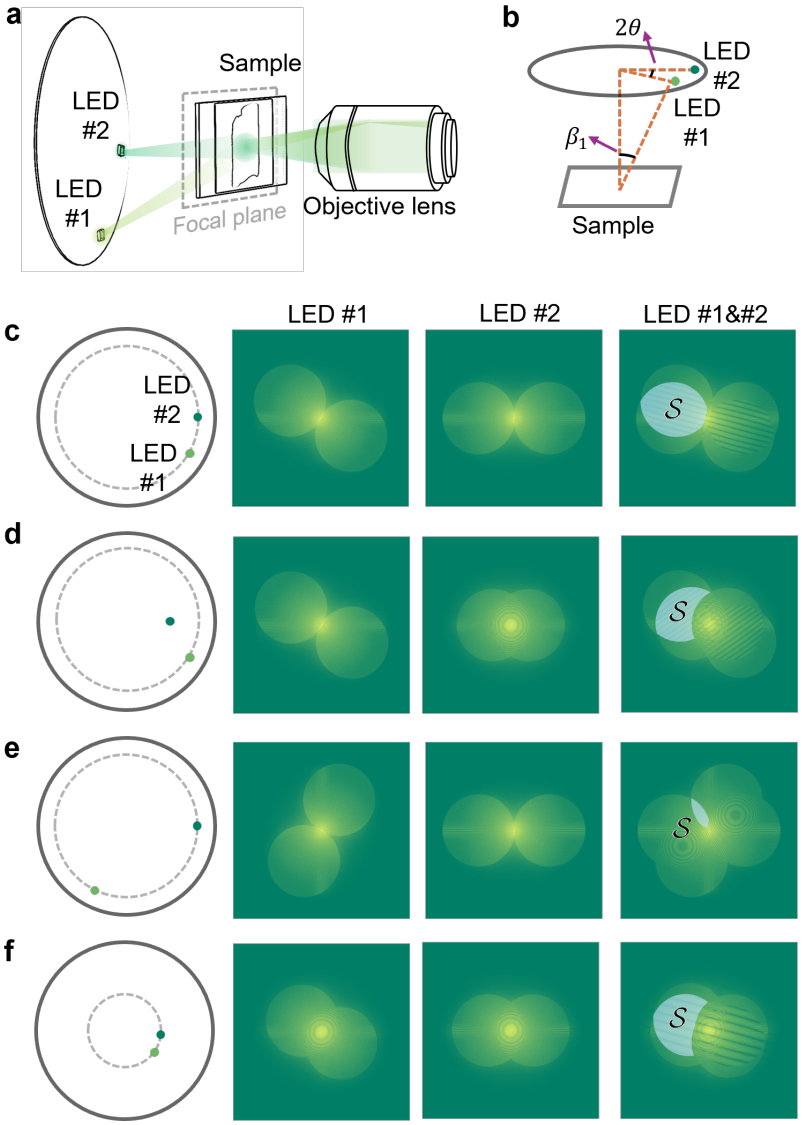

Figure S14: **a**, Two-LED configuration in the optical setup. **b**, Geometric definition of polar illumination angle β and the azimuthal illumination angle separation 2θ. **c**, A recommended two-LED configuration. A configuration with **d**, $\beta_1 \neq \beta_2$, **e**, $2\theta > \pi/2$, **f**, small β. Set $\mathcal{S}$ is the overlap region defined in Eq. (S13).

4 Algorithm for determining defocus distances

Tailored for our special illumination design, DAbI algorithm integrates the virtual defocus aberration strategy, the fringe curvature compensation strategy, and the fast Fourier transform (FFT) to accurately detect defocus from fringe patterns over small and large defocus ranges under versatile system settings. In this note, we present the detailed algorithmic design of DAbI and provide pseudocode. Following the discussion in Note 3, we assume throughout this section that the two LEDs have identical polar illumination angles ($\beta_1 = \beta_2 = \beta$) relative to the optical axis of the sample.

From DAbI's principle, a straightforward approach to estimate the defocus distance is to identify the valley positions $\mathbf{k}_v$ in $|\mathcal{F}\{I_1\} + \mathcal{F}\{I_2\}|$ and compute $|\Delta z|$ using Eq. (S22). However, this brute-force approach is not only computationally inefficient but also highly sensitive to experimental noise and outliers. In such a way, it is difficult to precisely localize the valley positions, leading to inaccurate defocus estimation. Instead of relying on this naïve strategy, we propose an efficient and robust defocus estimation algorithm.

We start with the 2D case based on Eq. (S21). Since the two illumination LEDs have identical polar illumination angles, without loss of generality, we define:

$$\mathbf{k}_{1\perp} = (k_c \cos\theta, -k_c \sin\theta), \quad \mathbf{k}_{2\perp} = (k_c \cos\theta, k_c \sin\theta)$$

where $k_c = k_0 \sin\beta$. Equation (S21) can then be rewritten as:

$$\left(\sqrt{k_0^2 - (k_x + k_c\cos\theta)^2 - (k_y - k_c\sin\theta)^2} - \sqrt{k_0^2 - (k_x + k_c\cos\theta)^2 - (k_y + k_c\sin\theta)^2}\right)\Delta z = n\pi, \quad \text{where} \quad n = 2m-1, \quad m \in \mathbb{Z}, \quad \mathbf{k}_v \in \mathcal{S}_\mathrm{v} \tag{S139}$$

The valid region $\mathcal{S}_\mathrm{v}$ in Fourier space is defined as:

$$\mathcal{S}_\mathrm{v} \coloneqq \left\{ \mathbf{k}_\perp \in \mathbb{R}^2 \;\middle|\; \begin{array}{l} (k_x + k_c\cos\theta)^2 + (k_y - k_c\sin\theta)^2 \le k_0^2\mathrm{NA}^2 \\ (k_x + k_c\cos\theta)^2 + (k_y + k_c\sin\theta)^2 \le k_0^2\mathrm{NA}^2 \\ (k_x - k_c\cos\theta)^2 + (k_y + k_c\sin\theta)^2 > k_0^2\mathrm{NA}^2 \\ (k_x - k_c\cos\theta)^2 + (k_y - k_c\sin\theta)^2 > k_0^2\mathrm{NA}^2 \end{array} \right\}. \tag{S140}$$

Let

$$A = \frac{(k_x + k_c\cos\theta)^2 + (k_y - k_c\sin\theta)^2}{k_0^2}, \quad B = \frac{(k_x + k_c\cos\theta)^2 + (k_y + k_c\sin\theta)^2}{k_0^2},$$

then Eq. (S139) can be expanded using Taylor series as:

$$(2\sin\beta\, k_y \sin\theta + R(A) + R(B))\,\Delta z = n\pi, \tag{S141}$$

where $R(A)$ and $R(B)$ denote the higher-order remaining terms resulting from the Taylor expansion, which become negligible when the NA is small.

When the system NA is small (e.g., NA < 0.3), A and B are small, and the higher-order terms are negligible. Equation (S141) becomes:

$$2\sin\beta\, k_y \sin\theta \Delta z = n\pi. \tag{S142}$$

Equation (S142) is a simplified version of Eq. (S26). The resulting fringes are straight lines parallel to the x-axis. Considering two adjacent fringes, we have:

$$|\Delta z| = \frac{\pi}{\Delta k_y \sin\beta \sin\theta}, \tag{S143}$$

where Δk_y is the spacing between two adjacent fringes, which can be estimated by applying a Fourier transform and searching for the frequency peaks.

Fringe Curvature Compensation Strategy. For higher system NA, the higher-order residual terms $R(A)$ and $R(B)$ introduce curvature to the fringes, making the estimated Δz inaccurate (Note 1.5). To correct for this, we digitally compensate for the fringe curvature by introducing virtual compensation terms into the spectra. Suppose we already have an initial estimation of the defocus distance from Eqs. (S32),(S34),(S143),

denoted as Δz_0. Based on this estimation, within the set $\mathcal{S}$, rather than directly summing the contributions from two measurements (as in Eqs. (S14),(S15)), we first add the individual residual terms to each part separately. This yields:

$$\mathcal{F}\{I_i\}_{\mathrm{Vir}} = \widehat{A}(\mathbf{k}_\perp)\, e^{j\widehat{\eta}(\mathbf{k}_\perp)}\, e^{j\sqrt{k_0^2-|\mathbf{k}_\perp+\mathbf{k}_{i\perp}|^2}\Delta z}\, e^{j\left(\sqrt{k_0^2-|\mathbf{k}_\perp+\mathbf{k}_{i\perp}|^2}-\frac{|\mathbf{k}_\perp+\mathbf{k}_{i\perp}|^2}{2k_0}\right)\Delta z_0}, \quad i=1,2,\ \mathbf{k}_\perp\in\mathcal{S}_{\mathrm{v}}. \tag{S144}$$

Note that

$$\sqrt{k_0^2-|\mathbf{k}_\perp+\mathbf{k}_{i\perp}|^2}-\frac{|\mathbf{k}_\perp+\mathbf{k}_{i\perp}|^2}{2k_0}\approx k_0+R(\cdot).$$

Then, summing these two terms and taking the absolute value yields observable fringes. The modified fringe condition becomes:

$$2\sin\beta\, k_y \sin\theta\Delta z + (R(A)+R(B))(\Delta z-\Delta z_0) = n\pi. \tag{S145}$$

Given that Δz_0 is a reasonably good initial estimation of Δz, the residual terms partially compensate for the high-order effects that cause curvature, resulting in straighter fringes. We can then recalculate the defocus distance Δz_1 using the same Fourier transform-based method. If Δz_1 is not sufficiently accurate, the procedure can be repeated to obtain $\Delta z_2, \Delta z_3, \ldots$, until the series converges to a stable and precise solution.

This iterative method is inspired by the Born series approach commonly used in solving scattering problems. For systems with small to moderate NA (e.g., NA < 0.3), a single iteration is often sufficient to produce accurate results. For high-NA systems (e.g., NA > 0.3), our simulations show that 3–5 iterations typically yield precise estimations.

Virtual Defocus Aberration Strategy. To tackle small defocus detection and the sign ambiguity challenges, we incorporate the virtual defocus aberration strategy introduced in Note 1.6.

When the defocus is relatively small, the fringes are either not dense enough for accurate quantification. In such cases, we virtually introduced a known large defocus aberration to set $\mathcal{S}$ to generate denser and more distinguishable fringe patterns. We then summed the two modified spectra and applied the Fourier transform to extract the fringe frequency and calculate the total defocus distance. By subtracting the known virtual defocus, we obtained both the actual defocus distance and the defocus direction Note 1.6. For example, we first virtually add an 80-µm defocus aberration and a 74-µm defocus distance is calculated by the Fourier transform method. The physical defocus distance solved by DAbI is 74 µm − 80 µm = −6 µm, which naturally incorporates both the absolute distance and the direction of defocus.

In the case of large defocus distances, the frequency of the fringe patterns and defocus distance can be directly obtained from the Fourier transform of the fringe pattern together with the fringe curvature compensation strategy. However, the sign of the defocus remains ambiguous. To resolve this, we applied the virtual defocus aberration strategy by introducing an adaptive known defocus aberration in both positive and negative directions. These additions alter the fringe density in the resulting interference patterns. The direction that yields denser fringes indicates the correct sign of the original defocus.

For 3D samples, as discussed in Note 2, the fringe patterns exhibit similar spatial structures to the 2D case, but their contrast gradually diminishes away from the center. Therefore, an adaptive fringe region selection method is designed, which automatically selects a region of interest based on the spectrum's signal-to-noise ratio (SNR) and local fringe contrast. This selected region is then processed with our algorithm.

In summary, by integrating these specially designed components, our proposed DAbI algorithm is capable of robustly and precisely estimating both the magnitude and direction of defocus for both 2D and 3D samples across a wide range of system configurations. Detailed pseudocode is described in Algorithm 1. The simulation and experiment code can be found on GitHub (https://github.com/hwzhou2020/DAbI).

DAbI Algorithm Pseudocode

Algorithm 1 DAbI Defocus Estimation Algorithm

Require: Intensity measurements I_1, I_2; illumination wave vectors $\mathbf{k}_1, \mathbf{k}_2$; free-space wavenumber k_0; numerical aperture NA; maximum iteration count N; adaptive known defocus z_v

Ensure: Estimated defocus distance Δz

Compute Fourier transforms: $F_1 \leftarrow \mathcal{F}\{I_1\}$, $F_2 \leftarrow \mathcal{F}\{I_2\}$
if NA < 0.3 **then**
    Set $N \leftarrow 1$
end if
Define valid spectral region $\mathcal{S}$ based on Eq. (S13)
Select subregion $\mathcal{S}_{\text{sub}} \subset \mathcal{S}$ based on signal-to-noise ratio and local fringe contrast
Estimate defocus level (small or large) using FFT within $\mathcal{S}_{\text{sub}}$
if Defocus level is large **then**
    Set $z_v \leftarrow 0$
end if
Apply virtual defocus aberration (Note 1.6): add z_v to F_1, F_2 within $\mathcal{S}_{\text{sub}}$
Compute combined spectrum: $F_{\text{sum}} \leftarrow |F_1 + F_2|$
Estimate fringe spacing Δk_y from the fringe pattern via FFT
Estimate $|\Delta z + z_v|$ using Eq. (S143)
Determine defocus direction using virtual defocus aberration in $\mathcal{S}_{\text{sub}}$
for $i = 1$ to N **do**
    Apply virtual compensation to $F_1, F_2 \rightarrow F_1', F_2'$ using Eq. (S144) and $\Delta z + z_v$
    Update combined spectrum: $F'_{\text{sum}} \leftarrow F_1', F_2'$
    Estimate updated fringe spacing Δk_y
    Update defocus estimate $\Delta z + z_v$ using Eq. (S143)
    if Converged **then**
        break
    end if
end for
return Δz

5 Illumination angle and system calibration

To perform DAbI using our demonstrated illumination angle choices (discussed in Note 3), a one-time calibration is required to determine the illumination angles generated by the LEDs or lasers.

We first place a thin 2D biological sample at the focal plane of the imaging system. Natural biological samples with rich spatial-frequency content are preferred to facilitate reliable alignment. In our experiments, a human lung cancer pathology slide was used for calibration. An LED array (or two individual LEDs) mounted on a three-axis translation stage is then adjusted to control the illumination positions.

Next, two intensity images (I_1, I_2) are acquired under the two illumination angles, respectively. Taking the Fourier transform of each intensity image reveals a characteristic two-circle pattern in the amplitude spectrum (Fig. S15). The centers of the circular regions directly correspond to the illumination angles and are given by

$$\begin{aligned}
\Delta k_{x_i}^{\text{pixel}} &= \left\lfloor \frac{\Delta k_{x_i}}{\Delta\omega} \right\rfloor,\ \Delta k_{y_i}^{\text{pixel}} = \left\lfloor \frac{\Delta k_{y_i}}{\Delta\omega} \right\rfloor, \\
\Delta k_{x_i} &= \frac{2\pi}{\lambda} \frac{\Delta x_i}{\sqrt{\Delta x_i^2 + \Delta y_i^2 + \Delta h^2}},\ \Delta k_{y_i} = \frac{2\pi}{\lambda} \frac{\Delta y_i}{\sqrt{\Delta x_i^2 + \Delta y_i^2 + \Delta h^2}}, \\
\Delta\omega &= \frac{2\pi}{N_{\text{FOV}} \frac{e}{M}},
\end{aligned} \tag{S146}$$

where $(\Delta k_{x_i}^{\text{pixel}}, \Delta k_{y_i}^{\text{pixel}})$ denote the pixel coordinates of the circular region centers in the Fourier domain; $(\Delta k_{x_i}, \Delta k_{y_i})$ are the corresponding spatial frequencies in k-space; $\Delta\omega$ is the spatial-frequency sampling interval per pixel; λ is the central wavelength of the illumination source; $(\Delta x_i, \Delta y_i)$ are the lateral coordinates of the i-th LED relative to the optical axis; Δh is the distance between the LED plane and the sample plane; N_{FOV} is the number of pixels across the FOV; e is the camera pixel pitch; M is the system magnification; and $i = 1, 2$ denotes the two illumination conditions.

Given the analytic relation between the lateral shifts of the circular regions and the LED positions, the system can be calibrated using these two intensity images as feedback. Because the illumination angles are pre-designed according to Note 3, the target values of $(\Delta k_{x_i}^{\text{pixel}}, \Delta k_{y_i}^{\text{pixel}})$ and the corresponding LED positions are fixed. We therefore define the desired spectral locations of the circular regions, indicated by the black dashed circles in Fig. S15. By iteratively adjusting the LED positions, the measured spectral circles are aligned with these predefined locations. Once this condition is met, the system is considered well aligned. The illumination angle is given by

$$\begin{aligned}
\Delta\theta_{x_i} &= \arcsin \frac{\Delta x_i}{\sqrt{\Delta x_i^2 + \Delta y_i^2 + \Delta h^2}}, \\
\Delta\theta_{y_i} &= \arcsin \frac{\Delta y_i}{\sqrt{\Delta x_i^2 + \Delta y_i^2 + \Delta h^2}}.
\end{aligned} \tag{S147}$$

The azimuthal angle θ, and polar angle β in Note 3 can be expressed as:

$$\begin{aligned}
\cos 2\theta &= \frac{\Delta x_1^2 + \Delta y_1^2 + \Delta x_2^2 + \Delta y_2^2 - (\Delta x_1 - \Delta x_2)^2 - (\Delta y_1 - \Delta y_2)^2}{2\sqrt{\Delta x_1^2 + \Delta y_1^2}\sqrt{\Delta x_2^2 + \Delta y_2^2}}, \\
&= \frac{\Delta x_1 \Delta x_2 + \Delta y_1 \Delta y_2}{\sqrt{\Delta x_1^2 + \Delta y_1^2}\sqrt{\Delta x_2^2 + \Delta y_2^2}}, \\
\tan\beta &= \frac{\sqrt{\Delta x_1^2 + \Delta y_1^2}}{\Delta h}
\end{aligned} \tag{S148}$$

If the above calibration procedure does not provide sufficient accuracy, a sample-based calibration strategy for DAbI is recommended. In this approach, two to three representative samples are selected. For each sample, a z-scan is performed from the in-focus position over a user-defined axial range, sampled at 5–10 evenly spaced axial positions. The DAbI algorithm is then applied to estimate the defocus distance, which is compared against the nominal ground truth.

For commercial imaging systems, where the NA and magnification are fixed, calibration can be further refined by slightly adjusting the illumination angles of the two LEDs until the estimated defocus distances match the ground truth. In customized systems, variations in system NA and magnification can also be explicitly incorporated into the calibration procedure.

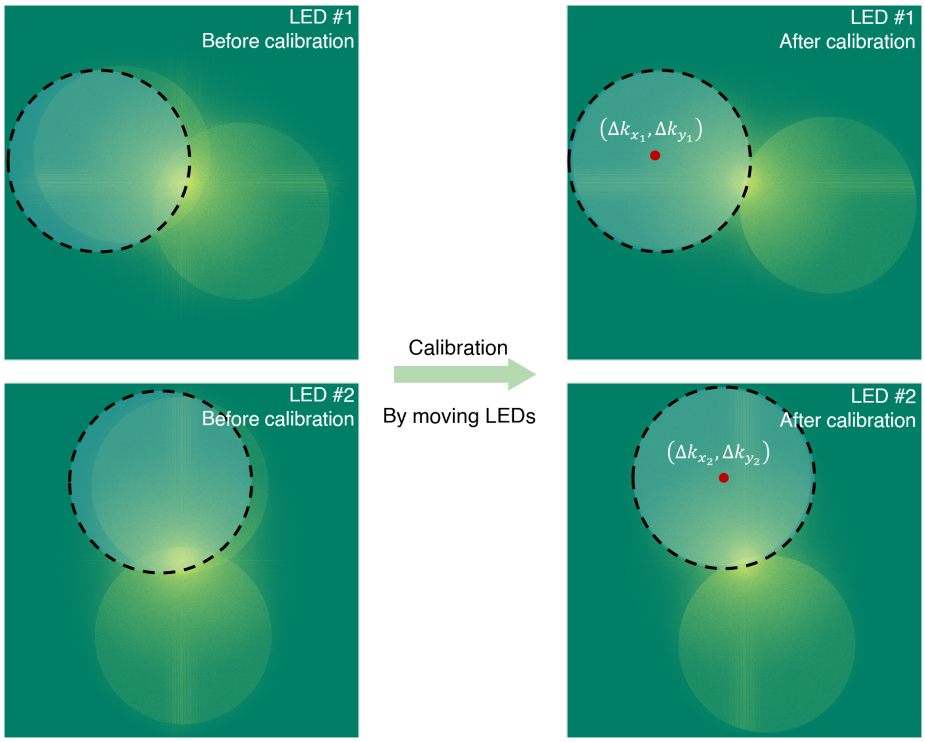

Figure S15: Visualization of the illumination angle calibration process from the intensity spectrum perspective. The black dashed circles mark the desired spectral region under the designed illumination angles.

6 Effect of different factors in DAbI autofocusing

In this section, we investigate how different system parameters affect the characteristics of DAbI fringes. Because the 3D case can be viewed as a narrowed visibility region of the corresponding 2D case, we focus here on 2D autofocusing using DAbI. The conclusions drawn in this section can be readily generalized to thick samples.

6.1 Effect of defocus distances

First, we revisit Eq. (S22) in Note 1.4,

$$|\Delta z| = \left| \frac{n\pi}{\sqrt{k_0^2 - |\mathbf{k}_{v\perp} + \mathbf{k}_{1\perp}|^2} - \sqrt{k_0^2 - |\mathbf{k}_{v\perp} + \mathbf{k}_{2\perp}|^2}} \right|.$$

For a given system configuration, the transverse illumination wavevectors $\mathbf{k}i \perp$ and the wavenumber k_0 are fixed. As the defocus distance $|\Delta z|$ increases, the corresponding valley positions $\mathbf{k}v \perp$ (at the same order) move toward smaller spatial frequencies, resulting in denser fringes in the Fourier domain. Conversely, when $|\Delta z|$ is sufficiently small, the solutions for the valley positions shift to large spatial frequencies. In this regime, the valleys fall outside the overlap region defined by the set $\mathcal{S}$, leading to the disappearance of observable fringes.

Figure S16 illustrates the DAbI fringes obtained from a thin sample at different defocus distances (wavelength $\lambda = 635, \mathrm{nm}$, NA $= 0.40$, magnification $20\times$, and camera pixel pitch 6.5 µm). A clear correlation between fringe density and defocus distance can be observed. For small defocus distances, where fringes are absent, we employ the virtual defocus aberration strategy to determine both the magnitude and the direction of defocus (Note 1.6).

6.2 Effect of numerical aperture, magnification, and pixel pitch

The NA and magnification of the objective lens, together with the camera pixel pitch, constitute three fundamental parameters of an imaging system. These parameters jointly affect the geometry of DAbI fringes and the performance of defocus detection.

To elucidate their impact on DAbI fringes, we simulated six representative combinations of NA, magnification, and camera pixel pitch, as shown in Fig. S17. The size and location of the DAbI fringe region $\mathcal{S}$ (defined in Eq. (S13)) depend on the system configuration. For low-NA systems (NA < 0.3), the fringes are predominantly straight, whereas pronounced curvature emerges at higher NA (NA > 0.3). This transition necessitates distinct algorithmic treatments, as described in Note 4. In particular, an iterative search strategy is employed to accurately handle high-NA regimes (Algorithm 1).

These parameters also govern the achievable autofocusing range and accuracy of DAbI by determining the number of sampled pixels and the effective sampling density within the fringe region $\mathcal{S}$. In the numerical realization of identifying the DAbI fringe spacing, the sampling rate of the fringes in the spectrum sets an upper bound on the maximum detectable defocus distance. Accordingly, Eq. (S143) can be rewritten in a discrete form as

$$|\Delta z| = \frac{N_{\mathrm{FOV}} e/M}{2N^{\#} \sin\beta \sin\theta}, \tag{S149}$$

where N_{FOV} denotes the number of pixels in the FOV; e stands for the camera pixel pitch; M denotes system magnification; and $N^{\#}$ is the pixel count for the fringe period. Noted that $N_{\mathrm{FOV}} e/M$ represents the physical size of the FOV.

According to the Nyquist sampling theorem [5], the sampling rate must satisfy at least two pixels for each period ($N^{\#} \geq 2$). When $N^{\#} = 2$, Eq. (S149) sets an upper limit for $|\Delta z|$:

$$|\Delta z| \leq \frac{N_{\mathrm{FOV}} e/M}{4 \sin\beta \sin\theta}, \tag{S150}$$

Equation (S150) shows that the theoretical range of DAbI depends directly on the camera pixel pitch and the magnification. Furthermore, in the recommended DAbI setup, the polar illumination angle (defined

in Note. 3.1) is close to the system's maximum acceptance angle, such that $\sin\beta \approx \mathrm{NA}$. As a result, the range is approximately inversely proportional to the system NA. Moreover, increasing the number of pixels within a single FOV and decreasing the azimuthal angle separation between the two LEDs both increase the achievable range, but come at the cost of reduced precision, especially at small defocus distances.

As an example, for $N_{\mathrm{FOV}} = 1536$, $e = 6.5$ μm, $M = 20$, $\sin\beta = 0.39$, and $\theta = \pi/8$, the resulting range is $|\Delta z| = 836$ μm.

We further experimentally evaluated the performance of DAbI under different NA and magnification configurations (Fig. S18), including 20×/0.40NA and 40×/0.65NA objective lenses. We did not test more extreme cases, such as 10×/0.25NA or lower magnification/NA settings, because the maximum achievable autofocusing range in those configurations exceeds the mechanical travel range of our experimental setup.

In terms of autofocusing range, DAbI maintains robust performance (one-sided) up to approximately 900 µm for the 20×/0.40NA system and 270 µm for the 40×/0.65NA system, which corresponds to 443× and 365× of the DoF. The corresponding theoretical upper limits for these two cases are 2132 µm and 656 µm, respectively. Thus, DAbI experimentally achieves about 40% of the theoretical upper limit in both cases, primarily due to non-negligible camera noises at extremely large defocus distances. Empirically, in the presence of noise, reliable DAbI operation typically requires 4–5 pixels per fringe period, which corresponds to approximately 40%–50% of the theoretical maximum range.

Regarding accuracy, Fig. S18a shows that DAbI retains high precision throughout the system DoF within the autofocusing range. As the system NA increases, the DoF decreases, and the accuracy requirement for autofocusing becomes increasingly stringent. Despite this challenge, DAbI consistently achieves large-defocus detection with satisfactory accuracy under high-NA conditions (Fig. S18b). We note the presence of one or two outliers in defocus estimation (Fig. S18), which we attribute to noise-induced fringe degradation at large defocus.

6.3 Effect of wavelengths

Defocus aberration is directly related to the defocus distance at a given wavelength, as manifested by the accumulated phase at the pupil plane of the imaging system. At the same time, a shorter wavelength corresponds to a larger wavenumber k_0, which leads to a broader coverage in spatial frequency space. As shown in Fig. S19, given a magnification of 20× and a camera pixel pitch of 4.5 µm, shorter wavelengths result in a more extensive coverage of the digitized pupil plane. However, the combined effects of phase accumulation and frequency coverage lead to the same fringe density in DAbI under different illumination wavelengths.

DAbI explicitly models wavelength dependence in fringe formation. As a result, it operates robustly across different optical wavelengths and can also accommodate system chromatic aberrations (Note 13.2). The effect of temporal partial coherence associated with different wavelengths has been further investigated through both theoretical analysis and numerical simulations in Note 1.7.

6.4 Effect of other aberrations

In practical optical systems, the defocus aberration may not be the sole aberration in the system. Common aberrations, such as spherical aberration, coma, and astigmatism, may exist and distort DAbI fringe patterns. In some of our experiments, we do observe the existence of spherical aberration. If the aberration level is small, this aberration can be negligible; otherwise, a precalibration procedure is needed.

In this simulation, we studied the cases of spherical aberration and complex aberrations. We set the defocus distance Δz to 50 µm and manually introduced aberrations of different types and magnitudes. We then applied DAbI to estimate the defocus distance. As shown in Fig. S20, the presence of other aberrations causes the DAbI fringes to become tilted, curved, or distorted.

In the left and middle columns, where other aberrations are relatively small, DAbI is still able to provide accurate defocus distance estimations (the defocus distance error is within the system DoF). In contrast, the right column shows cases with stronger aberrations, where the fringes are severely distorted and the defocus estimation by DAbI becomes unreliable. In such cases, it is necessary to perform a precalibration and digitally compensate for other aberrations.

We further note that the distribution of valley positions is directly coupled to all components of the system aberrations through a physical imaging model, providing a novel and intuitive approach for estimating

all system aberrations (not limited to defocus alone). By tracking the positions of these valleys, one can formulate and solve an inverse problem to recover the Zernike coefficients corresponding to different aberration modes. Deep learning–based approaches may be particularly well suited for this task, offering both accuracy and scalability.

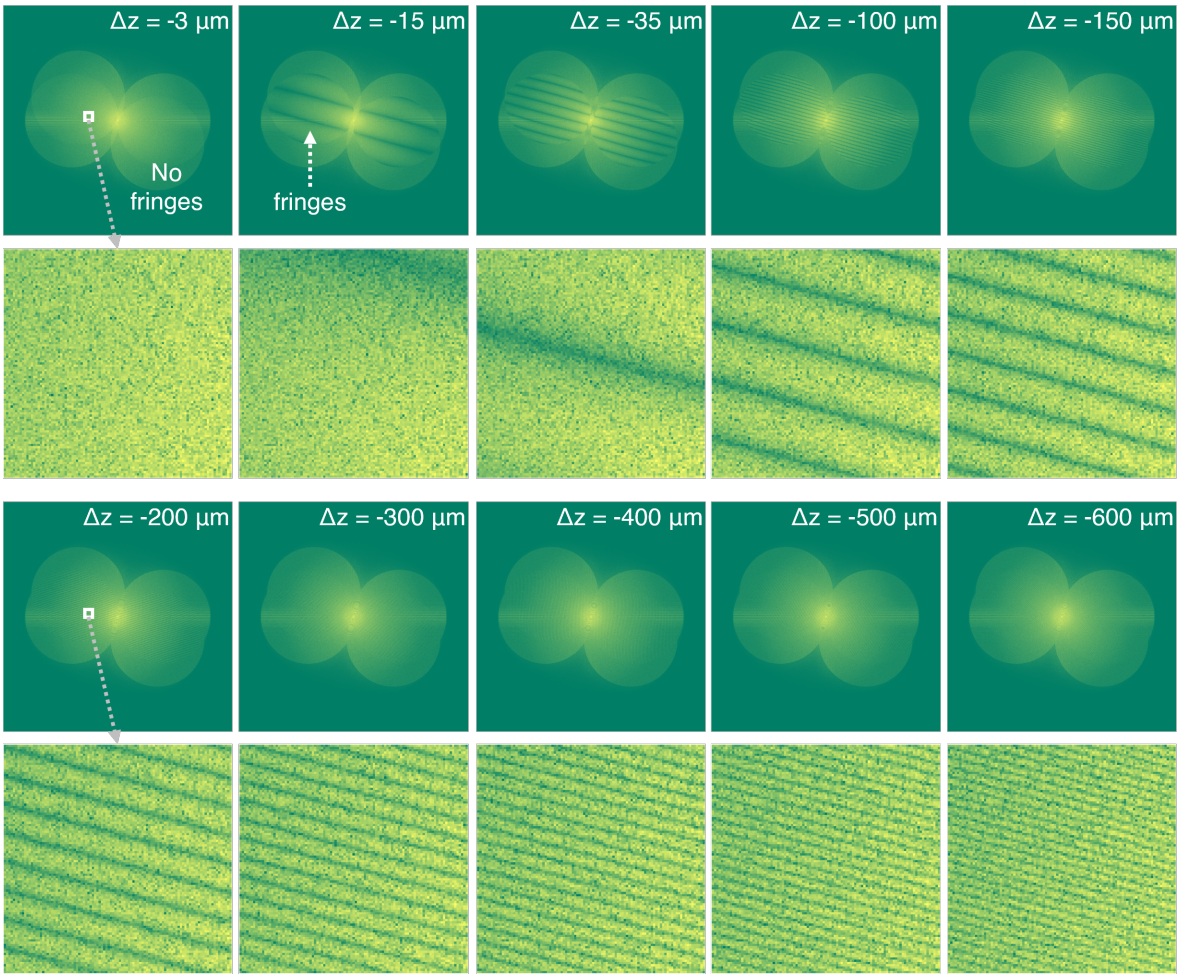

Figure S16: Effect of defocus distance on the DAbI fringe density. The second and fourth rows are zoomed-in regions in the white-box region in the first and third rows, respectively. Δz denotes the defocus distance.

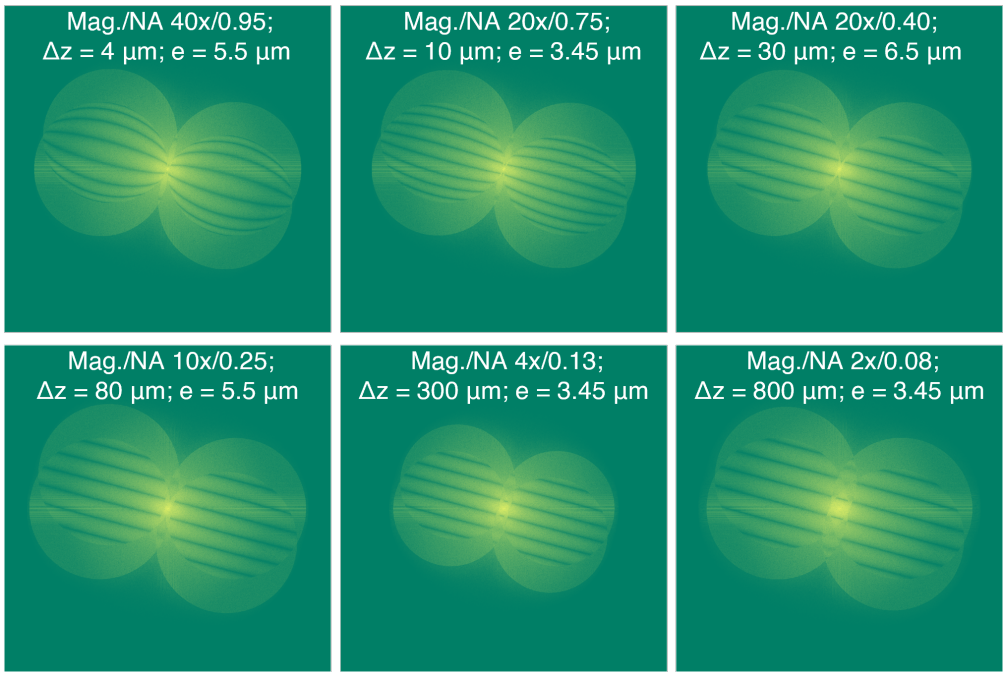

Figure S17: Effect of NA and magnification (mag.) on the DAbI fringes. The wavelength is set to 635 nm.

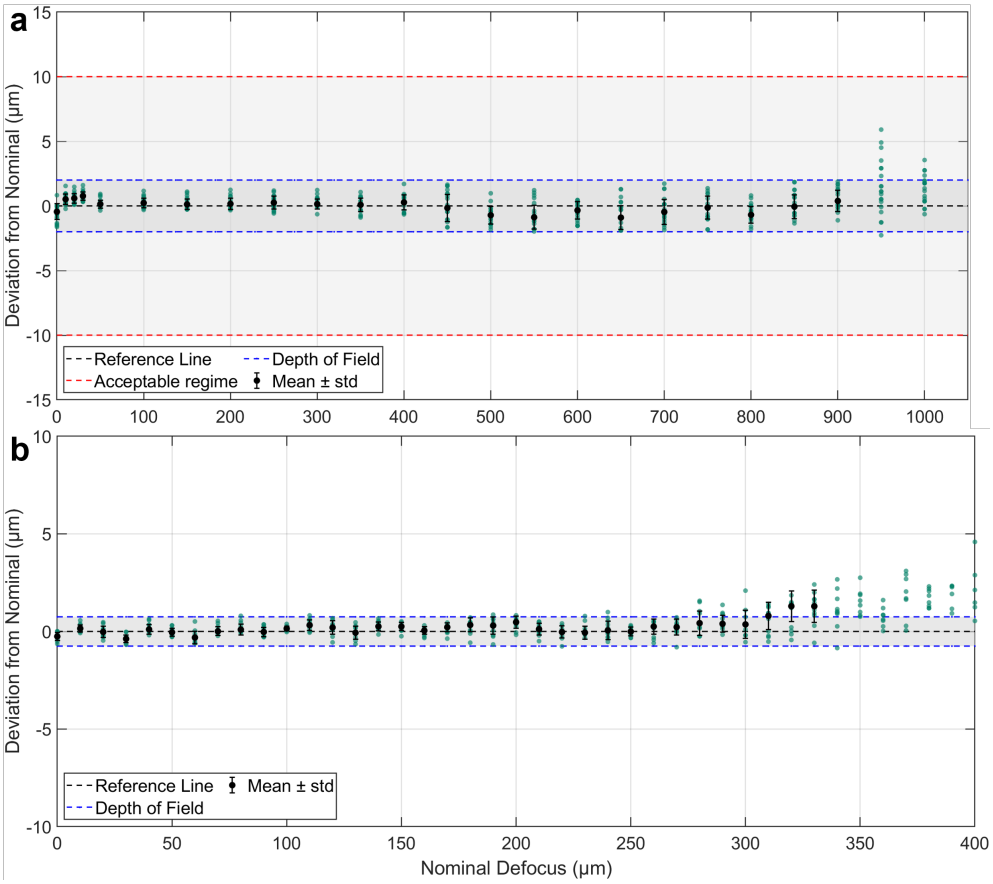

Figure S18: Experiment results of DAbI performance on two different NA/magnification settings with **a** 20 samples ($n = 20$) and **b** 10 samples ($n = 10$), **a**, 20×/0.4NA, **b**, 40×/0.65NA, with the same camera pixel pitch of 6.5 µm

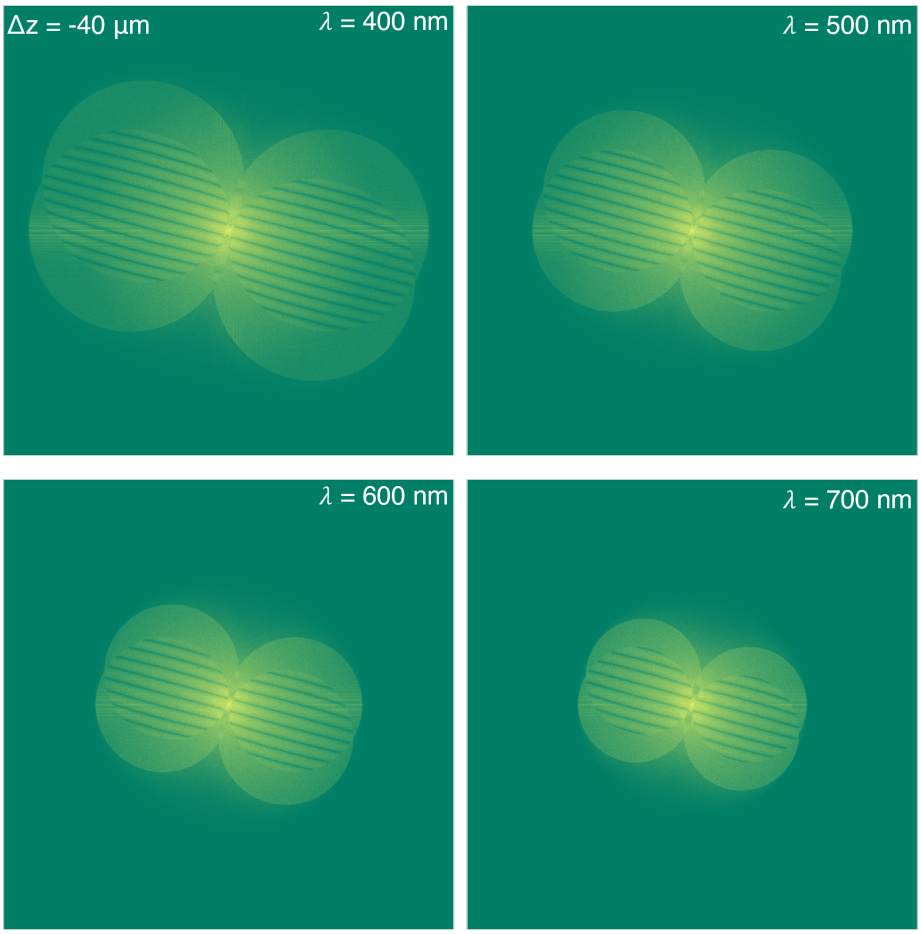

Figure S19: Effect of wavelength on the DAbI fringe density. The defocus distance Δz is set to 40 μm.

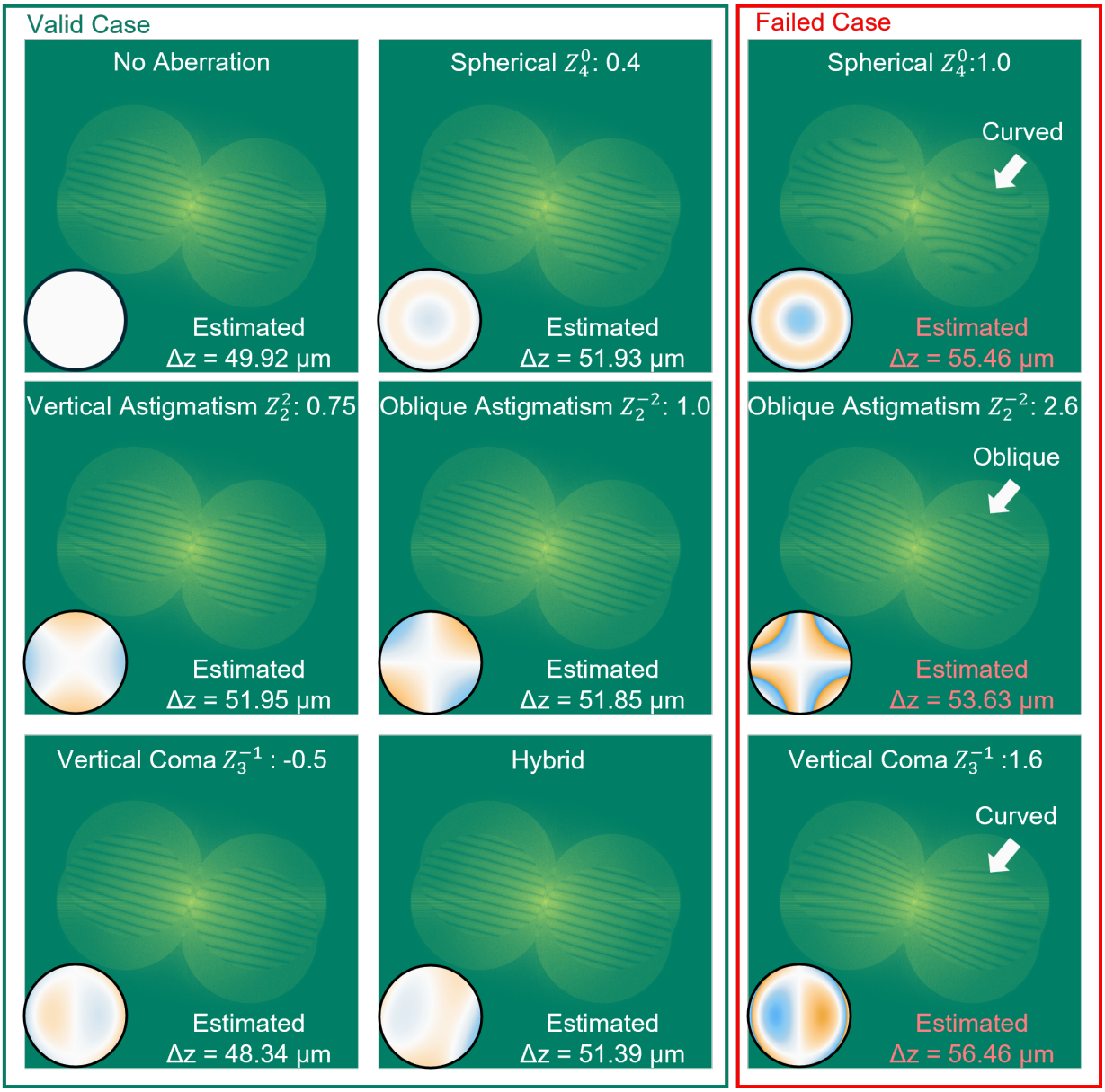

Figure S20: Effect of aberration on the DAbI fringes. The defocus distance Δz is set to 50 μm.

7 Sample thickness estimation

In Note 2, we discussed the relationship between fringe visibility and sample thickness. Specifically, an increase in sample thickness leads to a narrowing of the fringe visibility region within the set $\mathcal{S}$. Leveraging this relationship, sample thickness can be inversely inferred from the observed DAbI fringe regions.

In many practical scenarios, a rough estimate of sample thickness is already available. However, there remain cases in which the sample thickness is unknown. One such example is bacteria growing on agar substrates, where the sample gradually thickens over time, starting as a thin film and growing layer by layer [6]. In this context, DAbI has potential applications in quantifying sample growth dynamics.

Here, we demonstrate the qualitative relationship between sample thickness and fringe visibility using simulations (Fig. S21). A phase imaging video of label-free (unstained) live cells was used as the simulation input to mimic a volumetric biological sample [7]. Example ground-truth image planes of the simulated volume are shown in Fig. S21**a**–**d**. The background medium was assigned a refractive index of 1.33.

In Fig. S21**e**–**h**, we varied the simulated sample thickness while keeping the refractive index variation range fixed. As the sample thickness increased, the visible fringe region became progressively narrower. In addition, the fringe contrast exhibited a slight degradation.

This thickness–fringe visibility relationship is also influenced by the scattering characteristics of the sample and is therefore sample-dependent. As shown in Fig. S21**i**–**l**, we gradually increased the variation range of the refractive index distribution. A larger refractive index range Δn corresponds to stronger scattering. We observed that increased scattering led to a general degradation of fringe contrast. The underlying reason is that strong scattering significantly reduces the unscattered signal, resulting in a dominant auto-correlation term and a weakened second term in Eq. (S12). This effect also defines the operating regime of DAbI, which is not suitable for strongly scattering samples. In principle, this limitation may be mitigated through optical clearing techniques.

Due to the coupled effects of sample thickness and scattering characteristics, the visibility region and contrast of DAbI fringes cannot, in general, uniquely quantify sample thickness. Nevertheless, when certain sample priors are available—such as sample type or approximate refractive index distributions—DAbI still holds potential for applications in biological and clinical imaging. Further investigation along these directions will be pursued in future work.

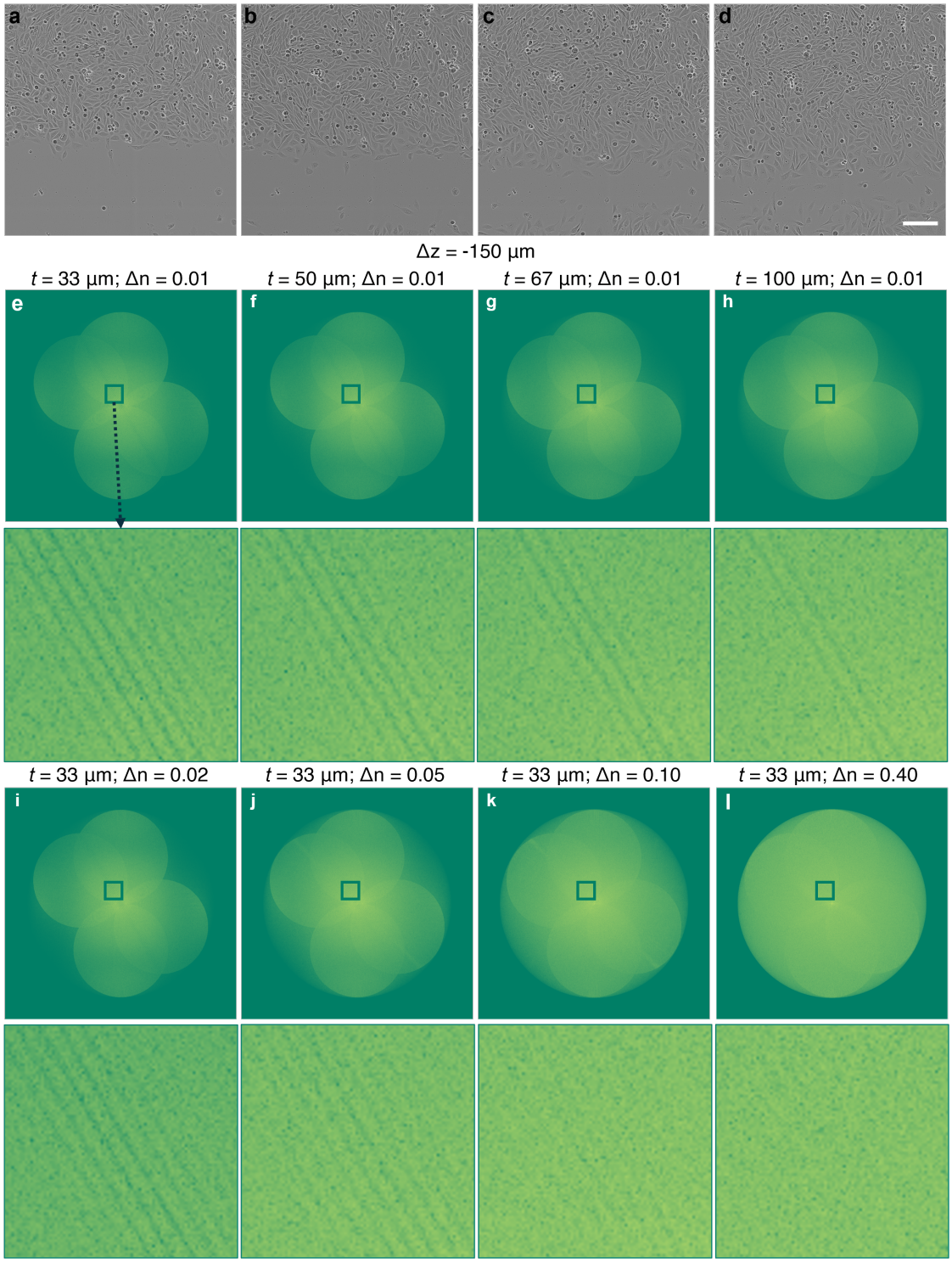

Figure S21: **a-d**, Example planes of the simulated volumetric sample (cell phase imaging video). **e-h**, DAbI fringes under different thicknesses (t) of the sample. **i-l**, DAbI fringes under different scattering characteristics (refractive index range Δn). All the zoomed-in images clearly depict the fringe visibilities. All simulations are done at a defocus distance of $\Delta z = 150$ µm. Scale bar: 100 µm.

8 Effect of sample content on fringe visibility

8.1 Sample content and fringe visibility

According to Eq. (S16) (reiterate below for convenience),

$$\begin{aligned}|\mathcal{F}\{I_1\}+\mathcal{F}\{I_2\}| &= \left|\widehat{A}(\mathbf{k}_\perp)e^{j\widehat{\eta}(\mathbf{k}_\perp)}\right|\left|e^{j\widehat{\phi}(\mathbf{k}_\perp+\mathbf{k}_{1\perp})}+e^{j\widehat{\phi}(\mathbf{k}_\perp+\mathbf{k}_{2\perp})}\right| \\ &\propto \sqrt{2+2\cos\left(\widehat{\phi}(\mathbf{k}_\perp+\mathbf{k}_{1\perp})-\widehat{\phi}(\mathbf{k}_\perp+\mathbf{k}_{2\perp})\right)}, \quad \mathbf{k}_\perp\in\mathcal{S},\end{aligned}$$

under coherent illumination, the cosine fringe visibility of DAbI is modulated by the amplitude term $\left|\widehat{A}(\mathbf{k}_\perp)\right|$. This amplitude term is directly from the intensity spectrum and is associated with the sample content. Here, we analyze the sample content/structures and their effects on the fringe visibility.

For natural or biological samples, the intensity spectrum typically follows a power-law decay [8], in which low spatial frequencies contain most of the image energy and the amplitude falls off approximately as $1/f^\alpha$ toward higher spatial frequencies. As a result, the circular spectral region sampled by DAbI is inherently populated with meaningful signal content. Figure S22 shows representative experimental examples of natural and biological samples. Their amplitude spectra appear noise-like, with DAbI fringes directly modulating the underlying spectral content.

To evaluate robustness across sample diversity, we applied DAbI to a wide range of biological and clinical samples. The lists of sample types and representative raw intensity measurements is provided in Note 8.2.

Other sample types do not follow the power-law decay in the Fourier domain, including resolution targets (USAF1951, Siemens star) and periodic gratings. In Fig. S23 and S24, we showed the fringe visibility of these samples.

1. **USAF1951 resolution target.** Although the USAF1951 target exhibits structured features in the spatial domain, its Fourier spectrum does not contain highly localized or dominant frequency components (Fig. S23). We demonstrate in Fig. 7 of the main paper that DAbI operates reliably on this sample.

2. **Siemens star.** The Siemens star can be regarded as a collection of gratings with continuously varying periods along the azimuthal direction, producing a strongly radial spectrum. When directly applying the algorithm described in Note 4, DAbI may fail due to anisotropic spectral energy distribution. However, a simple modification enables successful operation: replacing "perform FFT on $\mathcal{S}_{\text{sub}}$" with "perform FFT on the sum of $\mathcal{S}_{\text{sub}}$ along the red-arrow direction in Fig. S23**b**" in Algorithm 1. A graphical illustration of this modified procedure is shown in Fig. S23**b3**–**e**.

3. **Gratings.** A grating represents an extreme case of a resolution target. In the idealized scenario, a one-dimensional grating corresponds to a perfect sinusoidal or rectangular waveform, whose Fourier spectrum consists of a small number of Dirac delta functions. In such a hypothetical case, DAbI would fail. In practice, however, fabricated gratings are imperfect and contain scattered spectral components. Figure S24 shows experimental measurements of a one-dimensional phase grating (quantitative phase target, Benchmark Technologies Inc.) at different defocus distances. Both DAbI fringes and cross-shaped spectral patterns are clearly visible. Although the spectrum is dominated by discrete frequencies, the presence of scattered components enables DAbI to function. As in the Siemens star case, a slight modification of the defocus detection algorithm can be applied to accommodate grating-type samples.

From the above analysis, we conclude that the amplitude term $\left|\widehat{A}(\mathbf{k}_\perp)\right|$ does not pose a significant limitation in the practical implementation of DAbI.

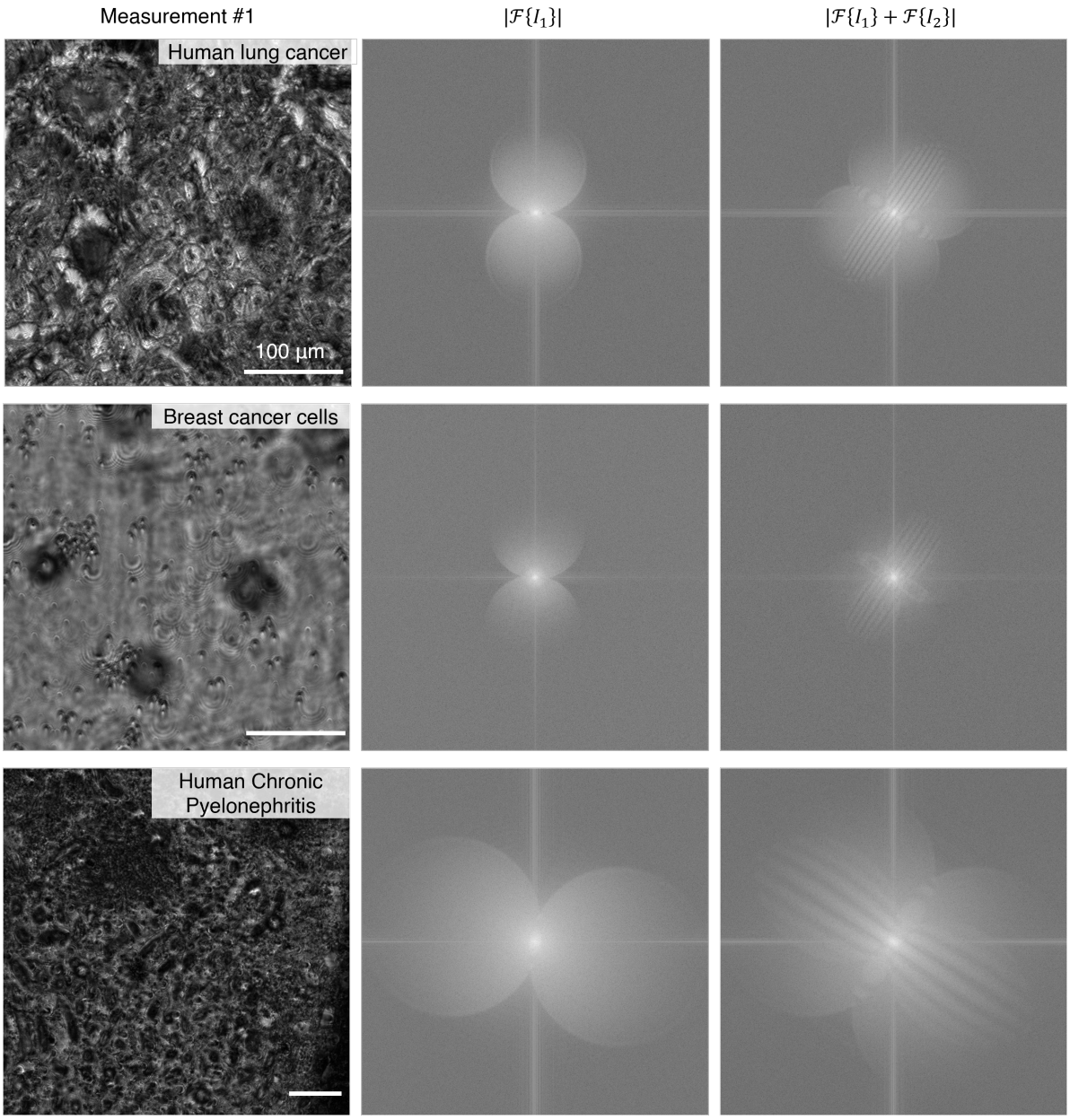

Figure S22: Example experimental raw intensity measurements, amplitude intensity spectrum, and DAbI fringes for out-of-focus 2D biological samples. The differences in circular region size originate from the system specifications, including magnification, camera pixel pitch, illumination wavelengths, and NA. Scale bar: 100 µm.

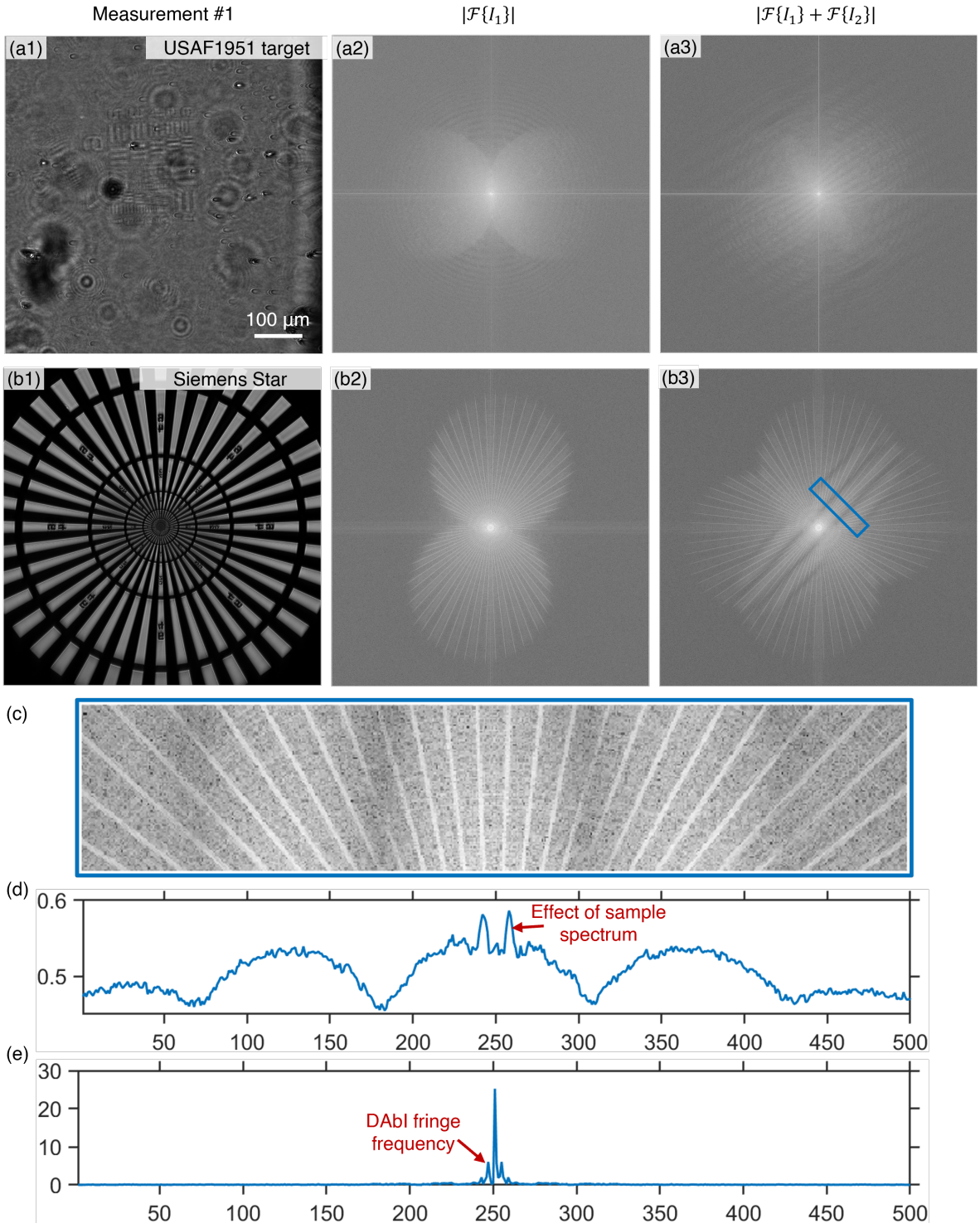

Figure S23: Experimental raw intensity measurements, amplitude intensity spectrum, and DAbI fringes for out-of-focus **a**, USAF1951 and **b**, Siemens star resolution target. **c**, Zoomed-in region of the blue box in **b3**. **d**, Averaged line profile from the vertical direction in **c**. **e**, Fourier transform of the line profile in **d**. Scale bar: 100 µm.

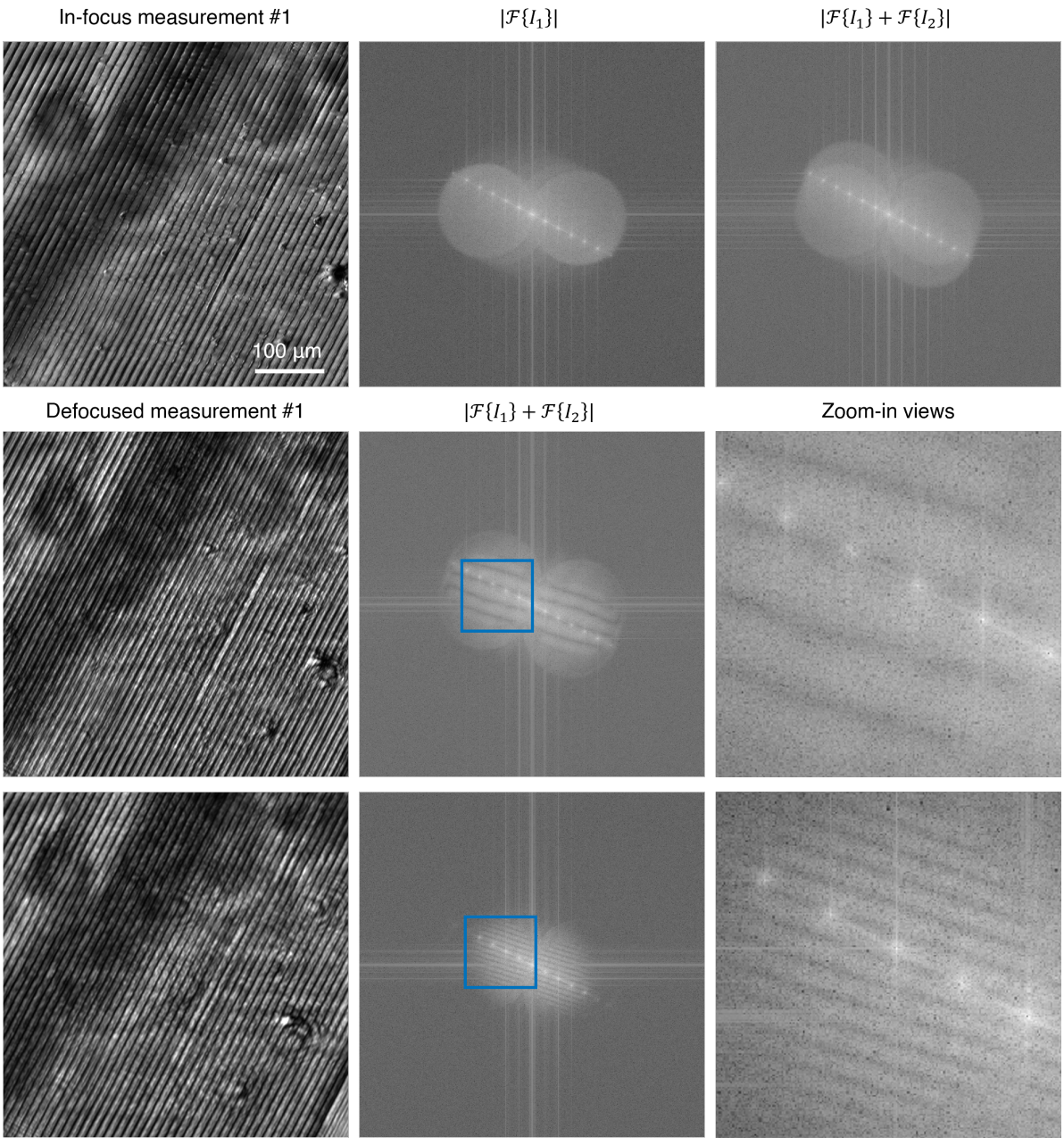

Figure S24: Experimental raw intensity measurements, amplitude intensity spectrum, and DAbI fringes (including zoomed-in regions) for in-focus and out-of-focus 1D phase grating sample. Scale bar: 100 µm.

8.2 Lists of sample information

In this section, we provide detailed sample information studied in Fig. 3 of the main paper. Table S1 presents the sample types in evaluating the 2D autofocusing range, and Table S2 for the 3D autofocusing range. We also provide a few example raw intensity measurements for 2D cases (Fig. S25) and 3D cases (Fig. S26). The H&E-stained human sections are from the human pathology survey slide set (Carolina Biological Supply Inc.). The rest of the sample preparations have been described in the Methods section in the main paper.

Sample Name	**Sample Quantity**
Unstained human non-small-cell lung cancer	5
Unstained human colon cancer	2
Unstained human brain organoid section	1
HEK cell with self-assembling synuclein	1
Unstained mouse brain thin section	1
H&E-stained human seminoma of testis	1
H&E-stained human fibroadenoma of breast	1
H&E-stained viral pneumonia lung	1
H&E-stained human giant nevus congenital	1
H&E-stained human myocardial infarct	1
H&E-stained human brochopneumonia	1
H&E-stained human benign prostatic hyperplasia	1
H&E-stained lily anther early prophase	1
H&E-stained human lung adenocarcinoma	2

Table S1: A list of sample types for 2D autofocusing range evaluation.

Sample Name	**Sample Quantity**
50-µm mouse liver section	2
50-µm mouse kidney section	1
40-µm mouse brain section	2
70-µm mouse brain section	1
50-µm mouse lung section	1
70-µm mouse lung section	2
90-µm mouse lung section	1
150-µm mouse lung section	1
50-µm mouse heart section	2
70-µm mouse heart section	1
90-µm mouse heart section	1
50-µm mouse skin section	1
70-µm mouse skin section	1
90-µm mouse skin section	1
50-µm mouse spleen section	1
50-µm human brain organoid section	1

Table S2: A list of sample types for 3D autofocusing range evaluation.

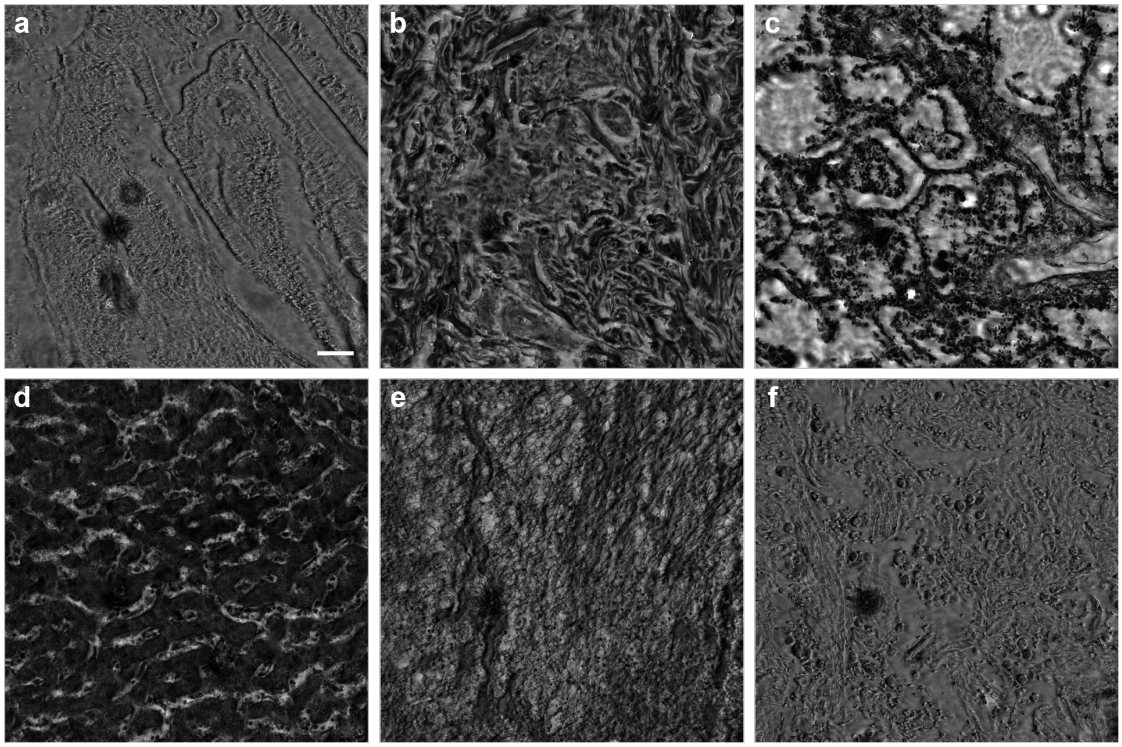

Figure S25: Example experimental raw intensity measurements for out-of-focus 2D samples. **a**, Unstained colon cancer. **b**, H&E-stained giant nevus congenital human section. **c**, H&E-stained human Bronchopneumonia. **d**, H&E-stained human cirrhosis of liver. **e**, H&E-stained human myocardial infarct. **f**, Unstained non-small-cell lung cancer. Scale bar: 50 µm.

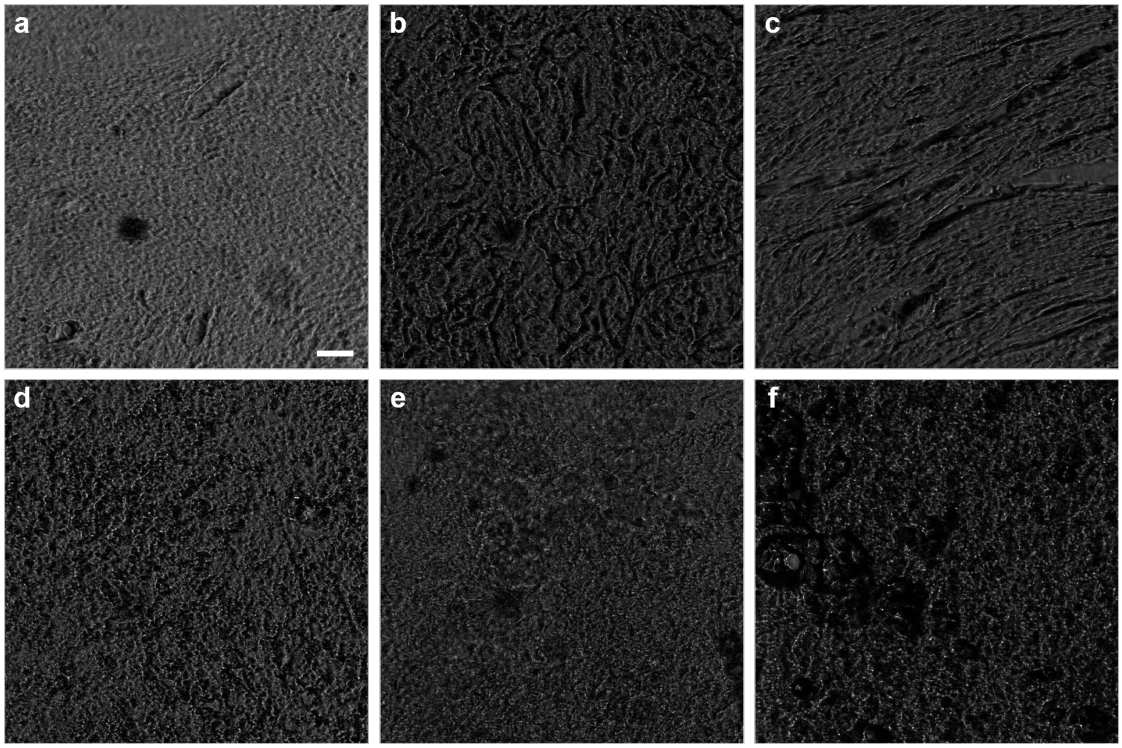

Figure S26: Example experimental raw intensity measurements for out-of-focus 3D samples. **a**, 40-µm mouse brain section. **b**, 70-µm mouse heart section. **c**, 50-µm mouse kidney section. **d**, 50-µm mouse liver section. **e**, 70-µm mouse skin section. **f**, 150-µm mouse lung section. Scale bar: 50 µm.

9 Comparison with other autofocusing methods

Autofocusing in optical microscopy has been a heated topic over the past decades. A wide range of methods have been proposed and applied. A recent review article on autofocusing has summarized the existing methods [9]. Based on the review article, we compared our DAbI technique with the other nine categories of methods across different dimensions. Due to all these methods being suitable for different scenarios with various restrictions, it is impossible to benchmark them on the same imaging platform or even on a consistent simulation environment. Therefore, we did a qualitative comparison of all these categories and discussed the pros and cons of every category.

9.1 Dual-LED methods

Dual-LED [10–12] has a simple optical setup that shares similarity with the DAbI setup. It uses two opposite LEDs to record a single intensity image. When the sample is out of focus, these two opposite LED illuminations create a lateral shift at the image plane, producing a two-copy intensity image (Fig. S27). The dual-LED methods utilize this two-copy effect to find a linear correlation between the lateral shift and defocus distance. The quantification of lateral shifts is performed through the autocorrelation of the intensity image. Given this two-copy effect, there exist two side peaks in the autocorrelation profile. Additionally, the dual-LED methods have a variant using two intensity measurements from two opposite LED illuminations sequentially [13]. The use of two images can help identify the defocus direction.

Mathematically, the two diametrically opposite LEDs illuminate the sample with symmetric oblique angles ($\pm\beta$, with β as the polar angle, shown in Fig. S27). When the sample is at a defocus distance of Δz, each oblique illumination results in a geometrical projection of the sample onto the focal plane. Due to the oblique illumination, this projection introduces a lateral displacement for each intensity image:

$$\Delta y_{\pm} = \pm \Delta z \tan \beta. \tag{S151}$$

Then, the total displacement from the two opposite LED illumination is:

$$2\Delta y = 2\Delta z \tan \beta. \tag{S152}$$

The captured intensity image from the dual-LED method has a two-copy effect with a separation of $2\Delta y$. This separation can be computed through finding the side peak location in auto-correlation. Finally, the defocus distance can be calculated through Eq. (S152).

Although DAbI and dual-LED methods share similarity in the optical system setup, where both methods employ oblique illuminations, the fundamental physics insight and methods are different between these two methods, and DAbI demonstrates significantly superior autofocusing performance.

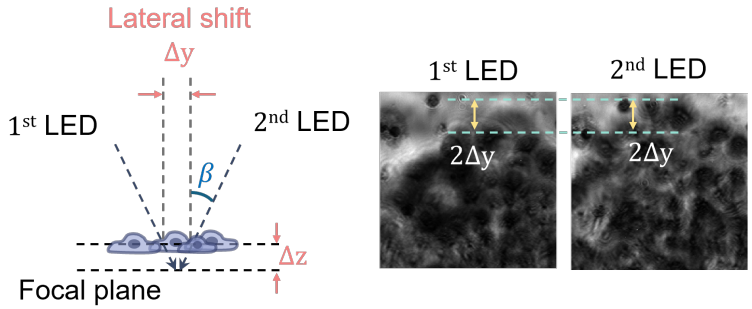

Figure S27: A graphical demonstration of lateral shifts in dual-LED methods.

Dual-LED relies on a geometric-optics image-translation model and extracts defocus from image shift. DAbI is derived from a wave-optics image formation model, where the fringe modulation arises from the digital interference between two shifted defocus pupil functions in the intensity spectrum. *The fringes' properties under DAbI settings can not be correctly and fully explained by the lateral image translation and Fourier translation theorem.* Therefore, we conclude that the theoretical framework from the dual-LED methods is

limited, while the theory we explain DAbI is much more comprehensive and in-depth, leveraging significant advantages in the algorithm design. We aim to illustrate the difference between the principles and the distinction between DAbI fringes and fringes introduced by lateral translation in dual-LED methods with the following four **Differences**.

Difference 1: Dual-LED theory cannot explain why the fringes in DAbI only appear in a constrained region in the intensity spectrum.

In DAbI, the approximately straight fringes are constrained in a specific region $\mathcal{S}$ and its centrosymmetric part, as shown by both simulations (Fig. S28**a**) and experiments (Fig. S28**b**). Furthermore, within the other region $\mathcal{S}^*$ (defined in Eq. (S17)) and its centrosymmetric part, we can observe sparse and circular fringes (Indicated by the white arrow in Fig. S28). The formation of these distinct fringe patterns in $\mathcal{S}$ and $\mathcal{S}^*$ is well explained by digital interference of two shifted aberration pupils in DAbI theorem. However, the image lateral shifts model of dual-LED methods can not explain these fringe patterns.

Suppose the original in-focus image is $I_0(x, y)$. Due to illumination from two diametrically opposite LEDs, the two intensity images captured by the camera can be approximated as

$$I_1(x, y) \approx I_0(x, y + \Delta y), \qquad I_2(x, y) \approx I_0(x, y - \Delta y), \tag{S153}$$

We neglect the image blur caused by defocus and consider only the geometric lateral displacement as the dual-LED method.

The autocorrelation between I_1 and I_2 yields a peak corresponding to the total lateral shift $2\Delta y$. Equivalently, according to the Fourier translation theorem, the Fourier transform of the summed image exhibits a cosine modulation:

$$\begin{aligned} |\mathcal{F}\{I_1 + I_2\}| &= \left|\mathcal{F}\{I_0\}\left(e^{-ik_y\Delta y} + e^{+ik_y\Delta y}\right)\right| \\ &= 2\,|\mathcal{F}\{I_0\}|\,|\cos(k_y\Delta y)| \end{aligned} \tag{S154}$$

Eq. (S154) shows that the fringes introduced by lateral shift should cover all spectrum within pupil constraints. That is to say, within all overlap regions in the spectrum ($\mathcal{S}$ and $\mathcal{S}^*$ and their centrosymmetric part in Fig. S28), there should exist evenly spaced fringes. However, this is both theoretically and experimentally not accurate in DAbI. The circular fringes within the region $\mathcal{S}^*$ can only be explained by our theoretical analysis in Note 1.

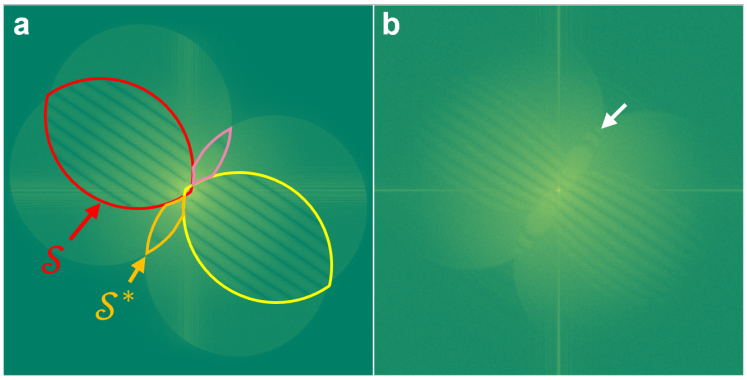

Figure S28: DAbI spectral fringe patterns at different regions under a defocus distance of 30 μm with 20×/0.40NA system: **a**, simulation and **b**, experiment.

Difference 2: Dual-LED theory cannot explain the curved fringes in DAbI, especially in high NA settings.

As we discussed in Note 1.5, the DAbI fringes may not be straight. Especially in a high-NA setting, we observe curved fringes in set $\mathcal{S}$ (Fig. S4). However, the curved fringes cannot be explained through the dual-LED theory. The auto-/cross-correlation of the image(s) should result in evenly spaced periodic patterns, rather than curved patterns.

Difference 3: Dual-LED theory cannot work when the image translation is very large (similar to image size), while DAbI can.

Dual-LED methods heavily rely on image translation. If the image shift is close to the FOV size, the dual-LED methods can barely detect defocus distances due to the limited image overlap. In contrast, thanks to the in-depth theory support from wave-optics and aberration analysis, DAbI together with the system and algorithm design obtained a better signal-level in defocus detection. We validate this point with the following experiment.

Here, we experimentally demonstrate that capturing 256×256-pixel intensity images (20×/0.40NA, a camera pixel pitch of 6.5 µm, and the same illumination angles) at a defocus distance of 450 µm. Figure S29 a,b shows the experimental raw intensity images under the above setting for DAbI. Theoretically, the lateral shift should be in the vertical direction for 229 pixels, which is very close to the FOV size. That is to say, the two images only have a 10% overlapping region. If we perform the cross-correlation of these two images, we cannot find the peak in the cross-correlation profile (Fig. S29**c**).

Instead, when we apply the DAbI algorithm, given that it is wave-optics based, we can use the virtual defocus aberration strategy to digitally propagate inverse virtual defocus distance (150 µm) back to break the samping rate limit and get good peaks indicating a modified defocus distance of 300 µm, as shown in Fig. S29**d**. The reason why DAbI could work in this low overlapping case is that fundamentally DAbI fringes originate from the digital interference of two shifted defocus pupil functions in the intensity spectra, rather than the image lateral shift. Even if the sample content of two images is mostly different due to the large defocus distance and the small patch size, the corresponding sample spectrum $\widehat{O}(\mathbf{k}_\perp)$ still shares some similarity, especially in the low frequency part. The two shifted defocus aberration pupil can still produce DAbI fringes after virtual strategy, on top of random sample phase modulations.

To make a fair comparison, we implemented dual-LED methods (256×256-pixel, 20×/0.40NA, camera pixel pitch 6.5 µm, and illumination angle $\beta = 12.3°$) at certain defocus distances that has a similar number of shifts between two images, around 202 and 269 pixels. The resultant detection of defocus fails in the dual-LED method, as shown in Fig. S29**e,f**.

Difference 4: Dual-LED cannot work on volumetric samples, while we developed a theory for DAbI to work on autofocusing of thick samples (Note 2).

Dual-LED methods have been adapted to autofocusing for 2D samples, however, they have not been reported for autofocusing volumetric samples from both theory and experimentations. On the contrary, we have developed a comprehensive theoretical framework (Note 2), together with system and algorithm design, enables the validity of autofocusing in thick samples using DAbI. We have shown experimental demonstrations of thick sample autofocusing in Figure 4 in the main paper.

In Figs. S30 and S31, we provide additional details comparing the thick-sample autofocusing performance of the dual-LED method and DAbI. Specifically, we evaluate the autofocusing capability of DAbI and the dual-LED approach using a 150 µm–thick mouse kidney tissue section. All system parameters for DAbI and the dual-LED method are identical to those described in **Difference 2** of this section, except that a FOV of 2048×2048 pixels is used. Two representative defocus distances, 125 µm and 450 µm, are tested and presented in Figs. S30 and S31, respectively. In both cases, under DAbI illumination settings, we observe clearly visible DAbI fringes, enabling accurate estimation of the defocus distance. In contrast, the dual-LED method fails to reliably detect the defocus distance under these thick-sample conditions.

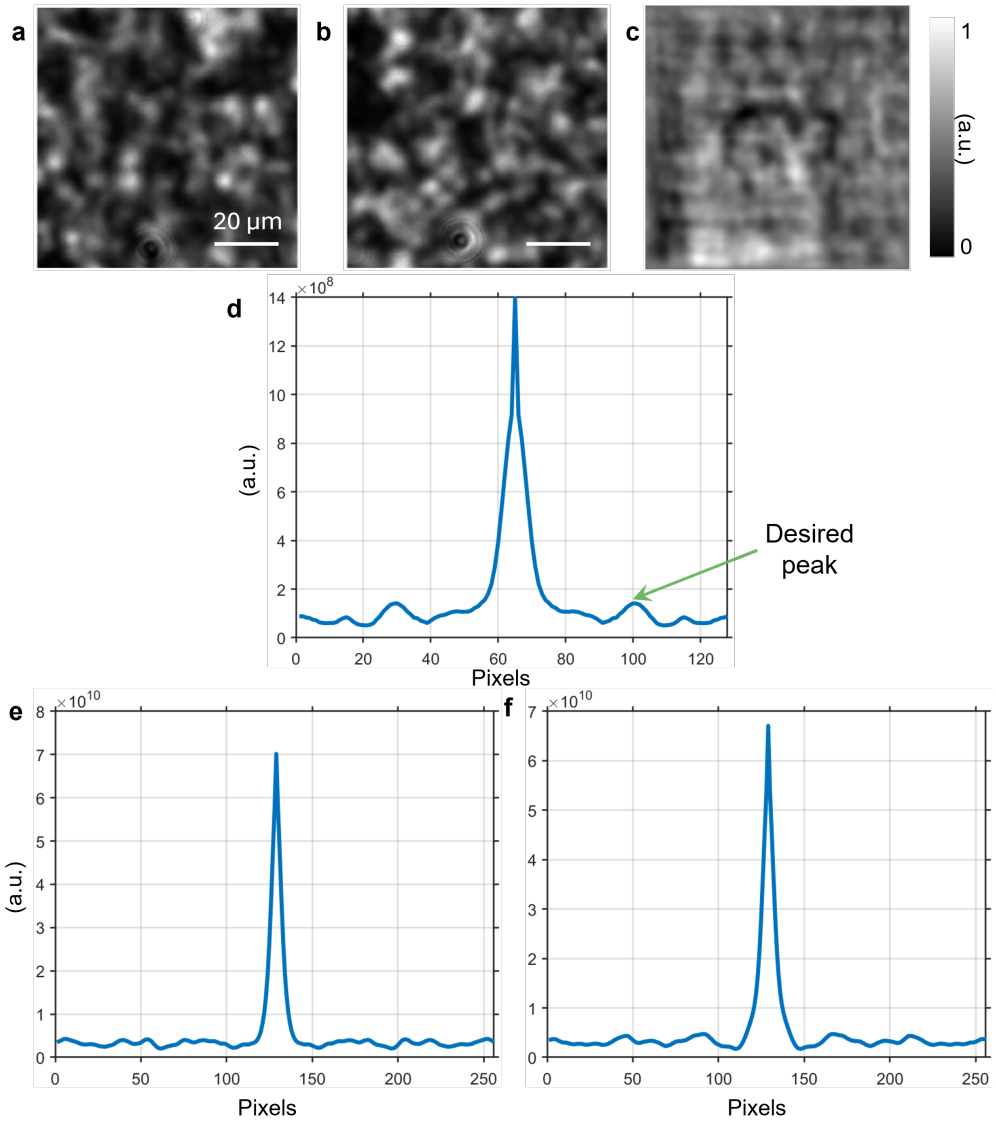

Figure S29: Experimental comparison for dual-LED methods and DAbI. **a,b**, Two intensity images from DAbI. **c**, Cross-correlation profile between **a** and **b**. **d**, Line profile of fringe detection with DAbI in the Fourier domain with a 229-pixel lateral shift. A virtual defocus distance of 150 µm has been applied. The arrow indicates the correct fringe spacing that corresponds to 449.1 µm (ground truth 450 µm). Fringe spacing detection using dual-LED methods with a lateral shift of **e**, 202 pixels and **f**, 269 pixels, respectively.

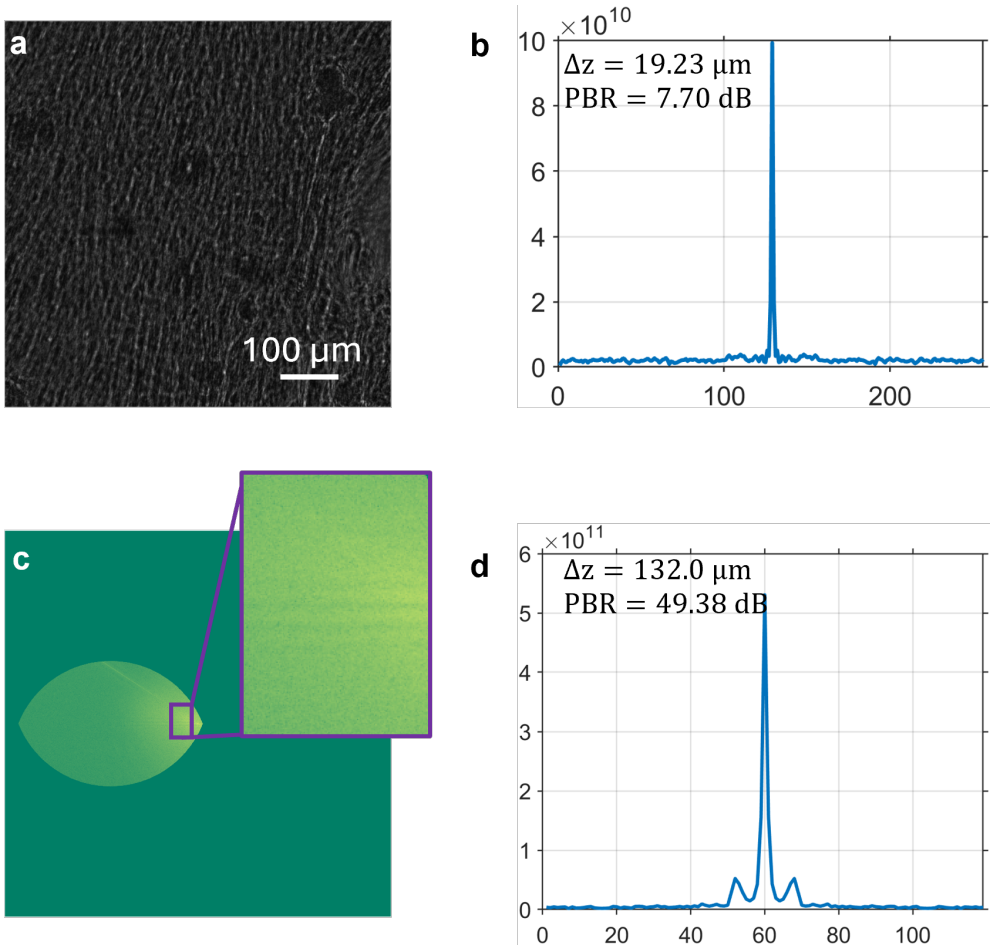

Figure S30: Experimental comparison for dual-LED methods and DAbI in a thick sample at a small defocus distance. **a**, Raw intensity image from dual-LED methods. **b**, dual-LED defocus detection failed. **c**, DAbI fringes of a thick sample in the experiment. **d**, DAbI successfully detects the defocus distance. Ground truth defocus: 125 µm, PBR stands for peak-to-background ratio.

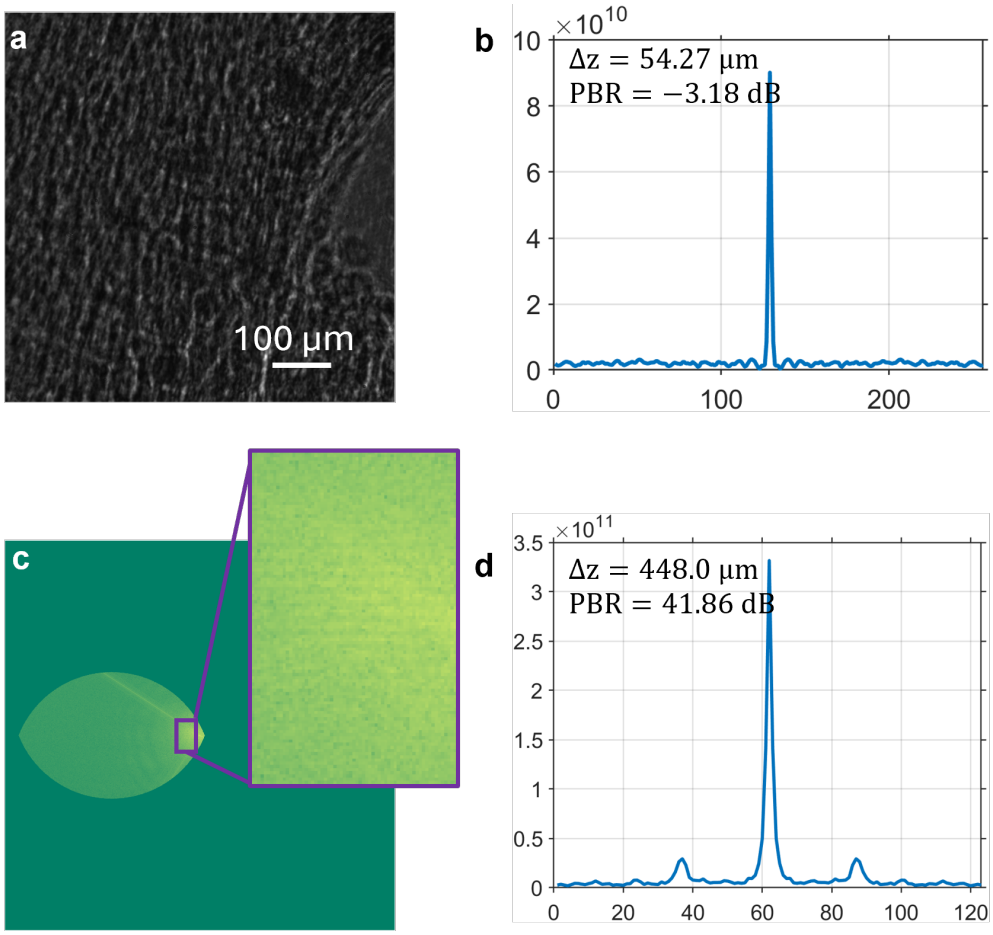

Figure S31: Experimental comparison for dual-LED methods and DAbI in a thick sample at a large defocus distance. **a**, Raw intensity image from dual-LED methods. **b**, dual-LED defocus detection failed. **c**, DAbI fringes of a thick sample in the experiment. **d**, DAbI successfully detects the defocus distance. Ground truth defocus: 450 μm, PBR stands for peak-to-background ratio.

Differences in algorithm and system design: *Compared with dual-LED, DAbI introduces a virtual defocus aberration strategy in its algorithm and adopts a different illumination configuration.*

According to the DAbI theorem, the contribution of each individual intensity spectrum within the fringe region $\mathcal{S}$ can be approximated as the complex field of the sample spectrum multiplied by a shifted pupil function. This formulation implies that the corresponding complex field can be digitally propagated forward or backward, and its phase can be deliberately manipulated to modify the DAbI fringe characteristics. This observation motivates the proposed virtual defocus aberration strategy in our algorithm design. The most important application of this strategy arises in the small defocus regime, where interference fringes are not directly observable. In such cases, DAbI can digitally propagate the complex fields to larger defocus distances, thereby enhancing fringe visibility and enabling accurate defocus distance estimation. This mechanism allows robust autofocusing over the entire operational focusing range.

Beyond defocus magnitude estimation, the virtual defocus aberration strategy further enables determination of the defocus direction, compensation of fringe curvature in high-NA systems with iterative algorithms, and correction of image distortions caused by inherent system aberrations.

In contrast, conventional dual-LED methods are based on geometric optics and perform auto- or cross-correlation directly on intensity images. As a result, they lack access to complex field information and cannot implement analogous virtual propagation strategies. Consequently, dual-LED approaches fail to reliably handle small defocus distances. A comprehensive performance comparison between DAbI and dual-LED methods at small defocus distances is presented in the following **Comparison of performance** paragraphs in this section.

Based on the DAbI principle and the virtual defocus aberration strategy, we design DAbI illumination patterns that are fundamentally different from dual-LED approaches. Instead of positioning two LEDs diametrically opposite to maximize image shift, DAbI places two illumination LEDs close to each other (small azimuthal illumination angle θ), with a polar illumination angle β approaching the system NA (Fig. S32). This configuration effectively enlarges the interference fringe region $\mathcal{S}$. As a result, DAbI achieves higher fringe contrast, improved defocus detection accuracy, and a substantially extended autofocusing range, as demonstrated by the performance comparison below.

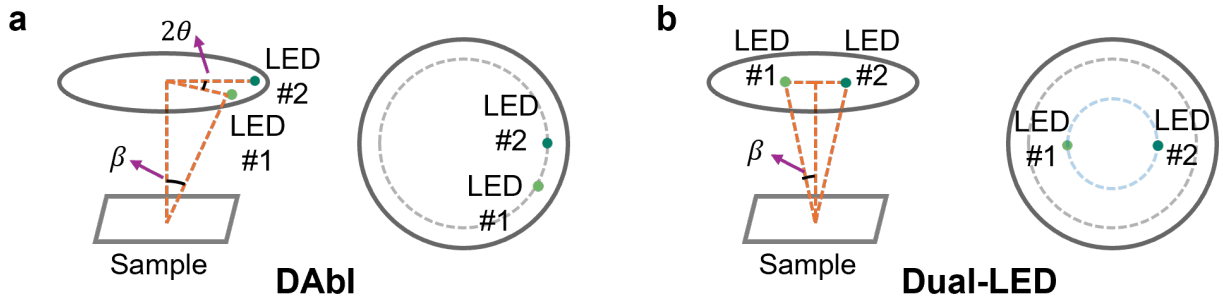

Figure S32: Illumination setup schematic for **a**, DAbI, **b**, dual-LED methods

Comparison of performance: *At the same level of accuracy, compared with dual-LED methods, DAbI covers a broader range for defocus detection.*

Apart from principles and methodology, our method shows superior defocus detection capability compared with dual-LED methods. To make a fair comparison, we calibrated dual-LED and DAbI on the same imaging system with the same set of samples. We implemented both methods under two settings: (1) $20\times/0.40$NA objective lens, with $\beta = 23.0°, \theta = 11.25°$ for DAbI and $\beta = 12.3°, \theta = 90°$ for dual-LED methods; (2) $40\times/0.65$NA objective lens, with $\beta = 23.0°, \theta = 11.25°$ for DAbI and $\beta = 12.3°, \theta = 90°$ for dual-LED methods. Note that the values of β, θ in dual-LED methods were derived from the reference [11]. In both settings, a camera (PCO edge 5.5) with a pixel pitch of 6.5 µm was used. The samples used in these experiments varied across stained and unstained human tissues, mouse tissues, and cellular-type samples. Additionally, 4-6 samples (stained and unstained) were used for system calibration for both methods, and these results were included in the following Figures.

We compare the performance of the two methods in Figs. S33, S34, S35, and S36. Under the $20\times/0.40$NA configuration, DAbI method achieved high focusing accuracy within the system DoF (± 4.06 µm) and con-

sistently maintains this performance from 0 µm to approximately 900 µm on one side of the focal plane (top panel of Fig. S33). This corresponds to an autofocusing range of 1800 µm, which is approximately 443 times the native DoF. In contrast, the dual-LED method maintained high accuracy only up to about 300 µm (bottom panel of Fig. S33). Beyond this range, its focusing error increases substantially, frequently exceeding the system DoF and in some cases surpassing 10 µm, as indicated by the red crosses and annotations in Fig. S33.

At small defocus distances (e.g., less than 30 µm), the image shifts induced by defocus are minimal. As a result, the dual-LED method had limited ability to reliably resolve these shifts, leading to frequent failures in defocus estimation (Fig. S34). In contrast, DAbI, enabled by the virtual defocus aberration strategy (Note 1.6), was capable of accurately detecting small defocus, with the resulting errors remaining within the DoF (Fig. S34).

We further evaluated a comparison under a different system configuration (40×/0.65 NA) to evaluate the generalizability of the above conclusions. As shown in Figs. S35 and S36, DAbI consistently maintained high focusing accuracy from 0 µm to approximately 270 µm in one axial direction, corresponding to an effective range of 365× the native DoF. In contrast, the dual-LED method remains reliable only within a much narrower range of approximately 5–110 µm.

The performance advantages of DAbI at both large and small defocus distances are particularly beneficial for biological and clinical microscopy applications. For instance, in multi-well plate bioimaging (e.g., 96- or 48-well formats), switching between wells can introduce substantial defocus offsets, necessitating a long-range autofocusing capability. Conversely, whole-slide pathology imaging typically involves gradual axial variations, for which high sensitivity to small defocus distances is critical. These performance advantages establish DAbI as a powerful tool for microscopic autofocusing.

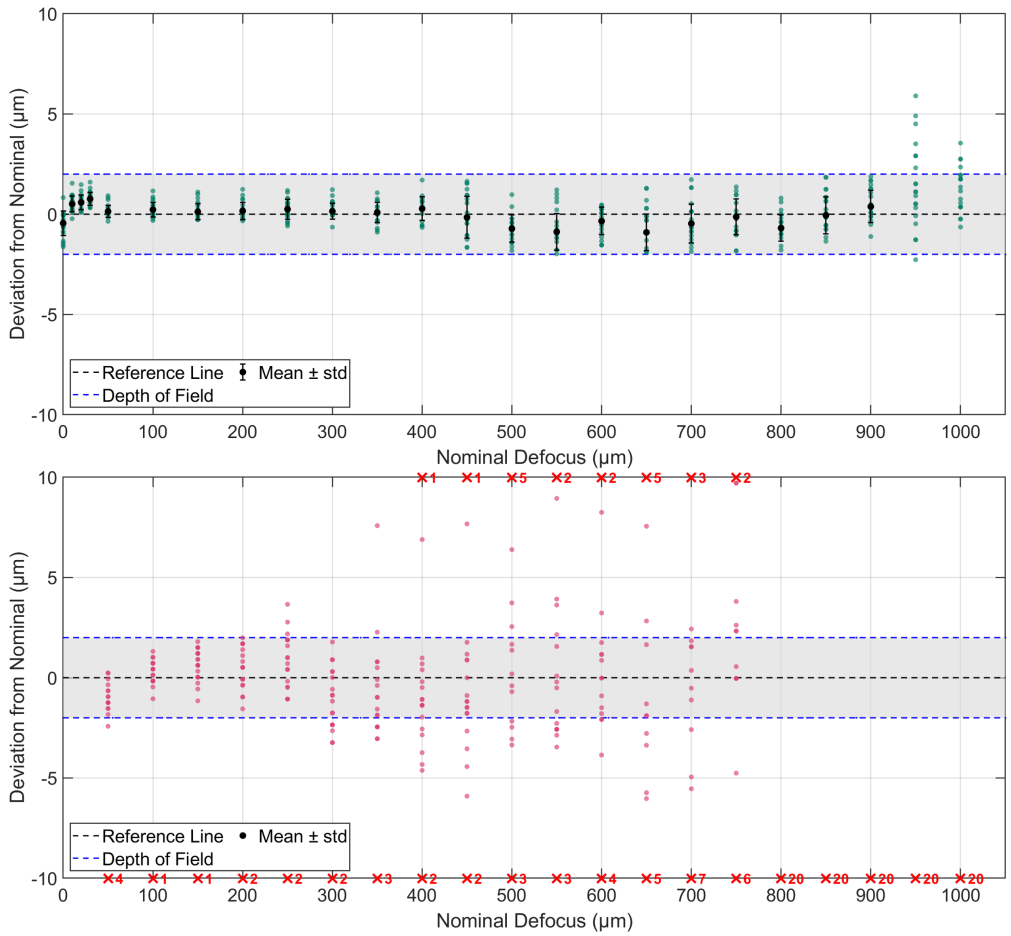

Figure S33: Experimental comparison of autofocusing performance of DAbI (upper panel) and dual-LED method (bottom panel) over a long range under the 20×/0.40NA setting with 20 samples (n=20). The red crosses and annotations denote the number of significantly failed cases.

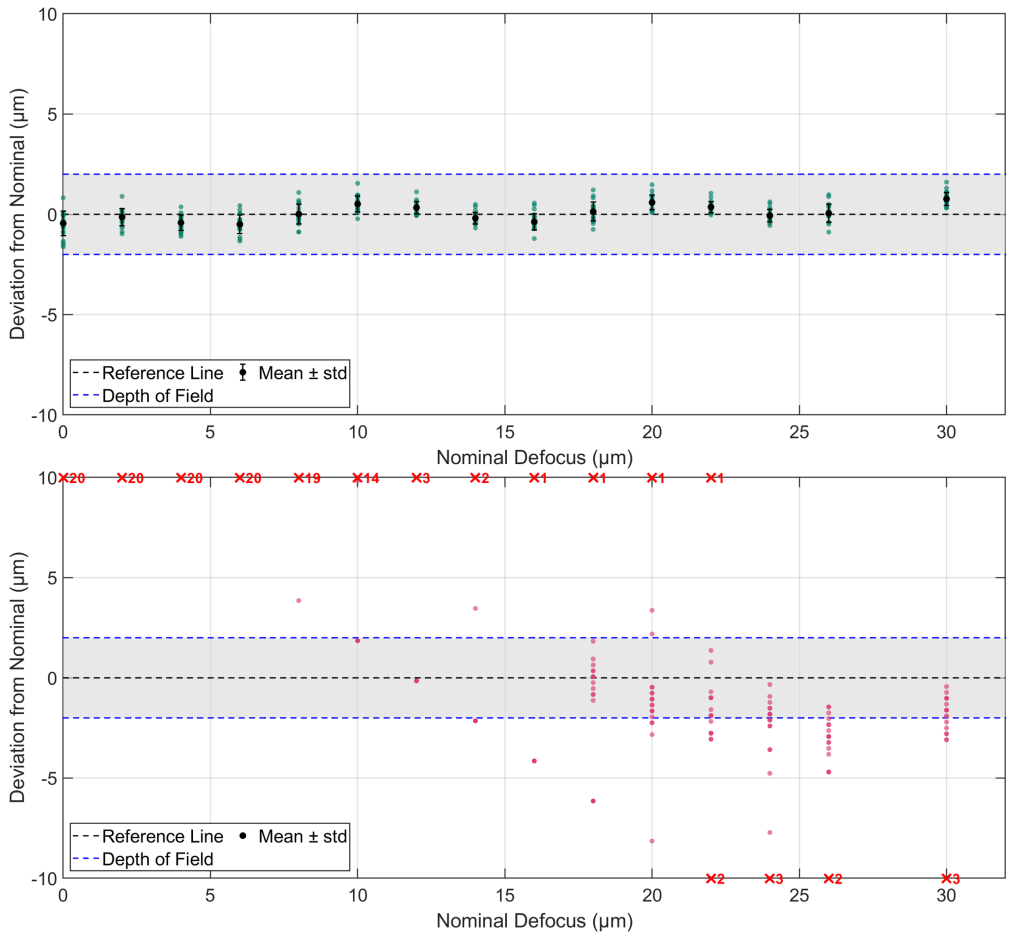

Figure S34: Experimental comparison of autofocusing performance of DAbI (upper panel) and dual-LED method (bottom panel) at small defocus distances under the 20×/0.40NA setting with 20 samples (n=20). The red crosses and annotations denote the number of significantly failed cases.

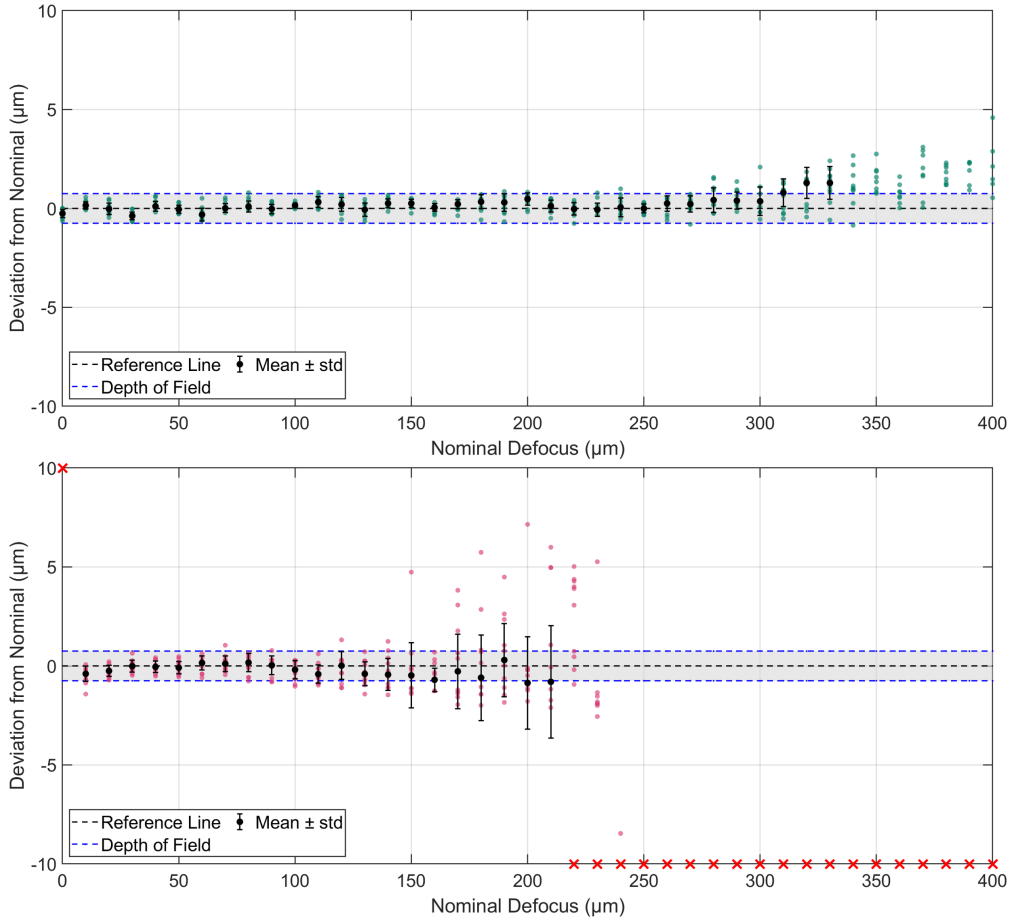

Figure S35: Experimental comparison of autofocusing performance of DAbI (upper panel) and dual-LED method (bottom panel) over a long defocus range under the 40×/0.65NA setting with 10 samples (n=10). The red crosses denote the significantly failed cases.

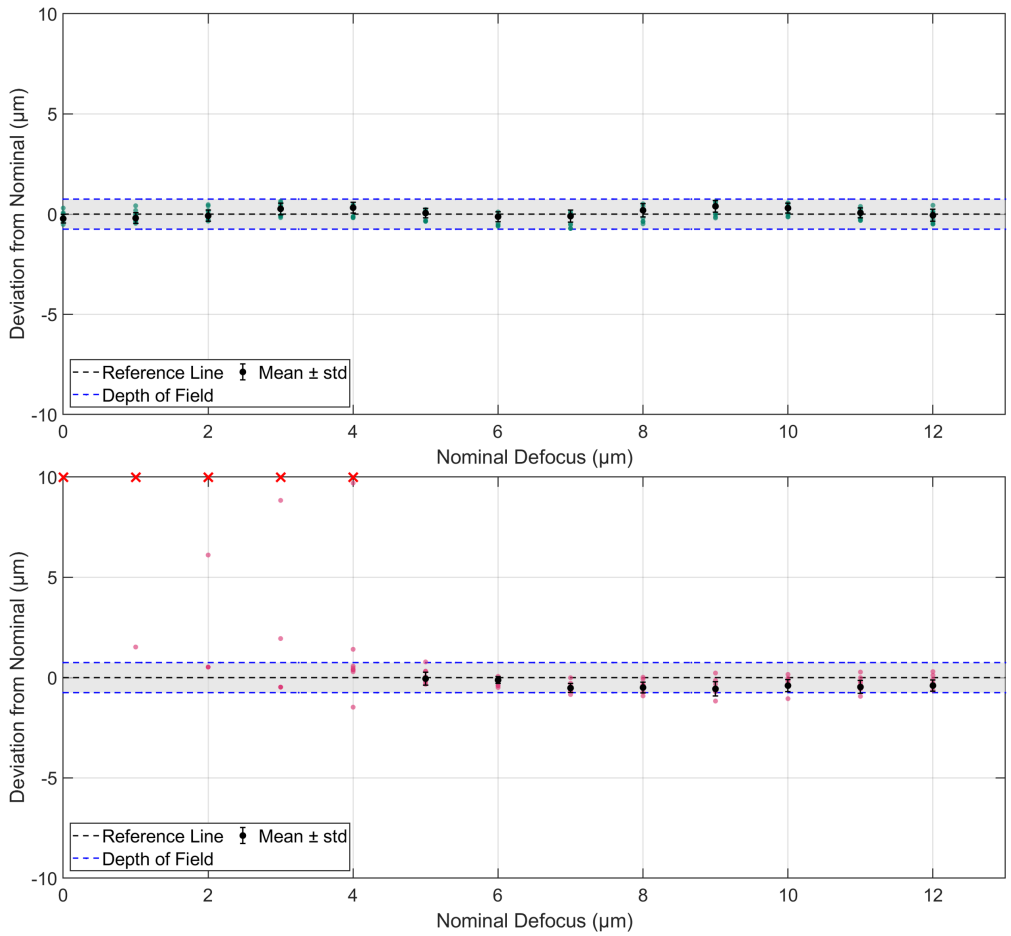

Figure S36: Experimental comparison of autofocusing performance of DAbI (upper panel) and dual-LED method (bottom panel) at small defocus distances under the 40×/0.65NA setting with 10 samples (n=10). The red crosses denote the significantly failed cases.

9.2 Focus metric methods

The focus metric methods [14–17] have been widely studied for their simplicity (no requirements for any system modifications). Typically, metrics are used as the guidance for a search algorithm along multiple axial positions (e.g. golden search). Alternatively, these methods typically compute metrics for an image stack along the axial direction (e.g. coarse-to-fine method). Then the optimal metric is selected to represent the best focus plane. A variety of focus metrics have been proposed and implemented for different microscopes or sample types.

The autofocusing range of the focus metric is constrained by a predefined range (the defocus search range). A larger search range is accompanied by more image acquisitions, leading to increased light exposure and prolonged autofocusing time.

If the metrics are strictly monotonic on each side of the focal plane, finding the optimal focal plane within a predefined range becomes a convex optimization problem. Golden-section or Fibonacci search will therefore yield the optimal solution [18].

Given a desired accuracy of DoF ($\delta\alpha$) and a predefined search range $[-Z, Z]$, where the initial interval length is $L_0 = 2Z$, the golden-section search (similar to binary search, but with a ratio of $\delta\mu = \frac{1+\sqrt{5}}{2}$) shrinks the search range by a constant factor at each iteration:

$$L_t = L_0 \left(\frac{1}{\delta\mu}\right)^t, \tag{S155}$$

where t denotes the t^{th} iteration.

To guarantee that the final uncertainty interval is no larger than the desired accuracy, we require

$$L_t \leq \delta\alpha. \tag{S156}$$

Substituting the expression for L_t yields

$$2Z \left(\frac{1}{\delta\mu}\right)^t \leq \delta\alpha, \tag{S157}$$

which leads to the following lower bound on the number of iterations:

$$t \geq \frac{\ln\left(\frac{2Z}{\delta\alpha}\right)}{\ln(\delta\mu)}. \tag{S158}$$

In golden-section search, two evaluations are required for initialization, and each subsequent iteration introduces one new evaluation by reusing a previously sampled point. Therefore, the total number of image acquisitions (focus metric evaluations) required to achieve accuracy $\delta\alpha$ is

$$N_{\text{img}} = t + 2 = \left\lceil \frac{\ln\left(\frac{2Z}{\delta\alpha}\right)}{\ln(\delta\mu)} \right\rceil + 2. \tag{S159}$$

We validated these image acquisition needs through experiments and compared them with DAbI (shown in Fig. S37). Examples of using four different metrics on the same sample to find the focal plane with an accuracy of <DoF (Fig. S38). An example of sequentially captured images through golden search is presented in Fig. S39.

Through our experiments, we found that the golden search algorithm is valid when the predefined search range is small. In our demonstrated experiments, this predefined search range is smaller than ±30 µm under a 20×/0.40NA objective lens. If the predefined range gets larger, the monotonicity of focus metrics at each side of the focal plane may not be valid (shown in Fig. S40). In such a situation, a coarse-to-fine strategy is efficient and robust, with a sequential axial scanning with big steps, followed by the golden search within a small interval. In this case, many more image acquisitions are needed.

In addition to the autofocusing range and the number of image acquisitions, the focus metric also requires multiple mechanical movements along the axial direction, while DAbI only needs one mechanical move. These moves and stops significantly increase the autofocusing time.

Finally, it lacks a uniform metric suitable for general scenarios [9]. Different metrics may suit for distinctive sample types. For example, in Fig. S41, we experimentally demonstrate that for an unstained human pathology tissue sample, the Laplacian variance metric works on finding the focal plane, while other metrics failed.

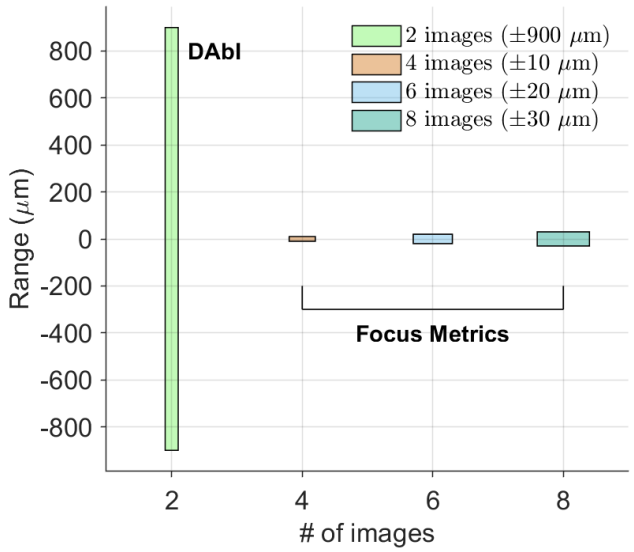

Figure S37: Comparison between DAbI and focus metric methods. The vertical axis indicates the defocus detection range, and the lateral axis denotes the number of images needed to find the focal plane.

9.3 Tilted sensor methods

The tilted sensor methods [19–21] utilize the oblique placement of a focusing sensor. A beam splitter is implemented to direct part of the light to the image sensor and the rest to the focusing sensor. The center of the tilted sensor is conjugate to the focal plane of the imaging system. The optimal focus position can be inferred by locating the peak of the contrast curve in real time.

The autofocusing range of this method is constrained by the tilt angle of the focusing sensor. A larger oblique angle yields a longer autofocusing range, but at the cost of focusing precision. Additionally, this method may not work for transparent samples, since out-of-focus regions have a higher contrast.

9.4 Deep learning methods

Recently, deep learning methods have gained significant popularity in various applications. In the field of 2D autofocusing, some image-based deep learning methods [22–28] output a defocus value and then move the sample back to the focal plane. This type of method only requires a single image capture. The other type of method [29–32] directly generates an in-focus image from an out-of-focus image using generative models. The nature of this type of method is actually extending the DoF (DoF) digitally. However, the existing papers still categorize these deep learning methods as autofocusing methods.

In both cases, the deep learning methods suffer from generalization issues. They can be sample-dependent and system-dependent. The validity of these methods relies on high-quality, large-scale training datasets, which hinders the wide application of these methods.

9.5 Phase detection methods

Phase detection autofocusing has been extensively used in most digital single-lens reflex cameras (DSLR) [33]. It separates the incoming light into two beams and records paired images. The translation shifts between the two images can infer the defocus amount.

This concept has also been applied to optical microscopy [34–36] with an additional focusing sensor and some optical modifications. This type of method is fast but requires precise optical alignments and calibrations. Compared with DAbI, phase detection methods cannot achieve a long autofocus range, since the additional sensor has a limited size. The method requires a beam splitter and other optical components, which reduces the light efficiency. This photon budget becomes critical when automating fluorescence microscopes.

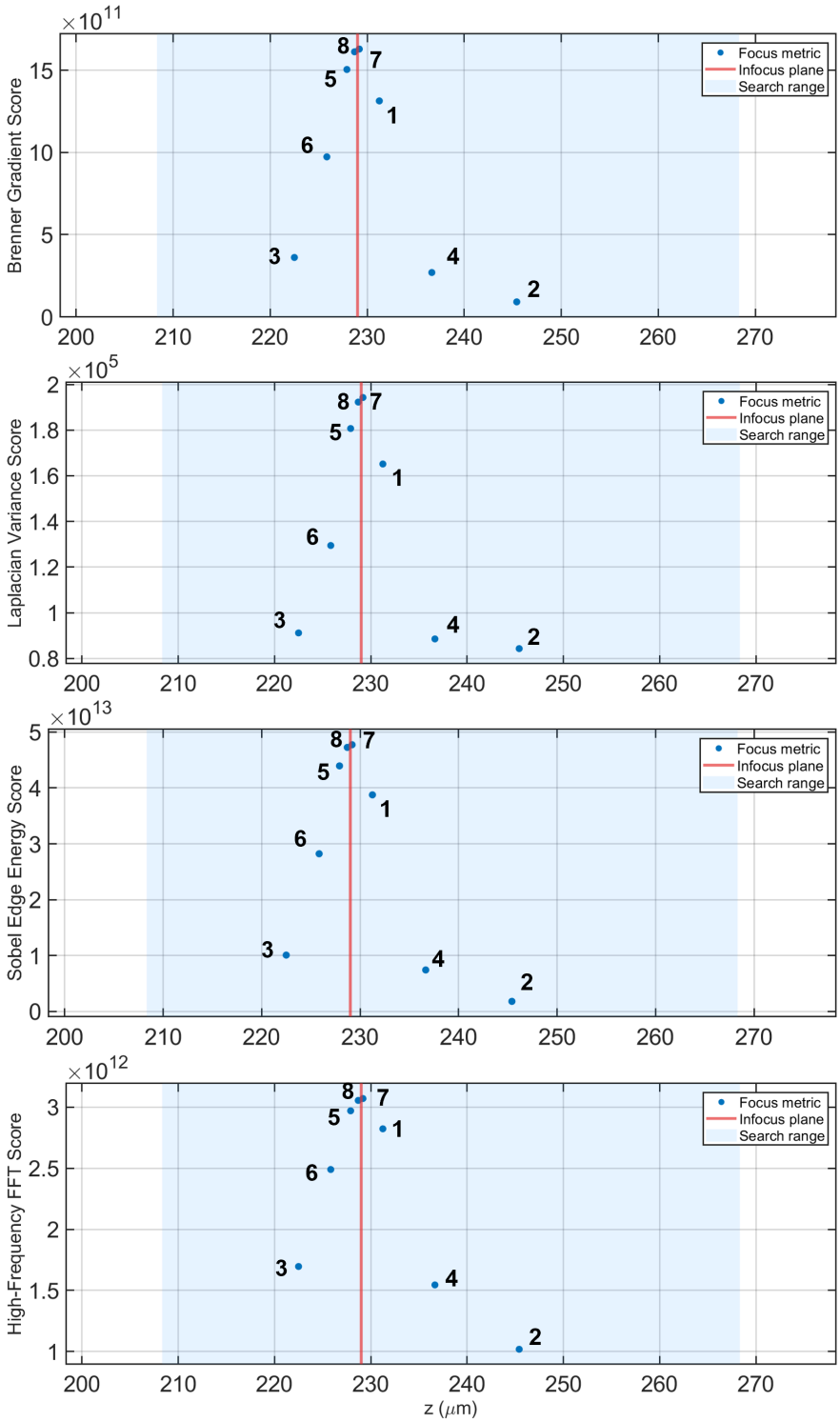

Figure S38: An experimental example of focus metric golden search within a range of ±30 µm. The numbers in the figure correspond to the focus metrics of the sequentially captured images.

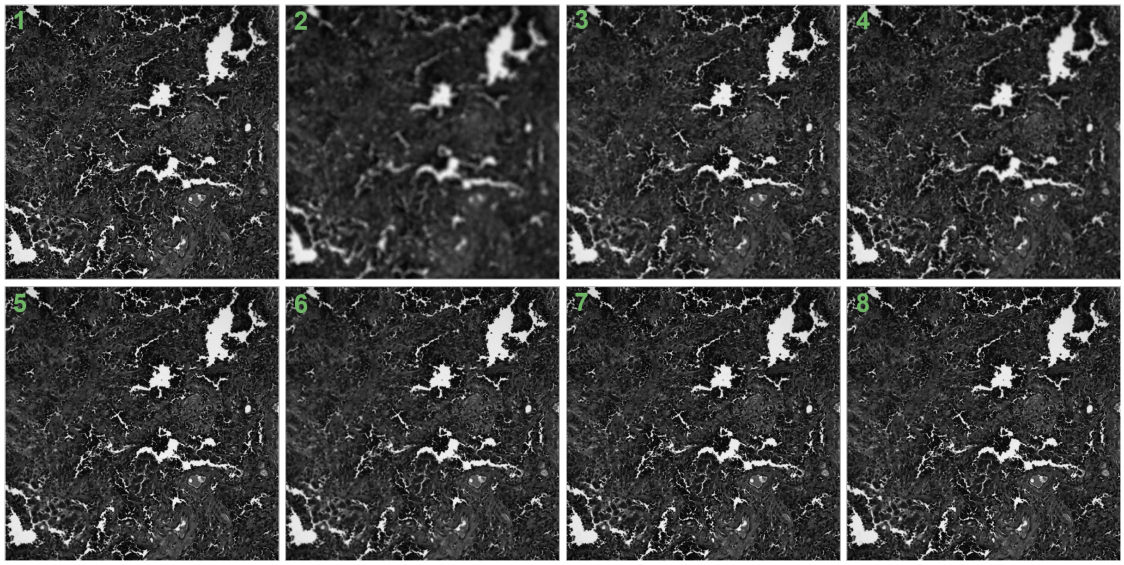

Figure S39: An example of 8 experimentally captured images using focus metric golden search within a range of ±30 µm. The numbers in the figure correspond to the image sequence.

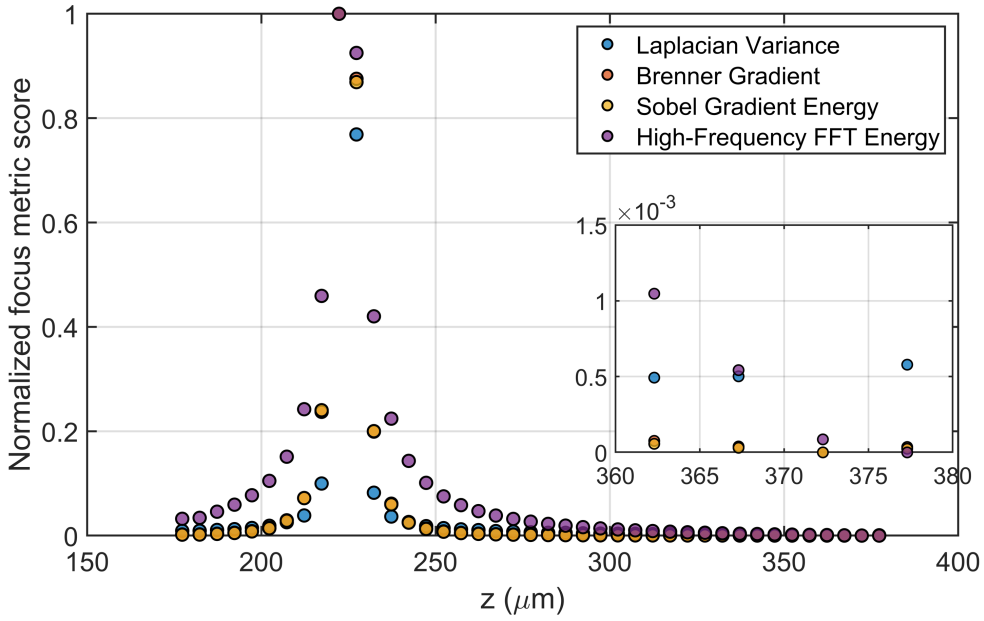

Figure S40: An example of invalid monotonicity of focus metric on either side of the focal plane.

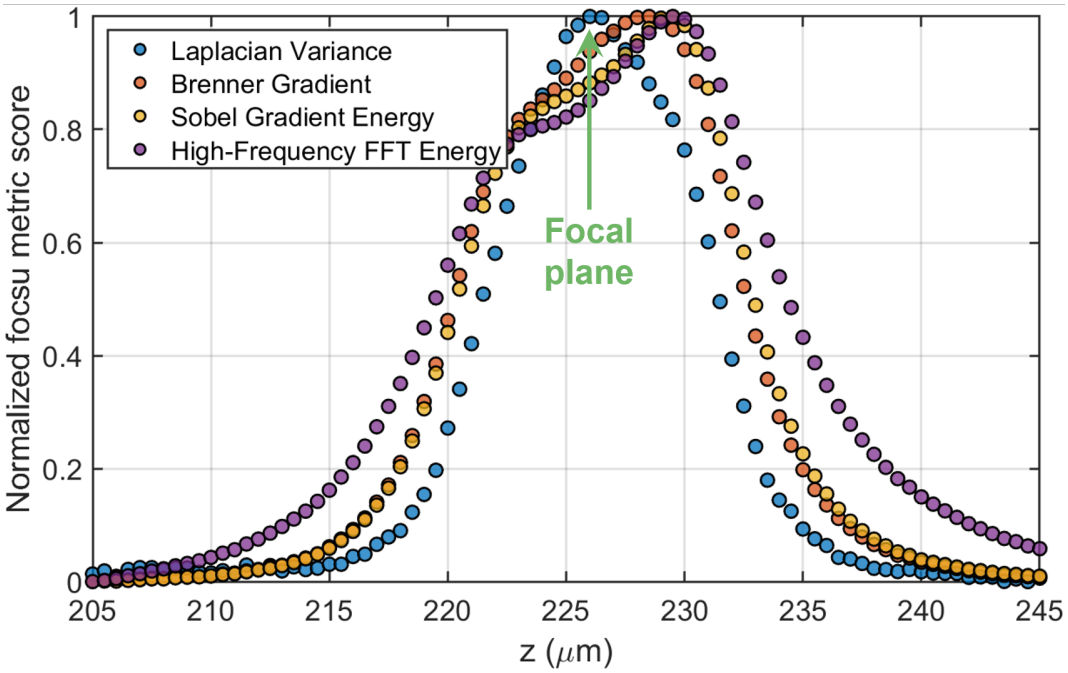

Figure S41: An example of focus metrics for finding the focal plane of an unstained human pathology tissue sample.

9.6 Beam splitter array methods

Beam splitter array-based methods [37, 38] employ a 45-degree semireflective beam splitter array to divide the incoming light path and direct it toward different regions of a focusing sensor, enabling simultaneous image acquisition across multiple axial planes. These multi-plane images are then processed using focus metrics and curve-fitting models to achieve accurate image-based autofocusing, following a principle similar to focus metric methods.

The beam splitter array methods demand additional beam-splitting optical designs, which compromise photon efficiency and introduce increased system complexity. The intricate optical architecture also poses challenges for integration into diverse imaging modalities and system configurations. Moreover, its autofocusing range is inherently limited by the finite area of the focusing sensor. Like focus metric methods, this approach is also ineffective for transparent or thick samples.

9.7 Triangulation methods

Triangulation methods [39–42] are active autofocus techniques that translate axial defocus into a measurable lateral displacement. They illuminate the coverslip–sample interface with a thin, line-shaped near-infrared beam delivered at an oblique angle. When the interface moves axially away from the nominal focal plane, the reflected beam strikes the sensor at a laterally shifted position that scales linearly with the defocus distance, enabling the system to quantify the defocus distance.

Compared to DAbI, this type of method requires complex illumination and detection optics, making the system highly intricate. It is limited to specific sample formats, such as live cells housed in imaging chambers with standard coverslips, and is not compatible with conventional microscope slides or thick plastic dishes.

9.8 Low-coherence interferometry methods

The low-coherence interferometry methods [43, 44] employ a Fourier-domain optical coherence tomography (OCT) setup as an auxiliary optical path for autofocusing. The sample is illuminated at an oblique angle using a broadband low-coherence light source, and its axial depth reflectivity profile (A-scan) is acquired

based on Fourier-domain OCT principles. The recovered profile is then analyzed to determine the in-focus position.

Compared to DAbI, this type of method requires highly specialized and complex optical designs for both illumination and detection, which significantly increases system complexity and alignment difficulty. As a result, it is generally less favorable than DAbI in terms of system simplicity and photon efficiency. Furthermore, this approach typically detects only the reference plane instead of locating the actual sample plane within the specimen. Consequently, it is limited to specific sample formats and incompatible with conventional microscope slides. In addition, this method may struggle with thick or highly scattering samples.

9.9 Confocal pinhole methods

The confocal pinhole method [45] is a laser-based reflective autofocusing method using confocal pinhole detection. A laser beam is expanded and focused onto the sample substrate, and the reflected light is directed through a confocal pinhole before being detected by a photodetector. The confocal pinhole serves to spatially filter out out-of-focus reflections, thus enhancing the axial resolution. By performing axial scanning, a depth-resolved reflectance intensity profile is generated, and the sample axial position can be located.

Both DAbI and the confocal pinhole method are capable of achieving high-precision autofocusing over a relatively large axial range. However, the confocal pinhole approach requires a dedicated laser-based confocal setup and depends on time-consuming axial scanning to identify the in-focus position. This added complexity makes it less favorable in terms of system simplicity, operational efficiency, and phototoxicity. Additionally, the confocal method typically detects only a predefined reference surface rather than the actual sample interface, which can lead to inaccurate focus for thick specimens.

9.10 A brief summary of DAbI

DAbI shows significant advantages in long autofocusing range, low photon budget, generalizability, versatility, and 3D capability. The potential improvement on DAbI is to push for real-time responses. In the future, the algorithm for searching fringe valleys can potentially be further improved, aiming at the millisecond-level responses.

10 Digital refocusing with Fourier ptychography

Several advanced complex-field imaging techniques, such as Annular Ptychographic Imaging with Closed-form method (APIC) [46] and Fourier Ptychographic Microscopy (FPM) [47], can digitally correct moderate system aberrations, including defocus, by recovering the pupil function from multiple measurements. Although these methods offer some degree of DoF extension beyond conventional microscopy, the digital refocusing range remains limited, hindering their utility in high-throughput and fast-imaging scenarios.

DAbI can be seamlessly integrated with these techniques to substantially extend their effective DoF and overcome this limitation. It provides a precise estimate of defocus without requiring additional measurements (for FPM and APIC). When incorporated into reconstruction workflows with moderate modifications, this defocus prior enables pre-correction of aberrations and significantly improves reconstruction fidelity—particularly under large defocus conditions. As demonstrated in the main paper, the integration of DAbI with APIC achieves a 20-fold extension of the DoF compared to conventional brightfield transmission microscopes, equivalent to a 4.8-fold improvement over APIC alone.

Here, we further demonstrate the versatility of DAbI by integrating it with another widely adopted complex-field imaging technique, FPM [48]. Figure S42 shows the experimental results of a standard USAF1951 phase resolution target acquired using FPM, with and without DAbI, across a range of defocus distances. For this experiment, we used an annular-illumination FPM setup [49], which captured 24 brightfield measurements from 24 NA-matching illumination angles. DAbI estimates the defocus distance directly from two alternate raw intensity measurements, which is then incorporated into a digital refocusing FPM algorithm to enable accurate reconstruction under strong defocus conditions [50, 51]. With DAbI's defocus detection capability, we extended FPM's digital refocusing ability by a factor of 7.2, representing a 15-fold increase of effective DoF over conventional bright-field or phase-contrast microscopy.

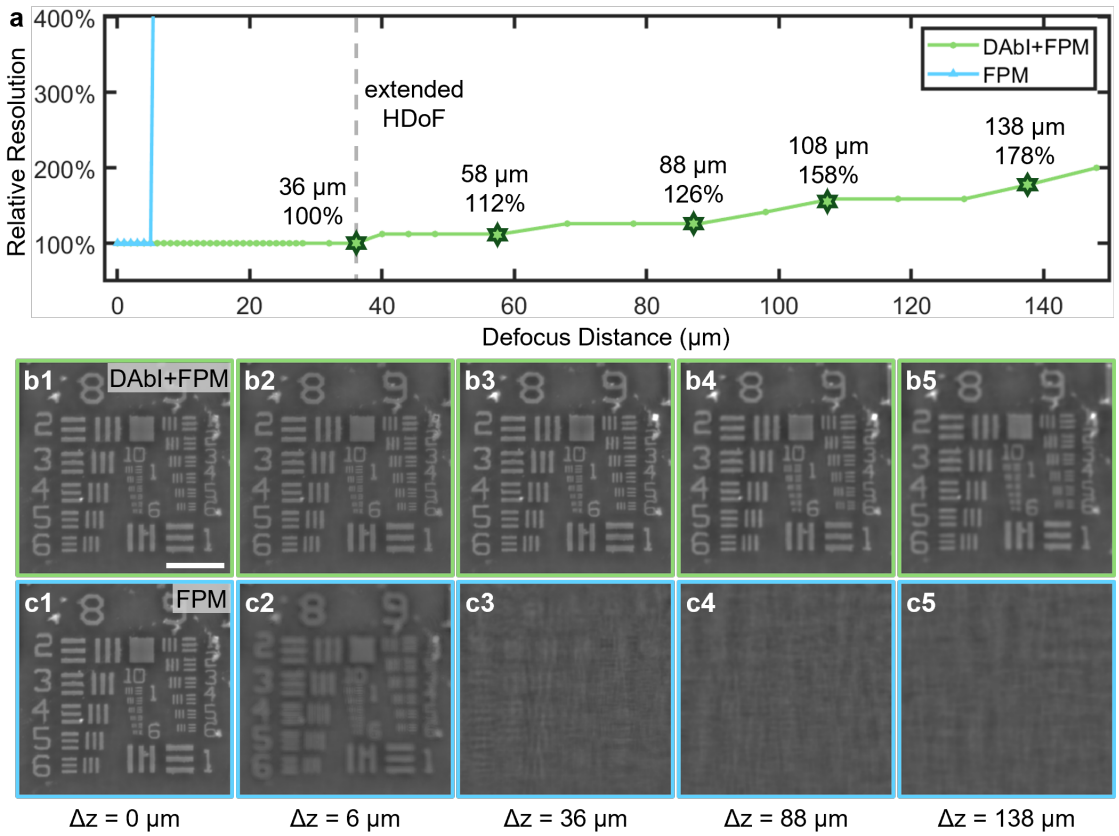

Figure S42: Experimental evaluation of digital refocusing using FPM with DAbI. **a**, Performance evaluation of digital refocusing with only FPM and DAbI-assisted FPM. **b1-5**, Zoom-in of reconstructions of USAF1951 phase targe using DAbI-assisted FPM at different defocus distances.**c1-5**, Zoom-in of reconstructions of USAF1951 phase target only using FPM. HDoF: Half DoF. Scale bar: 20 μm.

11 Comparison between digital refocusing and mechanical refocusing

In this section, we present an experiment that directly compares digitally refocused reconstructions from DAbI-assisted APIC [46], against reconstructions obtained from mechanically refocused, in-focus measurements. This experiment quantifies how accurately DAbI-assisted APIC is in digital refocusing to recover in-focus absorption/phase information from defocused acquisitions.

We collected multiple FOVs from both H&E-stained and unstained human lung cancer tissue slides. For each FOV, the sample was first intentionally positioned at a known defocus distance relative to the nominal focal plane, followed by the APIC acquisition. For both sample types, we only used the green LEDs.

Using the defocused measurements, we reconstructed the in-focus complex field via DAbI-assisted APIC. For the H&E-stained slides, we report the reconstructed amplitude images, which predominantly reflect absorption in the green channel. For the unstained slides, we report quantitative phase reconstructions.

As a reference for real refocusing, we then mechanically refocused the microscope to the true in-focus position and reconstructed the corresponding in-focus measurement using APIC alone. These mechanically refocused reconstructions serve as the ground-truth baseline for evaluating the fidelity of the digitally refocused results.

We quantified the agreement between digital and mechanical refocusing using standard image quality metrics. For the H&E absorption (amplitude) images, we used the Structural Similarity Index Measure (SSIM) and the Peak Signal-to-Noise Ratio (PSNR). For the quantitative phase images, we used the Root Mean Square Error (RMSE), since it directly measures deviations in the physical phase values rather than perceptual similarity.

The results are summarized in Fig. S43. The left panel compares absorption reconstructions, and the right panel compares quantitative phase reconstructions, across multiple FOVs and defocus distances, with the corresponding evaluation metrics reported in each panel. Overall, the digitally refocused reconstructions closely match the mechanically refocused baselines over the tested defocus range, achieving SSIM > 0.89 for absorption images and RMSE < 0.09 rad for phase images. These results demonstrate that the proposed DAbI-assisted APIC pipeline enables accurate digital refocusing with performance comparable to true mechanical refocusing, supporting the precision and reliability of the refocusing-based reconstructions presented in Fig. 8 in the main paper.

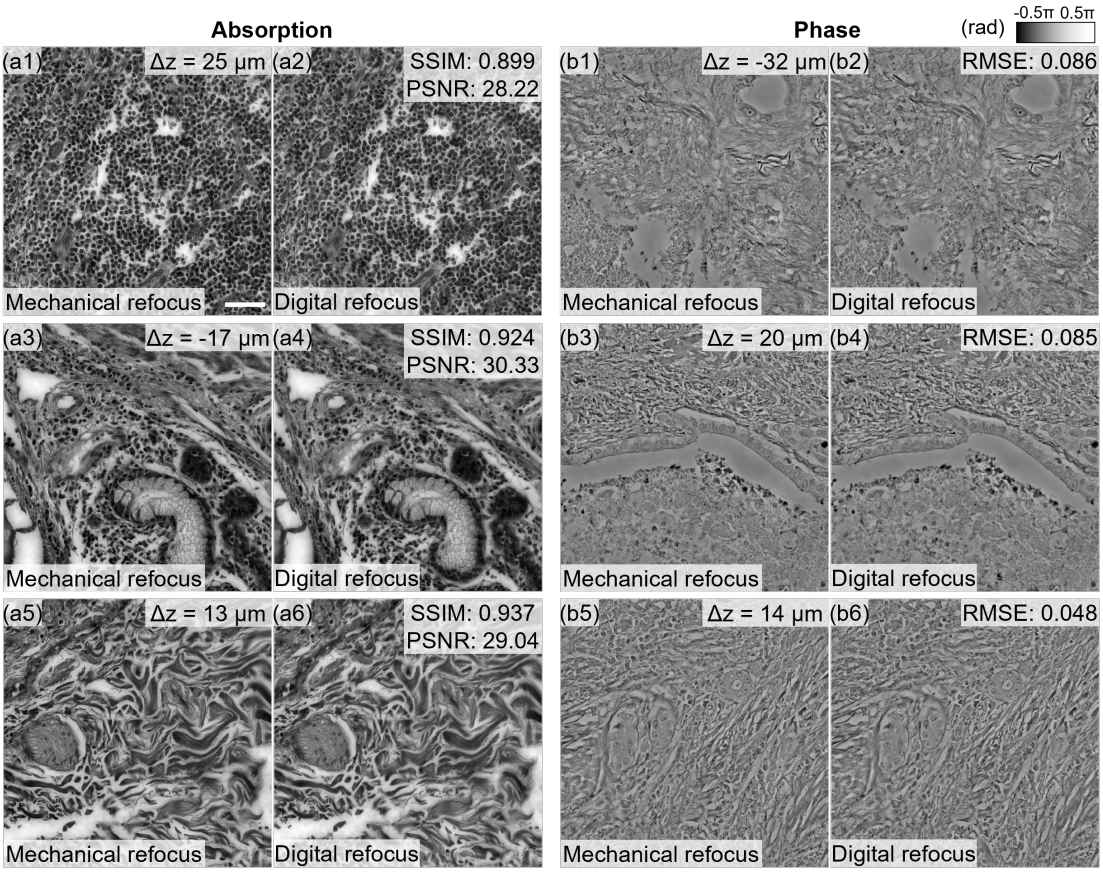

Figure S43: Mechanical refocusing versus DAbI-assisted digital refocusing with APIC. (**a1,a3,a5**) Amplitude (absorption in the green channel) reconstructed by APIC from mechanically refocused in-focus measurements of an H&E-stained NSCLC tissue section. The axial refocusing distance Δz is annotated in the top left corner. (**a2,a4,a6**) Corresponding digitally refocused amplitude reconstructed from a single defocused acquisition using DAbI-assisted APIC for the same FOVs. The Structural Similarity Index Measure (SSIM) and Peak Signal-to-Noise Ratio (PSNR) between digital and mechanical refocusing are reported in each panel. (**b1,b3,b5**) Quantitative phase reconstructed by APIC from mechanically refocused in-focus measurements of an unstained NSCLC tissue section, with Δz annotated. (**b2,b4,b6**) Corresponding digitally refocused phase reconstructed from the defocused acquisition using DAbI-assisted APIC. The Root Mean Square Error (RMSE, rad) between digitally refocused phase and the mechanically refocused baseline is reported in each panel. Scale bar: 50 μm.

12 Runtime scaling of DAbI

We benchmark the runtime scaling of the proposed DAbI algorithm on a CPU (Intel i7-14700KF) and a GPU (NVIDIA GeForce RTX 4090) across a range of input image sizes. The input images have side lengths ranging from 512 to 2048 pixels, with a step size of 256. For each image size, DAbI is executed 10 times on both CPU and GPU using multiple defocus distances and sample types, and the mean processing time and standard deviation are reported.

The results are summarized in Fig. S44. As the image size increases, the processing time of DAbI approximately follows an $\mathcal{O}(N \log N)$ scaling behavior, where N denotes the total number of pixels.

Overall, DAbI typically executes in $< 0.6\,\mathrm{s}$ on CPU and $< 0.15\,\mathrm{s}$ on GPU, demonstrating the computational efficiency of the proposed algorithm and highlighting its suitability for real-time autofocusing applications.

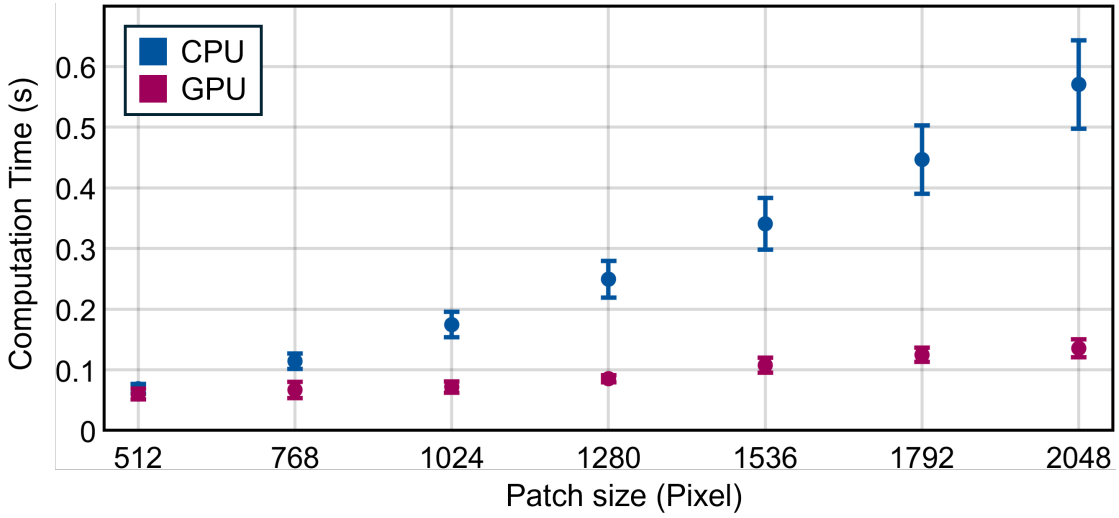

Figure S44: Runtime scaling of DAbI on CPU and GPU using experimental data. Blue and red circles denote the mean DAbI processing time over 10 repetitions across different samples and defocus distances on the CPU and GPU, respectively; error bars indicate standard deviation.

13 Additional experiments

In this section, we present additional experimental results.

13.1 Additional results for live mouse embryo imaging with DAbI

In the main paper, we have shown that DAbI facilitates automatic volumetric multi-well imaging. DAbI can eliminate the need for manual focusing when positioning the sample to a different well. Here, we showed additional results on this appealing application in Fig. S45.

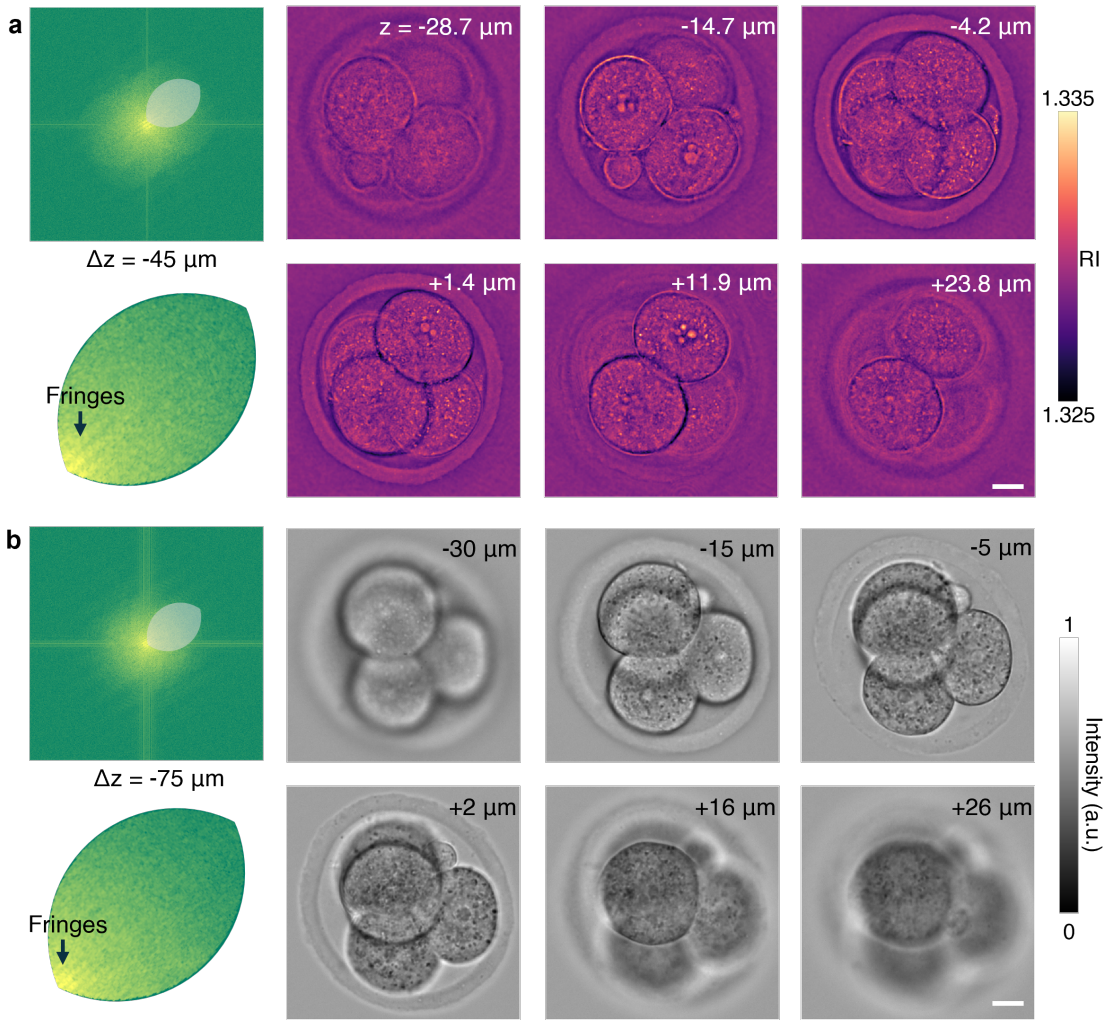

Figure S45: Experiments on multi-well live mouse embryo imaging with **a**, angular Fourier ptychotomography, and **b**, brightfield transmission microscopy. DAbI fringes can be extracted for defocus estimation. Scale bar 20 µm.

13.2 DAbI chromatic aberration correction in digital pathology

In the digital refocusing application, DAbI can produce a defocus prior to reconstruction algorithms to numerically bring the image back to focus. With this concept, DAbI can also correct chromatic aberration. By applying DAbI to every color channel, the wavelength-dependent defocus distances can be retrieved. In Fig. S45, we demonstrated that the H&E-stained human lung cancer tissue imaged by complex-field imaging exhibited different defocus distances in the three color channels, $\Delta z = 19, 22, 21$ µm, respectively.

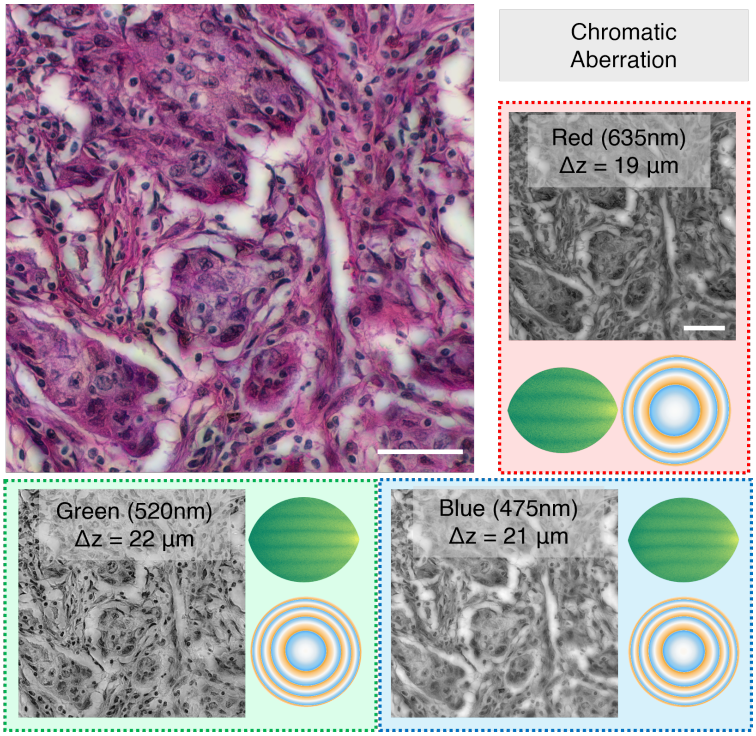

Figure S46: Experiment on H&E-stained human lung cancer imaging with DAbI applied to each color channel for chromatic aberration correction. Scale bar 50 μm.

14 Additional discussions

14.1 Adaptation to reflection-mode microscopes

Although all demonstrations in this paper and the Supplementary Notes are performed on transmission-mode optical microscopes, DAbI is equally compatible with reflection-mode microscopes. A potential system configuration for reflection-mode implementation is illustrated in Fig. S47. In this design, the illumination sources, together with an additional relay lens and a beam splitter (Lens 1 and BS in Fig. S47), provide oblique illumination delivered from the backside of the objective lens. The combination of Lens 1 and the objective forms a $4f$–system that relays the tilted illumination onto the sample plane. The scattered and unscattered light from the sample is then collected through the standard detection pathway.

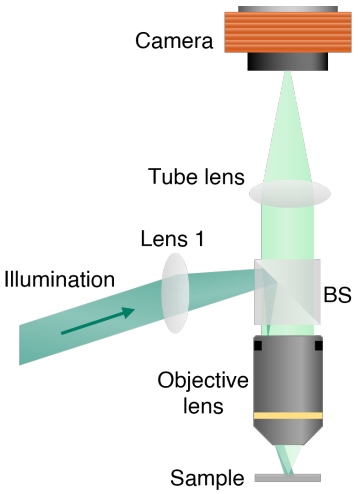

Figure S47: A potential system configuration for adapting DAbI to the reflection-mode microscopes. BS: beam splitter.

14.2 Potential reduction to a single image autofocusing

Our theoretical analyses of DAbI in Notes 1 and 2 provide a deep understanding of the defocus effect and defocus detection in a wave-optics perspective. Additionally, we have explained why two images are needed in DAbI to achieve robust defocus detection. However, some situations may need ultrafast autofocusing for mass-production inspection or parallel bio-imaging. In these situations, we may need to reduce image acquisition to a single capture. We believe

Our theoretical analyses of DAbI in Notes 1 and 2 provide a comprehensive wave-optics understanding of defocus effects and defocus detection. We have also explained why two intensity measurements are required in DAbI to achieve robust and unambiguous defocus estimation.

Nevertheless, certain applications—such as high-throughput industrial inspection and large-scale parallel biological imaging—require ultrafast autofocusing, where reducing image acquisition to a single capture may be highly desirable. In such scenarios, we believe that single-image variants of DAbI may be possible by introducing additional system constraints or priors. For example, data-driven approaches may learn to infer defocus from subtle spectral or spatial cues present in a single image.

It is important to note that these single-image strategies would likely involve trade-offs between robustness, performance, and generality compared with the two-image formulation of DAbI. Nonetheless, they may offer a favorable balance between speed and performance in throughput-limited applications. Investigating such single-shot extensions of DAbI remains an interesting direction for future work.

15 Sequence information for plasmid

15.1 rtTA plasmid sequence

ttgagatccttttttttctgcgcgtaatctgctgcttgcaaacaaaaaaaccaccgctaccagcggtggtttgtttgccggatcaagagctaccaactctttttccgaagg
taactggcttcagcagagcgcagataccaaatactgttcttctagtgtagccgtagttaggccaccacttcaagaactctgtagcaccgcctacatacctcgctctgcta
atcctgttaccagtggctgctgccagtggcgataagtcgtgtcttaccgggttggactcaagacgatagttaccggataaggcgcagcggtcgggctgaacgggggttc
gtgcacacagcccagcttggagcgaacgacctacaccgaactgagatacctacagcgtgagctatgagaaagcgccacgcttcccgaagggagaaaggcggacaggtatc
cggtaagcggcagggtcggaacaggagagcgcacgagggagcttccagggggaaacgcctggtatctttatagtcctgtcgggtttcgccacctctgacttgagcgtcga
tttttgtgatgctcgtcaggggggcggagcctatggaaaaacgccagcaacgcggccttttacggttcctggccttttgctggccttttgctcacatgtcctgcaggca
gctgcgcgctcgctcgctcactgaggccgcccgggcgtcgggcgacctttggtcgcccggcctcagtgagcgagcgagcgcgcagagagggagtggccaactccatcact
aggggttcctgcggccgcacgcgtaacactagttattaatagtaatcaattacggggtcattagttcatagcccatatatggagttccgcgttacataacttacggtaaa
tggcccgcctggctgaccgcccaacgacccccgcccattgacgtcaataatgacgtatgttcccatagtaacgccaatagggactttccattgacgtcaatgggtggagt
atttacggtaaactgcccacttggcagtacatcaagtgtatcatatgccaagtacgccccctattgacgtcaatgacggtaaatggcccgcctggcattatgcccagtac
atgaccttatgggactttcctacttggcagtacatctacgtattagtcatcgctattaccatggtcgaggtgagccccacgttctgcttcactctccccatctcccccccc
ctccccacccccaattttgtatttatttatttttttaattattttgtgcagcgatgggggcgggggggggggggggggggcgcgcgccaggcggggcggggcggggcgaggg
gcggggcggggcgaggcggagaggtgcggcggcagccaatcagagcggcgcgctccgaaagtttccttttatggcgaggcggcggcggcggcccctataaaaagcgaa
gcgcgcggcgggcgggagtcgctgcgcgctgccttcgccccgtgccccgctccgccgccgcctcgcgccgcccgccccggctctgactgaccgcgttactcccacaggtg
agcgggcgggacggcccttctcctccgggctgtaattagcgcttggtttaatgacggcttgtttcttttctgtggctgcgtgaaagccttgaggggctccgggagcgccg
gcaggaaggaaatgggcggggagggccttcgtgcgtcgccgcgccgccgtcccctttctccctctccagcctcggggctgtccgcgggggacggctgccttcgggggga
cggggcagggcggggttcggcttctggcgtgtgaccggcggctctagagcctctgctaaccatgttcatgccttcttctttttcctacagctcctgggcaacgtgctggt
tattgtgctgtctcatcattttggcaaagaattgcggcccaacggtaccgccaccatgtctaggctggacaagagcaaagtcataaacggagctctggaattactcaatg
gtgtcggtatcgaaggcctgacgacaaggaaactcgctcaaaagctgggagttgagcagcctaccctgtactggcacgtgaagaacaagcgggccctgctcgatgccctg
ccaatcgagatgctggacaggcatcatacccacttctgccccctggaaggcgagtcatggcaagactttctgcggaacaacgccaagtcataccgctgtgctctcctctc
acatcgcgacggggctaaagtgcatctcggcacccgcccaacagagaaacagtacgaaaccctggaaaatcagctcgcgttcctgtgtcagcaaggcttctccctggaga
acgcactgtacgctctgtccgccgtgggccactttacactgggctgcgtattggaggaacaggagcatcaagtagcaaaagaggaaagagagacacctaccaccgattct
atgcccccacttctgagacaagcaattgagctgttcgaccggcagggagccgaacctgccttccttttcggcctggaactaatcatatgtggcctggagaaacagctaaa
gtgcgaaagcggcgggccgaccgacgcccttgacgattttgacttagacatgctcccagccgatgcccttgacgattttgaccttgacatgctccccgggtaaaagctta
tcgataatcaacctctggattacaaaatttgtgaaagattgactggtattcttaactatgttgctccttttacgctatgtggatacgctgctttaatgcctttgtatcat
gctattgcttcccgtatggctttcattttctcctccttgtataaatcctggttgctgtctctttatgaggagttgtggcccgttgtcaggcaacgtggcgtggtgtgcac
tgtgtttgctgacgcaacccccactggttggggcattgccaccacctgtcagctcctttccgggactttcgctttcccctccctattgccacggcggaactcatcgccg
cctgccttgcccgctgctggacaggggctcggctgttgggcactgacaattccgtggtgttgtcggggaaatcatcgtccttttccttggctgctcgcctatgttgccacc
tggattctgcgcgggacgtccttctgctacgtcccttcggccctcaatccagcggaccttccttcccgcggcctgctgccggctctgcggcctcttccgcgtcttcgcct
tcgccctcagacgagtcggatctccctttgggccgcctccccgcatcgataccgagcgctgctcgagaatcggagacggtgtaatgatacgggtggcatccctgtgaccc
ctccccagtgcctctcctggccctggaagttgccactccagtgcccaccagccttgtcctaataaaattaagttgcatcattttgtctgactaggtgtccttctataata
ttatggggtggaggggggtggtatggagcaaggggcaagttgggaagacaacctgtagggcctgcggggtctattgggaaccaagctggagtgcagtggcacaatcttgg
ctcactgcaatctccgcctcctgggttcaagcgattctcctgcctcagcctcccgagttgttgggattccaggcatgcatgaccaggctcagctaatttttgttttttg
gtagagacggggtttcaccatattggccaggctggtctccaactcctaatctcaggtgatctacccaccttggcctcccaaattgctgggattacaggcgtgaaccactg
ctcccttccctgtccttctgattttgtaggtaaccaccgacagcttgtctctccagatgctcttgggccatcttccacatcgtccgtagcagccttggcaatttgccatc
actggcaaatacacataaatccaatgaatacggttaccaccatcacattaccatgcaggtacacagcaagaattgacgttggcatatcacatggtgtaataaccccactt
gtgaaacaacccagaataaggtacaaggcggaaatgtcgtcattctaaaataaaaggcatggccaggaatttgtctaatacccgggaacttaaattcagcttgaacaccag
tcgcaaaaaattcaaagaaagtgattcaggttcgggttcgtggattggaacagcttcttttgtttcagtgatgagagaatcctcctgtcaccctttagtgagggttaatt
ctcgagtctccctatagtgagtcgtattaattccgtgcggaccgagcggccgcaggaacccctagtgatggagttggccactccctctctgcgcgctcgctcgctcactg
aggccgggcgaccaaaggtcgcccgacgcccgggctttgcccgggcggcctcagtgagcgagcgagcgcgcagctgcctgcaggggcgcctgatgcggtattttctcctt
acgcatctgtgcggtatttcacaccgcatacgtcaaagcaaccatagtacgcgccctgtagcggcgcattaagcgcggcgggtgtggtggttacgcgcagcgtgaccgct
acacttgccagcgccttagcgcccgctcctttcgctttcttcccttcctttctcgccacgttcgccggctttccccgtcaagctctaaatcgggggctccctttagggtt
ccgatttagtgctttacggcacctcgaccccaaaaaacttgatttgggtgatggttcacgtagtgggccatcgccctgatagacggtttttcgccctttgacgttggagt
ccacgttctttaatagtggactcttgttccaaactggaacaacactcaactctatctcgggctattcttttgatttataagggattttgccgatttcggtctattggtta
aaaaatgagctgatttaacaaaaatttaacgcgaatttaacaaaatattaacgtttacaattttatggtgcactctcagtacaatctgctctgatgccgcatagttaag
ccagccccgacacccgccaacacccgctgacgcgccctgacgggcttgtctgctcccggcatccgcttacagacaagctgtgaccgtctccgggagctgcatgtgtcaga
ggttttcaccgtcatcaccgaaacgcgcgagacgaaagggcctcgtgatacgcctatttttataggttaatgtcatgataataatggtttcttagacgtcaggtggcact
tttcggggaaatgtgcgcggaaccccctatttgtttatttttctaaatacattcaaatatgtatccgctcatgagacaataaccctgataaatgcttcaataatattgaaa
aaggaagagtatgagtattcaacatttccgtgtcgcccttattcccttttttgcggcattttgccttcctgtttttgctcacccagaaacgctggtgaaagtaaaagatg
ctgaagatcagttgggtgcacgagtgggttacatcgaactggatctcaacagcggtaagatccttgagagttttcgccccgaagaacgtttccaatgatgagcactttt
aaagttctgctatgtggcgcggtattatcccgtattgacgccgggcaagagcaactcggtcgccgcatacactattctcagaatgacttggttgagtactcaccagtcac
agaaaagcatcttacggatggcatgacagtaagagaattatgcagtgctgccataaccatgagtgataacactgcggccaacttacttctgacaacgatcggaggaccga

aggagctaaccgctttttttgcacaacatgggggatcatgtaactcgccttgatcgttgggaaccggagctgaatgaagccataccaaacgacgagcgtgacaccacgatg
cctgtagcaatggcaacaacgttgcgcaaactattaactggcgaactacttactctagcttcccggcaacaattaatagactggatggaggcggataaagttgcaggacc
acttctgcgctcggcccttccggctggctggtttattgctgataaatctggagccggtgagcgtgggtctcgcggtatcattgcagcactggggccagatggtaagccct
cccgtatcgtagttatctacacgacggggagtcaggcaactatggatgaacgaaatagacagatcgctgagataggtgcctcactgattaagcattggtaactgtcagac
caagtttactcatatatactttagattgatttaaaacttcatttttaatttaaaaggatctaggtgaagatccttttgataatctcatgaccaaaatcccttaacgtga
gttttcgttccactgagcgtcagaccccgtagaaaagatcaaaggatcttc

15.2 Self-assembling α-synuclein plasmid sequence

ttgagatccttttttttctgcgcgtaatctgctgcttgcaaacaaaaaaaccaccgctaccagcggtggtttgtttgccggatcaagagctaccaactctttttccgaagg
taactggcttcagcagagcgcagataccaaatactgttcttctagtgtagccgtagttaggccaccacttcaagaactctgtagcaccgcctacatacctcgctctgcta
atcctgttaccagtggctgctgccagtggcgataagtcgtgtcttaccgggttggactcaagacgatagttaccggataaggcgcagcggtcgggctgaacgggggttc
gtgcacacagcccagcttggagcgaacgacctacaccgaactgagatacctacagcgtgagctatgagaaagcgccacgcttcccgaagggagaaaggcggacaggtatc
cggtaagcggcagggtcggaacaggagagcgcacgagggagcttccagggggaaacgcctggtatctttatagtcctgtcgggtttcgccacctctgacttgagcgtcga
tttttgtgatgctcgtcaggggggcggagcctatggaaaaacgccagcaacgcggccttttacggttcctggccttttgctggccttttgctcacatgtcctgcaggca
gctgcgcgctcgctcgctcactgaggccgcccgggcgtcgggcgacctttggtcgcccggcctcagtgagcgagcgagcgcgcagagagggagtggccaactccatcact
aggggttcctgcggccgcacgcgtatcaagtgccacctgacgtctccctatcagtgatagagaagtcgacacgtctcgagctccctatcagtgatagagaagGtacgtct
agaacgtctccctatcagtgatagagaagtcgacacgtctcgagctccctatcagtgatagagaaggtacgtctagaacgtctccctatcagtgatagagaagtcgacac
gtctcgagctccctatcagtgatagagaaggtacgtctagaacgtctccctatcagtgatagagaagtcgacacgtctcgagctccctatcagtgatagagaagctaccc
cctatataagcagagctcgtttagtgaaccgtcagatcgcctggagacgccatccacgctgttttgacctccatagaagacaccgggaccgatccagcctggatccggta
ccgccaccatggatgttttcatgaagggcctcagtaaggcaaaagaaggtgtggtcgccgctgccgaaaagaccaagcaaggcgttgcggaggccgcagggaagactaaa
gagggggtgttgtacgtcgggtctaagacaaaggaggggtcgtacacggtgtggcgactgtagccgaaaaaacgaaagaacaagtcaccaatgtcggcggcgctgttgt
cactggtgttacagcggtagcgcaaaagaccgtcgagggtgcggggtcaatagcggctgcgacagggttcgtaaaaaaggaccagcttggcaagaacgaggaaggcgccc
cccaggaaggcatactggaagatatgcccgtcgaccctgataacgaggcgtatgagatgccaagtgaagaaggttaccaagactatgagcccgaggcaggaggggggagc
ggaggtaccgggggattgactatactgctgctggtttcaccctcctccaaggtgcacatctgtacgctcctgaagacagaggtatctgcgatgtgctggttgccaacgg
taagatcatcgctgtggcctccaacattcctagcgacatcgttccaaactgcaccgttgtcgatctgagcggacagatcctctgtccaggattcattgatcagcacgtgc
acctcattggaggaggaggcgaagctggtcctactactagaactcccgaagtcgcactgtctcgcctcacagaggcaggcgttacctccgtcgtgggactcctgggtact
gatagcatctctaggcaccctgagtctctgctggcaaagaccagagccctcaatgaggagggtatctccgcttggatgctgactggtgcttatcacgtcccatctcgcac
cattactggcagcgtggagaaggacgttgcaatcatcgacagagtgatcggtgttaagtgcgctatctccgaccacaggagcgctgctcccgacgtctatcacctggcca
acatggcagccgagagcagagtcggtggtctgctcggtggcaagccaggagttaccgtgttccacatgggtgactctaagaaggcactgcaacccatctatgacctgctg
gagaactgtgacgtcccaatctccaagctgctgcctacccacgtcaacaggaacgtgcctctcttctaccaagctctggagttcgcaagaaagggtggcaccatcgacat
cacctctagcattgatgaacccgtcgctccagctgagggaatcgcaagggctgtccaagcaggtatcccactggcaagggtgacactcagctctgatggcaacggctccc
agccattcttcgatgatgaaggaaatctgactcacattggcgtggctggatttgaaactctcctggaaacagttcaggttctggttaaggactacgacttcagcatttct
gacgctctcagaccactcacctctagcgtcgctggcttcctgaacctgactggtaaaggcgaaatcctccctggtaatgacgctgatctgctggtgatgacacccgaact
gcgcattgagcaggtctatgcaagaggaaagctgatggttaaggacggaaaggcttgtgtcaagggcacattcgagactgctggtggctctggaggcaccggagggtctg
gagggactggaggctctggaggtactggcggttctggaggtaccggtggtaagcctatccctaaccctctgctcggtctcgattctaccggatccggtaagattgaagag
ggcaaactggttatctggatcaatggcgataagggctacaatggcctggcagaggtcggtaagaagttcgagaaagatacaggcatcaaagttactgtggaacacccaga
taagctggaggagaagttccctcaggtcgcagcaactggcgacggtccagacatcatcttctgggcacacgataggttcggtggctatgcccaatctggcctgctggctg
agattactcctgataaggctttccaggacaagctgtatccattcacctgggatgctgtgagatacaatggcaagctgatcgcataccctattgctgtggaagctctgagc
ctgatctacaacaaggacctgctgcctaatcctcctaagacatgggaagaaatccctgcactggacaaggaactgaaggccaaaggcaagtccgcactgatgttcaacct
gcaggagccttactttacctggccactgattgctgccgacggtggttacgctttcaagtacgagaatggtaagtacgacatcaaagatgtgggtgtggacaatgctggtg
ccaaagctggtctgactttcctggtggatctgatcaagaacaagcacatgaatgcagacactgactattctatcgcagaggctgctttcaacaaaggcgaaaccgcaatg
actatcaatggtccttgggcatggtctaacatcgacactagcaaagtcaactacggtgtcaccgttctgccaaccttcaagggtcagccaagcaaacctttcgttggcgt
gctgagcgcaggtatcaacgctgcctctcctaacaaagagctggctaaggagtttctggagaactacctgctgacagacgaaggtctggaggcagtgaacaaggacaagc
cactgggtgccgtggctctgaagagctacgaagaagaactggccaaggaccctcgcatcgctgctacaatggagaacgcacagaagggtgagatcatgccaaacatccca
cagatgagcgcattctggtatgccgtgaggaccgctgttatcaacgcagcttctggcagacagaccgtggatgaagccctgaaagacgcacagacctgagaattcgatat
caagcttatcgataatcaacctctggattacaaaatttgtgaaagattgactggtattcttaactatgttgctccttttacgctatgtggatacgctgctttaatgcctt
tgtatcatgctattgcttcccgtatggctttcattttctcctccttgtataaatcctggttgctgtctctttatgaggagttgtggcccgttgtcaggcaacgtggcgtg
gtgtgcactgtgtttgctgacgcaacccccactggttggggcattgccaccacctgtcagctcctttccgggactttcgctttcccctccctattgccacggcggaact
catcgccgcctgccttgcccgctgctggacaggggctcggctgttgggcactgacaattccgtggtgttgtcggggaaatcatcgtcctttccttggctgctcgcctatg
ttgccacctggattctgcgcgggacgtccttctgctacgtcccttcggccctcaatccagcggaccttccttcccgcggcctgctgccggctctgcggcctcttccgcgt
cttcgccttcgccctcagacgagtcggatctccctttgggccgcctccccgcatcgataccgagcgctgctcgagagatctacgggtggcatccctgtgacccctcccca
gtgcctctcctggccctggaagttgccactccagtgcccaccagccttgtcctaataaaattaagttgcatcattttgtctgactaggtgtccttctataatattatggg
gtggaggggggtggtatggagcaaggggcaagttgggaagacaacctgtagggcctgcggggtctattgggaaccaagctggagtgcagtggcacaatcttggctcactg
caatctccgcctcctgggttcaagcgattctcctgcctcagcctcccgagttgttgggattccaggcatgcatgaccaggctcagctaatttttgttttttttggtagaga

cggggtttcaccatattggccaggctggtctccaactcctaatctcaggtgatctacccaccttggcctcccaaattgctgggattacaggcgtgaaccactgctccctt
ccctgtccttctgattttgtaggtaaccacgtgcggaccgagcggccgcaggaacccctagtgatggagttggccactccctctctgcgcgctcgctcgctcactgaggc
cgggcgaccaaaggtcgcccgacgcccgggctttgcccgggcggcctcagtgagcgagcgagcgcgcagctgcctgcaggggcgcctgatgcggtattttctccttacgc
atctgtgcggtatttcacaccgcatacgtcaaagcaaccatagtacgcgccctgtagcggcgcattaagcgcggcgggtgtggtggttacgcgcagcgtgaccgctacac
ttgccagcgccttagcgcccgctcctttcgctttcttcccttcctttctcgccacgttcgccggctttccccgtcaagctctaaatcgggggctccctttagggttccga
tttagtgctttacggcacctcgaccccaaaaaacttgatttgggtgatggttcacgtagtgggccatcgccctgatagacggtttttcgccctttgacgttggagtccac
gttctttaatagtggactcttgttccaaactggaacaacactcaactctatctcgggctattcttttgatttataagggattttgccgatttcggtctattggttaaaaa
atgagctgatttaacaaaaatttaacgcgaattttaacaaaatattaacgtttacaattttatggtgcactctcagtacaatctgctctgatgccgcatagttaagccag
ccccgacacccgccaacacccgctgacgcgccctgacgggcttgtctgctcccggcatccgcttacagacaagctgtgaccgtctccgggagctgcatgtgtcagaggtt
ttcaccgtcatcaccgaaacgcgcgagacgaaagggcctcgtgatacgcctatttttataggttaatgtcatgataataatggtttcttagacgtcaggtggcacttttc
ggggaaatgtgcgcggaacccctatttgtttatttttctaaatacattcaaatatgtatccgctcatgagacaataaccctgataaatgcttcaataatattgaaaaagg
aagagtatgagtattcaacatttccgtgtcgcccttattcccttttttgcggcattttgccttcctgtttttgctcacccagaaacgctggtgaaagtaaaagatgctga
agatcagttgggtgcacgagtgggttacatcgaactggatctcaacagcggtaagatccttgagagttttcgccccgaagaacgttttccaatgatgagcacttttaaag
ttctgctatgtggcgcggtattatcccgtattgacgccgggcaagagcaactcggtcgccgcatacactattctcagaatgacttggttgagtactcaccagtcacagaa
aagcatcttacggatggcatgacagtaagagaattatgcagtgctgccataaccatgagtgataacactgcggccaacttacttctgacaacgatcggaggaccgaagga
gctaaccgcttttttgcacaacatgggggatcatgtaactcgccttgatcgttgggaaccggagctgaatgaagccataccaaacgacgagcgtgacaccacgatgcctg
tagcaatggcaacaacgttgcgcaaactattaactggcgaactacttactctagcttcccggcaacaattaatagactggatggaggcggataaagttgcaggaccactt
ctgcgctcggcccttccggctggctggtttattgctgataaatctggagccggtgagcgtgggtctcgcggtatcattgcagcactggggccagatggtaagccctcccg
tatcgtagttatctacacgacggggagtcaggcaactatggatgaacgaaatagacagatcgctgagataggtgcctcactgattaagcattggtaactgtcagaccaag
tttactcatatatactttagattgatttaaaacttcatttttaatttaaaaggatctaggtgaagatccttttgataatctcatgaccaaaatcccttaacgtgagttt
tcgttccactgagcgtcagaccccgtagaaaagatcaaaggatcttc

16 Supplementary video information

Supplementary Video 1: This video includes animations for demonstrating autofocusing and digital refocusing with DAbI.

References

1. Born, M. & Wolf, E. *Principles of optics: electromagnetic theory of propagation, interference and diffraction of light* (Elsevier, 2013).
2. Dong, Z. *et al.* Analytic Fourier ptychotomography for aberration-free and high-resolution volumetric refractive index imaging. *Nature Communications* **17** (2026).
3. Arfken, G. B., Weber, H. J. & Harris, F. E. *Mathematical Methods for Physicists* 7th. ISBN: 978-0-12-384654-9 (Academic Press, Boston, 2012).
4. Zuo, C., Sun, J., Li, J., Asundi, A. & Chen, Q. Wide-field high-resolution 3D microscopy with Fourier ptychographic diffraction tomography. *Optics and Lasers in Engineering* **128,** 106003 (2020).
5. Nyquist, H. Certain topics in telegraph transmission theory. *Transactions of the American Institute of Electrical Engineers* **47,** 617–644 (1928).
6. Zhang, O. *et al.* Investigating 3D microbial community dynamics of the rhizosphere using quantitative phase and fluorescence microscopy. *Proceedings of the National Academy of Sciences* **121,** e2403122121 (2024).
7. Holme, B. *et al.* Automated tracking of cell migration in phase contrast images with CellTraxx. *Scientific Reports* **13,** 22982 (2023).
8. van der Schaaf, A. & van Hateren, J. Modelling the Power Spectra of Natural Images: Statistics and Information. *Vision Research* **36,** 2759–2770. ISSN: 0042-6989. https://www.sciencedirect.com/science/article/pii/0042698996000028 (1996).
9. Bian, Z. *et al.* Autofocusing technologies for whole slide imaging and automated microscopy. *Journal of Biophotonics* **13,** e202000227 (2020).
10. Liao, J. *et al.* Dual light-emitting diode-based multichannel microscopy for whole-slide multiplane, multispectral and phase imaging. *Journal of Biophotonics* **11,** e201700075 (2018).
11. Liao, J. *et al.* Rapid focus map surveying for whole slide imaging with continuous sample motion. *Optics Letters* **42,** 3379–3382 (2017).
12. Guo, C. *et al.* OpenWSI: a low-cost, high-throughput whole slide imaging system via single-frame autofocusing and open-source hardware. *Optics Letters* **45,** 260–263 (2020).
13. Yu, C., Ding, F., Ma, Z. & Tang, Y. *Rapid Autofocus Method Based on LED Oblique Illumination for Metaphase Chromosome Microscopy Imaging System* in *Photonics* **11** (2024), 1091.
14. Brenner, J. F. *et al.* An automated microscope for cytologic research: a preliminary evaluation. *Journal of Histochemistry & Cytochemistry* **24,** 100–111 (1976).
15. Yeo, T., Ong, S., Sinniah, R., *et al.* Autofocusing for tissue microscopy. *Image and Vision Computing* **11,** 629–639 (1993).
16. Groen, F. C., Young, I. T. & Ligthart, G. A comparison of different focus functions for use in autofocus algorithms. *Cytometry: The Journal of the International Society for Analytical Cytology* **6,** 81–91 (1985).
17. Redondo, R. *et al.* Autofocus evaluation for brightfield microscopy pathology. *Journal of Biomedical Optics* **17,** 036008–036008 (2012).
18. Press, W. H., Teukolsky, S. A., Vetterling, W. T. & Flannery, B. P. Numerical recipes 3rd edition. *Cambridge: New York* (2007).
19. Dong, R.-T., Rashid, U. & Zeineh, J. *System and method for generating digital images of a microscope slide* US Patent App. 10/897,941. Apr. 2005.
20. Hulsken, B. & Stallinga, S. *Sensor for microscopy* US Patent 10,353,190. July 2019.
21. Zou, Y., Crandall, G. J. & Olson, A. *Real-time focusing in line scan imaging* US Patent 9,841,590. Dec. 2017.
22. Pinkard, H., Phillips, Z., Babakhani, A., Fletcher, D. A. & Waller, L. Deep learning for single-shot autofocus microscopy. *Optica* **6,** 794–797 (2019).
23. Jiang, S. *et al.* Transform-and multi-domain deep learning for single-frame rapid autofocusing in whole slide imaging. *Biomedical Optics Express* **9,** 1601–1612 (2018).

24. Ren, Z., Xu, Z. & Lam, E. Y. Learning-based nonparametric autofocusing for digital holography. *Optica* **5,** 337–344 (2018).

25. Wei, L. & Roberts, E. Neural network control of focal position during time-lapse microscopy of cells. *Scientific Reports* **8,** 7313 (2018).

26. Kohlberger, T. *et al.* Whole-slide image focus quality: Automatic assessment and impact on ai cancer detection. *Journal of Pathology Informatics* **10,** 39 (2019).

27. Campanella, G. *et al.* Towards machine learned quality control: A benchmark for sharpness quantification in digital pathology. *Computerized Medical Imaging and Graphics* **65,** 142–151 (2018).

28. Yang, S. J. *et al.* Assessing microscope image focus quality with deep learning. *BMC Bioinformatics* **19,** 77 (2018).

29. Luo, Y., Huang, L., Rivenson, Y. & Ozcan, A. Single-shot autofocusing of microscopy images using deep learning. *ACS Photonics* **8,** 625–638 (2021).

30. De Haan, K., Rivenson, Y., Wu, Y. & Ozcan, A. Deep-learning-based image reconstruction and enhancement in optical microscopy. *Proceedings of the IEEE* **108,** 30–50 (2019).

31. Wu, Y. *et al.* Extended depth-of-field in holographic imaging using deep-learning-based autofocusing and phase recovery. *Optica* **5,** 704–710 (2018).

32. Li, Q. *et al.* Learning to autofocus in whole slide imaging via physics-guided deep cascade networks. *Optics Express* **30,** 14319–14340 (2022).

33. Kinba, A., Hamada, M., Ueda, H., Sugitani, K. & Ootsuka, H. *Auto focus detecting device comprising both phase-difference detecting and contrast detecting methods* US Patent 5,597,999. Jan. 1997.

34. Guo, K., Liao, J., Bian, Z., Heng, X. & Zheng, G. InstantScope: a low-cost whole slide imaging system with instant focal plane detection. *Biomedical Optics Express* **6,** 3210–3216 (2015).

35. Liao, J. *et al.* Single-frame rapid autofocusing for brightfield and fluorescence whole slide imaging. *Biomedical Optics Express* **7,** 4763–4768 (2016).

36. Silvestri, L. *et al.* Universal autofocus for quantitative volumetric microscopy of whole mouse brains. *Nature Methods* **18,** 953–958 (2021).

37. Virág, T., László, A., Molnár, B., Tagscherer, A. & Varga, V. S. *Focusing method for the high-speed digitalisation of microscope slides and slide displacing device, focusing optics, and optical rangefinder* US Patent 7,663,078. Feb. 2010.

38. Montalto, M. C., McKay, R. R. & Filkins, R. J. Autofocus methods of whole slide imaging systems and the introduction of a second-generation independent dual sensor scanning method. *Journal of Pathology Informatics* **2,** 44 (2011).

39. Reinheimer, G. *Arrangement for automatically focusing an optical instrument* US Patent 3,721,827. Mar. 1973.

40. Liu, C.-S. & Jiang, S.-H. Precise autofocusing microscope with rapid response. *Optics and Lasers in Engineering* **66,** 294–300 (2015).

41. Liu, C.-S., Wang, Z.-Y. & Chang, Y.-C. Design and characterization of high-performance autofocusing microscope with zoom in/out functions. *Applied Physics B* **121,** 69–80 (2015).

42. Li, Q., Bai, L., Xue, S. & Chen, L. Autofocus system for microscope. *Optical Engineering* **41,** 1289–1294 (2002).

43. Wei, J. & Hellmuth, T. *Optical coherence tomography assisted ophthalmologic surgical microscope* US Patent 5,493,109. Feb. 1996.

44. Cable, A. *et al. Microscopy system with auto-focus adjustment by low-coherence interferometry* US Patent 9,869,852. Jan. 2018.

45. Liron, Y., Paran, Y., Zatorsky, N., Geiger, B. & Kam, Z. Laser autofocusing system for high-resolution cell biological imaging. *Journal of Microscopy* **221,** 145–151 (2006).

46. Cao, R., Shen, C. & Yang, C. High-resolution, large field-of-view label-free imaging via aberration-corrected, closed-form complex field reconstruction. *Nature Communications* **15,** 4713 (2024).

47. Zheng, G., Horstmeyer, R. & Yang, C. Wide-field, high-resolution Fourier ptychographic microscopy. *Nature Photonics* **7,** 739–745 (2013).

48. Ou, X., Zheng, G. & Yang, C. Embedded pupil function recovery for Fourier ptychographic microscopy. *Optics Express* **22,** 4960–4972 (2014).

49. Sun, J., Zuo, C., Zhang, J., Fan, Y. & Chen, Q. High-speed Fourier ptychographic microscopy based on programmable annular illuminations. *Scientific Reports* **8,** 7669 (2018).

50. Liang, M. *et al.* All-in-focus fine needle aspiration biopsy imaging based on Fourier ptychographic microscopy. *Journal of Pathology Informatics* **13,** 100119 (2022).

51. Zhou, H. *et al.* Fourier ptychographic microscopy image stack reconstruction using implicit neural representations. *Optica* **10,** 1679–1687 (2023).